Institut de la Matière Condensée et des Nanosciences (IMCN)

Institute of Information and Communication Technologies, Electronics and Applied Mathematics (ICTEAM)

HIERARCHICALLY ORGANISED MATERIALS BASED ON POLYMERS AND CONDUCTIVE ONE-DIMENSIONAL NANOSTRUCTURES FOR THE CONTROL OF ELECTROMAGNETIC PROPAGATION

Thesis submitted for the
Ph.D. degree in Engineering Sciences

by Yann Danlée

on 20th March 2015

Jury members
Prof. Isabelle Huynen, supervisor
Prof. Christian Bailly, supervisor
Prof. André de Lustrac
Dr. Jean-Michel Thomassin
Prof. Luc Piraux, secretary
Prof. Thomas Pardoen
Prof. Jean-Pierre Raskin, chairperson

UCL Université catholique de Louvain

Jury members

Prof. Isabelle Huynen, UCL – ICTEAM (Belgium)
Prof. Christian Bailly, UCL – IMCN (Belgium)
Prof. André de Lustrac, U-Psud – IEF (France)
Dr. Jean-Michel Thomassin, ULg – CERM (Belgium)
Prof. Luc Piraux, UCL – IMCN (Belgium)
Prof. Thomas Pardoen, UCL – iMMC (Belgium)
Prof. Jean-Pierre Raskin, UCL – ICTEAM (Belgium)

Abstract

Wireless communications use microwaves for fast and massive data transfer in our daily life. This thesis presents broadband absorbers, electromagnetic bandgap filters and invisibility cloaks as novel solutions to reduce electromagnetic (EM) interference phenomena responsible for many issues, ranging from simply annoying (e.g. "Wi-Fi drop out") to outright dangerous (e.g. "wrong transmission from health monitor in hospital" or "disruption of airport radar signal by wind turbine") . The studied structures consist of organised stacks of thin layers made of conductive nano-composite and dielectric polymer or ceramic substrate. As conductive fillers, we mainly use carbon nanotubes (CNT) and metallic magnetic nanowires (NW) because of their exceptional electrical properties and high aspect ratio, which allows reaching the electrical percolation threshold at very low concentration. By the nature and concentration of the fillers, we can control conductivity, permittivity and permeability of the composite films. By controlling orientation of the fillers during processing, we can impart anisotropic properties to the structures. A smart arrangement of the different layers is the key for a controlled absorption or propagation of the EM waves.

Broadband absorption is obtained by a novel multilayer arrangement built from alternating films of dielectric polymer and conducting layers. The latter are stacked in a precise gradient of conductivity. The conducting layers consist of either PC-CNT nanocomposite films or a very thin CNT coating. Such multilayers effectively absorb electromagnetic waves from 8 to 67GHz and probably higher despite their overall thickness much lower than the wavelength. The efficiency can further be enhanced with the help of submillimetric multilayers based on Nickel nanowires (Ni-NW) sandwiched between PC films. The magnetic response of Ni-NW contributes to enhanced attenuation of the

incoming waves. Also based on a similar gradient organisation, anisotropic multilayers provide a route to polarisation-selective absorbers.

The second objective of the research is to develop frequency-selective absorbers, also called electromagnetic bandgap (EBG) filters. The multilayer is now able to absorb a specified narrow frequency band or selectively reflect desired wavelengths within the GHz-range. The structures use ultra-thin conductive layers to generate a controlled resonance in homogenous high permittivity sheets. The basic structure is still composed of CNT deposits alternating between dielectric layers. The physical properties (i.e. relative permittivity and thickness) of the dielectric spacers generate narrow high-absorption bands at defined frequencies.

Finally, we investigate the ability of multilayer structures to deviate microwaves around a reflective cylindrical obstacle and reconstruct the incoming wave front pattern behind, i.e. making the obstacle invisible. A cylindrical invisibility cloak requires fine tuning the effective permittivity, which has to grow in gradient from 0 to 1 from the inner to outer radius of the cloak. We have reached this purpose by successively stacking cylindrical polymer foam - CNT composite bilayers with precise thickness of the dielectric layers and precise conductivity of the conductive layers. Parameters of each bilayer are fine-tuned to get the effective permittivity required by theory. Despite some loss, our multilayers demonstrate significant capacity to reduce the distortion of the wavefront pattern behind the obstacle.

Table of contents

Abstract V

Table of contents VII

Author's publications XI

Journal papers XI

International conference proceedings XII

Scientific communications XII

Acknowledgement XV

List of the abbreviations XIX

Chapter I Overview & context 1

Chapter II State of the art 7

1. Development of broadband absorbers 9

1.1. Impedance matching 9

1.2. Resonant absorbers 11

1.3. Hybrid structures 13

1.4. Active materials 14

1.5. Originality of the developed structures for broadband absorption 14

2. Development of electromagnetic bandgap filters 17

2.1. Electromagnetic bandgap metamaterials 17

2.2. Frequency selective surface 19

3. Development of polarisation controllers 20

3.1. Linear polariser 20
3.2. Twist polariser 22
4. Development of invisible cloaking 23
Chapter III Theoretical concepts 25
1. EMI shielding by absorption and bandgap multilayers 27
1.1. Principles of electromagnetic wave propagation 27
1.2. Limit and classification of absorbing structures 31
1.3. Electromagnetic bandgap (EBG) absorption/reflection by EM resonance 34
1.4. Operating on S-parameters 37
1.5. Simulation by chain matrix 38
1.6. Extraction of physical parameters from raw S-parameters 40
1.7. Nanoparticles-polymer composites 46
2. Invisible cloaking 55
2.1. Working principle 55
2.2. Mathematical derivation 57
2.3. Practical approach 66
2.4. Implementation of ε-only controlled multilayer invisibility cloak 71
Chapter IV Materials and methods 73
1. Nanocharges for composites 75
1.1. Origin of nanocharges 75
1.2. Production of metallic nanowires 76
2. Processing of nanocomposites 80
2.1. Compounded polymer-carbonaceous nanofillers composites 80
2.2. CNT ink based composites 82
2.3. Structured patterns in CNT 83
2.4. Metallic nanowires composites 84
2.5. Machining of dielectric spacers for cloak of invisibility 86

3. Electrical characterisation 88
3.1. DC characterisation 88
3.2. AC/microwave characterisation 89
3.3. Set up for wave propagation mapping 90
Chapter V Experimental results and discussion 91
1. Broadband absorber based on CNT 93
1.1. Electrical and morphological characterisation 93
1.2. Structure for wide band EMI shielding 98
1.3. Performance assessment through the Rozanov method 102
1.4. Optimisation of the gradient stacks for the Rozanov optimum 103
1.5. Conclusion 106
2. Nanowires based composites for EMI shielding 107
2.1. Gold nanowire-polycarbonate composites 107
2.2. Nickel nanowires-polycarbonate composites 112
2.3. Conclusion 119
3. Anisotropic composites for polarisation 120
3.1. Electrical and morphological characterisation 120
3.2. Polarisation-selective surface 122
3.3. Microwave twist polarisation 127
3.4. Conclusion 129
4. Electromagnetic bandgap structures 130
4.1. Frequency-selective filter with narrow bandgap 130
4.2. Frequency-selective filter with absorbing peak 132
4.3. Conclusion 135
5. Cylindrical invisible cloaking 137
5.1. Bilayers for controlled permittivity 137
5.2. Stacks of bilayers for the invisibility cloak 143
5.3. Mapping of near field around cloaked zone 148

5.4. Discussion of experimental results and potential enhancements 152
5.5. Prospects and alternatives for invisible cloaking 154
5.6. Conclusion 157
Chapter VI General conclusion & prospects 159
1. Broadband absorption 160
2. Electromagnetic bandgap filtering 162
3. Invisible cloaking 164
References 167
Annex A Plasma treatment for adhesion of CNT ink on PC 181
1. Experimental results 182
2. AFM topography 184
3. X-ray photoelectron spectroscopy (XPS) 186
Annex B Gel permeation chromatography (GPC) of PC-NW composites 189
Annex C Summary of the multilayers 193
1. Building blocks 194
2. Characteristic of the multilayers 196
Multilayer 1 196
Multilayer 2 197
Multilayer 3 197
Multilayer 4 198
Multilayer 5 198
Multilayer 6 199
Multilayer 7 199
Multilayer 8 200
Multilayer 9 200
Multilayer 10 200

Author's publications

Journal papers

1. Y. Danlée, I. Huynen, C. Bailly, "Thin smart multilayer microwave absorber based on hybrid structure of polymer and carbon nanotubes", *Applied Physics Letters*, vol. 100, n°21, pp. 213105.1-3 (2012).

2. Y. Danlée, C. Bailly, I. Huynen, "Thin and flexible multilayer polymer composite structures for effective control of microwave electromagnetic absorption", *Composites Science and Technology*, vol. 100, pp. 182-188 (2014).

3. Y. Danlée, I. Huynen, C. Bailly, "Frequency-Selective Multilayer Electromagnetic Bandgap Structure Combining Carbon Nanotubes with Polymeric or Ceramic Substrates", *Applied Physics Letters*, vol. 105, n°13, pp. 123118.11-4 (2014).

4. Y. Velasquez-Galvan, J. Martinez Huerta, J. de la Torre Medina, Y. Danlée, L. Piraux, "Dipolar interaction in arrays of magnetic nanotubes", *Journal of Physical Chemistry B*, vol. 26, n°2, pp. 026001 (2014).

International conference proceedings

1. Y. Danlée, C. Bailly, I. Huynen, "Thin smart multilayer microwave absorber based on hybrid structure of polymer and carbonated nanoparticles" International Conference on Electrodynamics of Complex Materials for Advanced Technologies (PLASMETA'11), Samarkand, Uzbekistan (2011).

2. I. Huynen, N. Quiévy, P. Bollen, Y. Danlée, C. Bailly, "Multi-hierarchical metamaterials combining conductive inclusions and polymer matrices for Electromagnetic Interference Shielding", Meta'12 Conference, Paris, France (2012).

3. Y. Danlée, I. Huynen, C. Bailly, "Smart Multilayer Frequency-selective Absorber for Microwave based on Hybrid Structure of Polymer and Carbon Nanotubes", Polymer Processing Society 28th Annual Meeting - PPS-28, Pattaya, Thailand (2012).

4. Y. Danlée, C. Bailly, I. Huynen, "Frequency-Selective Coatings Based on EBG Structure Combining Carbon Nanotubes with Polymeric or Ceramic Substrate" The 8th European Conference on Antennas and Propagation - EuCap, Den Haag, The Netherlands (2014).

Scientific communications

1. Y. Danlée, C. Bailly, I. Huynen, "Thin smart multilayer microwave absorber based on polymer and carbonated nanoparticles", 4ème colloque du Laboratoire International Associé : Nanotechnologies & Nanosystèmes, Allevard-les-Bains, France (2011).

2. Y. Danlée, I. Huynen, C. Bailly, "Smart multilayer microwave filter frequency-selective based on polymer and carbonaceous nanoparticles", 10th Wallonia Network for Nanotechnology (NanoWal) on Modelling and simulations at the nanoscale : Links

with experiments, spectroscopies and applications, Namur, Belgium (2013).

3. Y. Danlée, P. Bollen, B. Lecouvet, A. Delcorte, S. Hermans, I. Huynen, T. Pardoen, C. Bailly, "Functional polymer nanocomposites and hybrid structures for the control of electromagnetic properties or fire resistance", Scientific Advisory Committee, Louvain-la-Neuve, Belgium (2014).

Acknowledgement

Je souhaiterais exprimer ma sincère reconnaissance envers toutes les personnes qui ont contribué, directement ou indirectement, à la réalisation de cette thèse. Je remercie tout d'abord mes promoteurs pour leur confiance et le temps qu'ils m'ont consacré. Je les remercie particulièrement d'avoir imaginé ce sujet de thèse original voire un peu fou. Ce sujet rassemblait tous les points qui me tenaient à cœur : une approche plus expérimentale dans le domaine des nanomatériaux, un concept original et relativement libre, et, pour couronner le tout, un sujet qui impressionne la famille !

Ce travail fut possible grâce à l'entraide de nombreuses personnes des pôles BSMA et ELEN. Dès mon arrivée au Boltzmann, j'ai directement pu suivre une série de formations pour maitriser les machines de mise en œuvre, d'observation et de caractérisation. Je remercie Nicolas Quiévy pour le temps et l'énergie passés à me montrer le fonctionnement de l'extrudeuse et, surtout, comment la réparer en cas de panne. Michel, Éric, Rémy, Edwin et François m'ont d'ailleurs aussi souvent donné un coup de main dans cette dernière tâche récurrente. Je remercie Collette pour m'avoir montré très clairement le fonctionnement du SEM. Je remercie Pascale pour avoir relevé la lourde charge de me former au TEM. Il s'agit probablement de la machine la plus compliquée à gérer. Pascale était également ma collègue de bureau et nous avons partagé de nombreux débats et discussions en tout genre. Je remercie Amir pour les observations AFM, Pascal pour mes analyses GPC, Sabine pour l'étude FTIR, Cécile pour l'étude XRD, Sami pour l'accès incessant à la chambre à plasma, Juan Manuel pour les courbes d'hystérésis, Etienne pour la production de membranes nanoporeuses (via it4ip) et de nombreux autres membres du BSMA pour leur collaboration tant au niveau du travail que du divertissement sportif. Ce pôle est

particulièrement vivant grâce aux activités proposées comme le badminton, le mini-foot, la pétanque et le volleyball. Nous avons vécu quelques matchs de volley des plus intenses avec ses incontestables champions (Jeremy, Waël et Pascal) et… les autres ! Les matchs de pétanques étaient aussi bien animés surtout lorsque Guido enseignait sa technique de jeu assez particulière. Les autres activités, à tendance plus gastronomique, étaient (forcément) tout autant agréables. La bonne ambiance contribuait bien entendu au succès de ces activités. Enfin je souhaite saluer : Flavio, Vlad, Gaël, Quentin, Tilia, les Benoîts (Coulomb et Lecouvet), Raphaël, Ali, Naïma, Tabassum, Hadi, Jun, Lalasso, Henok, Anne-Christine, Aurore et aussi ma première collègue de bureau exotique : Miss Fangfang.

Après la mise en œuvre de mes composites au Boltzmann, vient la compagne de mesures électromagnétiques dans la salle Welcome au Maxwell. J'ai appris à utiliser les VNA et autres équipements grâce à Pascal et le Dave. Je les remercie, ainsi qu'Anthony, pour leur aide dans les assemblages de dispositifs particuliers que je leur ai demandée pendant ces quatre années de recherche. Je me dois aussi de remercier mes collègues de bureau pour l'ambiance exceptionnelle, Jérôme, Alberto et notre animateur en chef: Babak. Je salue également mes collègues d'ICTEAM: Ester, Raj, Aline, Pierre-Antoine, Gilles, Guillaume, Nicolas, Pierre Gérard, Mathieu, Dragoş, Marie-Christine, Viviane ainsi que mes collègues d'instituts plus lointains : Pierre Bollen, Francisco, Sébastien, Arnaud…

Plusieurs personnes de l'UCL ou extérieures sont également intervenues dans la réalisation de cette thèse et plus particulièrement au niveau de l'usinage des pièces pour mon système d'invisible cloaking. Je dois des remerciements à Xavier Bollen qui s'est démené pour imprimer mes pièces en ABS à temps; et Yves Charlier via sa société Grando qui m'a permis de faire des découpes de précision dans le Rohacell® et, au passage, de visiter ses machines de découpe par jet d'eau à ultra-haute pression.

Je souhaite adresser une pensée à tous les proches avec lesquels j'ai partagé ces années de thèse. Je remercie tout d'abord mes parents qui m'ont soutenu déjà bien avant d'arriver à l'université, mes grands-parents pour leurs encouragements (et même une participation artistique) et mon frère, Bruno, pour la réalisation de ma table de salon indispensable pour reposer mes pieds après une longue journée en salle de mise en œuvre ! Je salue tous mes amis, Wally, Sam et la Marie, Laurent Genard, Beni,

Loïc, Laurent Francis, Antoine et Susan, Manon et tous les autres… Enfin, le meilleur pour la fin, je remercie ma ravissante compagne, Aline, de m'avoir soutenu et encouragé ces trois dernières années. En réalité, ses encouragements étaient mitigés entre incitations à décrocher le prix Nobel et à prendre plus de congés avec elle ! Quoiqu'il en soit, son enthousiasme pour mes recherches constituait la meilleure des motivations.



List of the abbreviations

ABS	Acrylonitrile butadiene styrene
AC	Alternating current
AFM	Atomic force microscopy
Au-NW	Gold nanowire
CB	Carbon black
CNT	Carbon nanotube
CP	Circular polarisation
CCVD	Catalytic chemical vapour deposition
CVD	Chemical vapour deposition
DC	Direct current
DCM	Dichloromethane
DMF	Dimethylformamide
DMSO	Dimethyl sulfoxide
DUT	Device under test
e-beam	Electron beam
EBG	Electromagnetic bandgap
EM	Electromagnetic
EMI	Electromagnetic interference
EMW	Electromagnetic wave
FOM	Figure of merit
FSS	Frequency-selective surface
FTIR	Fourier transform infrared spectroscopy
GNP	Graphene nano-platelets
GNS	Graphene nanosheet
GPC	Gel permeation chromatography
LL	Line-Line
LP	Linear polarisation
LRL	Line–Return–Line
Ni-NW	Nickel nanowire

MAS	Microwave absorbing structure
MWCNT	Multi-walled carbon nanotube
NW	Nanowire
PC	Polycarbonate
PMMA	polymethyl methacrylate
PTFE	Polytetrafluoroethylene
PVC	polyvinyl chloride
RAM	radar absorbing materials
SEM	Scanning electron microscope
SRR	Split ring resonator
SWCNT	Single-walled carbon nanotube
TE	Transverse electric
TEM	Transmission electron microscopy
TM	Transverse magnetic
vdW	van der Waals
VNA	vectorial network analyser
XPS	X-ray photoelectron spectroscopy

Chapter I

Overview & context

Wireless communication via electromagnetic (EM) transmission in the microwave range is a fast and simple solution for a lot of applications and has become ubiquitous in everyday life. In parallel, electronic devices are becoming ever more compact and integrated. These trends generate a growing issue with EM interference (EMI), which can occur between devices or, even worse, between subcomponents of the devices themselves (1). For instance, it is mandatory to shield electronics microchips to avoid digit errors due to the interference from outside environment (2) (3). The consequences can range from simply annoying to outright dangerous. Medical probes and equipment, for instance, are at risk of being disturbed by the surrounding EM waves in particular from mobile phones (4). The major part of usual telecommunication signals used for mobile phones (5), GPS (6), television (7), radars (8) and so on are detrimentally affected by metallic structures in the environment which are the source of interferences. The current interest in telecommunications suggests that the number of emitters and, therefore potential problems, undoubtedly will increase in the future. Faced with this issue, the European Union member states have adopted a number of directives applying to any equipment placed on the market or taken into service. Its scope covers all apparatus "liable to cause electromagnetic disturbance or the performance of which is liable to be affected by such disturbance" (9). These directives are continuously updated to follow this fast-growing trade (10). This situation is complex to solve because there is no unique solution satisfying all scenarios. Each type of device must have a tailored solution which reduces its electromagnetic "pollution" and without interfering with its inner operations and outer communications.

EMI shielding by absorption remains an ideal solution for many problems of interference. Whether for isolating an electronic component, probe etc. from external parasites or even its own interferences, microwave absorption turns out to be the most appropriate solution. It radically solves the problem by simply removing all EMI. One of the major challenges is to minimise the thickness of the absorbing materials to make them compatible with the targeted components which are often microscopic. EMI shielding is as well required for large sensitive equipment or even for an entire room. The manufacturing of the absorber must be feasible at different scales and the absorber must preferably be conformable to an arbitrary shape. Those conditions force to select a material and optimise its structural organisation to reach the objectives.

However, total absorption is not appropriate for all applications. Many devices operate precisely through wireless communications. Obviously a mobile phone cannot be isolated from the cellular network! Broadband absorption is then inapplicable since it prevents the normal use of the communication network. The wireless connected devices require selective filtering of troubling waves from the operating frequency band. This level of control is called electromagnetic bandgap (EBG) filtering. The use of filters goes beyond the reduction of interference, it appears as a smart way to protect data. For instance, a company may require shielding its Wireless Local Area Network (WLAN) to confine confidential data in the building. The electromagnetic isolation/shielding must nevertheless allow transmission to other public networks such as mobile/cellular phones, satellite broadcasting, etc... On the contrary, it might be important to absorb all frequencies except a narrow useful band. The current market thus requires precise solutions in terms of targeted absorption over a broad spectrum or a narrow frequency band.

Besides a proper control of absorption in terms of frequencies, some emitting/receiving systems work with polarised waves. This leads to an emerging interest for absorbers operating along only one direction in order to shield the polarisation of a radar signal, for instance, while not interfering with potential other signals polarised at another angle. Polarisation-selective absorption is then a clean solution for this type of communications.

Although controlled absorption is an undeniable solution to reduce the problems caused by EMI, several concrete situations are not helped with controlled absorption. Civil aviation and weather radars, for example, have a distorted "vision" of the sky due to metal structures present in the environment (11). Wind turbines cause particularly annoying interferences to the detection of aeronautic radars (12). The air traffic control radars are liable to incorrectly localise aircrafts with a slight offset from the actual position with the dramatic consequences this may have (13) (14). Weather radars can also detect virtual turbulences which are actually caused by wind turbines (15). This phenomenon is caused by the rotating blades which change the refractive index of the medium. Since the refraction of the signal varies in an uncontrolled manner, the view reproduced by the receiver is incorrect (16). Covering those structures by an efficient absorber does not provide a convincing solution because it generates a shadow behind the wind turbines. The magnitude of the signal would become too weak for a reliable detection.

The only effective solution is the deviation of the radar waves in order to bypass all disturbing constructions which would make them invisible to the desired frequency since the signal would get around the object without ever passing through. Such solution has been dubbed "invisibility cloaking" and is no longer reserved to the realm of science fiction.

In summary, EMI problems are diverse and complex. They require tailored solutions. The key issue lies in a complete control of the propagation of microwaves. Either the propagation of the wave must be attenuated at all frequencies, at particular frequencies or in a particular polarisation state, or it has to be deviated following a well-defined path. In this thesis, we propose novel solutions along these lines. The basic building blocks are conductive nanofillers such as carbon nanotubes or metal nanowires combined with polymer, mainly polycarbonate but other polymer substrates and ceramics are used too. Polymer-nanofillers composites are particularly adapted to interact with microwaves through their easily controllable conductivity (or even ferromagnetism). The proposed solutions are characterised by a hierarchical organisation of layered structures that contributes to their very EM high efficiency but also excellent mechanical properties, such as flexibility, and simplicity with respect to the state of the art. The related scientific challenges of the thesis deal with the control of the multilayer structures morphology, on one hand, and the proper analysis and prediction of their EM behaviour, on the other hand. Another characteristic of the work is the very strong interaction between the experimental and simulation aspects. EM models have been developed and used for the multilayer structures used throughout the thesis and in most cases have informed the experimental realisation.

The thesis is organised as follows. An overview of broadband absorption, EBG filtering and invisible cloaking is first given in chapter II through a comparison to the state of the art to highlight its originality. Chapter III develops the theory of EM absorption, bandgap control and cloaking principle. The same chapter also introduces the model used to extract useful physical parameters from raw data (i.e. S-parameters), and others models using physical parameters as input to predict the frequency behaviour of the stacks of composites used throughout the work. Next, the experimental details on materials and methods are given in chapter IV. This is followed by a presentation of the main results in chapter V. This chapter first presents broadband absorbing multilayers based on carbon nanotubes (CNT) and polycarbonate, followed by

similar organised structures based on metallic nanowires, followed by anisotropic stacked films effective as broadband polarisers. The EBG filters are next introduced. The last section of this chapter deals with invisible cloaking based on polymer substrate and PC-CNT composites. Finally, the conclusion is drawn and perspectives of the thesis are given.

Chapter II

State of the art

This chapter presents an overview of the state of the art for the four types of EM functionalities developed in this thesis, i.e. broadband absorbers, EBG filters, polariser filters and invisible cloaks. In the conclusion of each part, we contrast the solutions described in literature with the approach developed in the thesis.

1. Development of broadband absorbers

Classical broadband EMI shielding is based on EM reflectors, usually metal foils or coatings, called Faraday cages (17). But these methods are less and less satisfactory in the present environment because the interfering EM signal is only deflected in another direction where it can still create havoc. This explains the growing popularity of EM absorbers, which truly eliminate the EM signal in directions or locations where it is unwanted. Broadband absorption is a delicate balance between high conductivity and low dielectric constant (18). Metal-based EM absorbing structures are impossible to obtain because EM waves do not penetrate the material but are reflected instead. This is the so-called skin effect: the penetration depth of an EM wave in a metal is approximately inversely proportional to the square roots of its conductivity and the signal frequency (19). Metals have low penetration depth and simply reflect EM waves. The challenge for shielding by absorption is precisely to avoid excessive reflection, whereas the transmission must be reduced. The scientific literature proposes several strategies which answer to the performance criteria demanded by specific applications. Radar absorbing materials (RAM) can be classified in two main classes: impedance matching and resonant absorbers, though it will be shown in the following discussion that many absorbers have features of both of these classes (20).

1.1. Impedance matching

The propagating wave that comes upon an interface will undergo some reflection that is proportional to the magnitude of the impedance

gap between incident and transmitting media. For complete attenuation of the incident wave, one or more wavelengths of material thickness are required, making bulky absorbers, very thick and adding weight. The non-reflective RAM are usually used as surface coverings in electromagnetic anechoic chambers, etc. Their primary function is to absorb and dissipate the electromagnetic energy with extreme efficiency to allow performing high precision measurements without any internal and external EM parasite. Several types of impedance matching RAM have been developed: pyramidal, tapered and matched absorbers.

Pyramidal absorber

The pyramidal absorbers are typically thick materials with pyramidal or cone structures extending perpendicularly to the surface in a regularly spaced pattern (see Fig. 1). These absorbers are developed so that the interface presents a gradual transition in impedance from air to that of the absorber. Furthermore, the shape directs the small fraction of the reflected incident wave from one pyramid toward the next pyramid, giving another opportunity for attenuation. The height and periodicity of the pyramids tend to be on the order of one wavelength. Pyramidal absorbers thus have a minimum operating frequency above which they provide high attenuation over wide frequency and large angle ranges.

Tapered loading absorber

The tapered absorbers are successive slabs of lossy materials stacked such that the characteristic impedance increases as the wave penetrates through the absorber (see Fig. 1). Most tapered absorbers are built from a few layers in order to tend toward a continuous gradient of the impedances. A second type of similar absorbers consists in stacks of homogeneous layers with increasing loading in the direction of propagation. The advantage of this class of materials is that they are thinner than pyramidal absorbers but they have poorer performance.

Matching layer absorber

The matching layer absorber places a transition absorbing layer between the incident (usually air) and absorbing media to reduce the thickness required for the gradual transition materials (see Fig. 1). The combined impedance from the first and second layers equals the impedance of the incident medium. This matching will be achieved when $Z_1 = \sqrt{Z_0 Z_2}$ and the thickness of the matching layer $t_{ml} = \lambda/4$. The last condition is met only for a certain frequency which makes the matching layer materials narrow band absorbers.

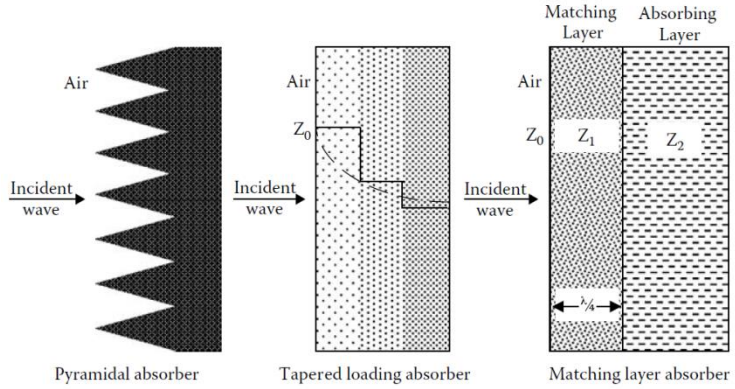


Fig. 1. illustrations of typical pyramidal, tapered loading and matching layer absorbers (21)

These impedance matching absorbers provide the best performance. The disadvantage (particularly for the pyramidal absorbers) is their thickness and tendency to be fragile. They are usually used for anechoic chambers because of their excellent absorption index.

1.2. Resonant absorbers

Resonant absorbers do not aim to match the impedance between the incident and absorbing media. Corresponding structures are thinner but do not absorb all the EM power. A first reflection is due to the mismatch of impedance at the entrance of the absorber. Secondly, a partial ratio of the transmitted wave is reflected from a metal coating the back side. If the distance travelled by the transmitted wave is an even

multiple of $\lambda/2$ then the two reflected waves will be out of phase and destructively interfere. The total reflected intensity is zero for the case where the magnitude of the two reflected waves is equal. Resonant materials are also called tuned or quarter wavelength absorbers and include Dallenbach layers, Salisbury screens and Jaumann layers.

Dallenbach layer

A Dallenbach tuned layer is a layer of homogeneous lossy material placed on a conducting substrate (see Fig. 2). The thickness, permittivity, and permeability can be adjusted so that the reflectivity is minimised for a desired wavelength. The Dallenbach layer relies on destructive interference of the waves reflected from the first and second interfaces. To obtain a minimum reflectivity, the effective impedance of the layer Z_M must equal the incident impedance Z_0. Optimisation of Dallenbach layers has shown that it is not possible to obtain a broadband absorber with only one layer, however several layers stacked together show increased bandwidth.

Salisbury screen

The Salisbury screen is also a resonant absorber, however, unlike the tuned absorbers it does not rely on the permittivity and permeability of the bulk layer. The Salisbury screen consists of a resistive sheet placed at an odd multiple of ¼ wavelengths in front of a metal backing usually separated by an air gap or a material with higher permittivity which replaces the air gap (see Fig. 2). The effective impedance of the structure is the sheet resistance. The impedance matching occurs thus if the sheet resistance is 377 $\Omega/\square$ (i.e. the impedance of air). An analogue of the electrical screen would be to place a magnetic layer on the metal surface, resulting in a thinner device (22).

Jaumann layer

Jaumann layers are a modification of Salisbury screens allowing to increase the absorption bandwidth. The device consisting two (or more) equally spaced resistive sheets in front of the conducting plane is able to

produce two minima in the reflectivity (see Fig. 2). This increases the bandwidth but the global thickness is of course increased too. Some optimisations of Jaumann absorbers are feasible but they are complex due to the number of parameters involved, especially when the number of layers increases (23).

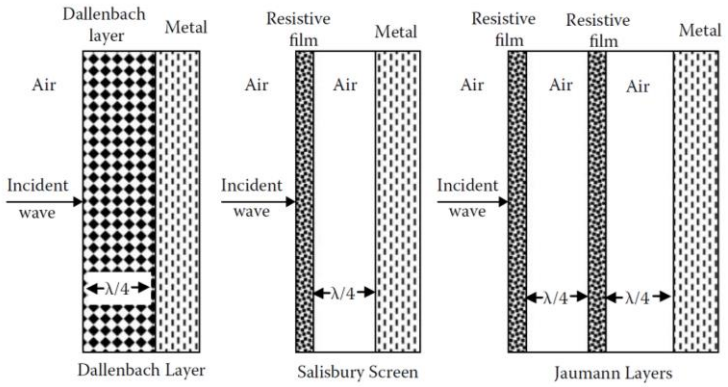


Fig. 2. illustrations of typical Dallenbach layer, Salisbury screen and Jaumann layer absorbers (21)

1.3. Hybrid structures

The development of microwave absorbing structures (MAS) runs parallel to the increasing use of composites in aerospace applications, and has led to a research focus on stealthy materials. Multifunctional requirements demand component structures that have desirable mechanical, thermal, electromagnetic, and chemical properties. Cellular materials, such as foams, honeycombs and lattice materials are ideally suited to achieve multi-functionality. The waveguide characteristics of a honeycomb combined with the performance of lossy foam lead to unexpectedly large EM power absorption over a wide frequency range superior to any known material (24). Fig. 3 shows an example of a hybrid produced by P. Bollen et. al. (25). The peak absorption frequency can be tuned by varying the shape of the honeycomb unit cell. Recent research in this field shows an efficiency in terms of absorption index close to impedance matching structures with the advantage of a undeniably better mechanical resistance (26) (27).

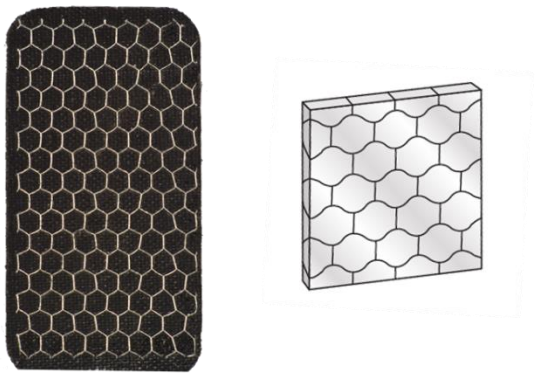


Fig. 3. Example of hybrid microwave absorbing structure (25)

1.4. Active materials

Electromagnetic absorption by a composite material can be actively controlled if the material has certain "active" inclusions. Such inclusions correspond to pyrosensitive solid electrolytes (28), polyconductors (29) and certain photosensitive materials. Pyrosensitive electrolytes change their behaviour from dielectric to conductor (α to β phase transitions) at a critical temperature. In the α-phase the conduction is essentially due to ions. It is possible to synthesise a pyrosensitive composite material by dispersing a solid electrolyte in a host medium. With appropriate thermal excitation, the composite material shows significant EM absorption. A variety of solid electrolytes are available which can be judiciously adopted in synthesising EM absorbing composites. Another family of conductors known as polyconductors have also shown active EM absorption under thermal and/or optical excitation. Synaptically configured arrays of photosensitive materials could possibly lead to a composite with photosensitive elements constituting an "active" microwave absorber (30).

1.5. Originality of the developed structures for broadband absorption

Effective EM absorbing structures described above comprise a large majority of a low permittivity dielectric material and a small fraction of

finely distributed conducting particles. It immediately suggests the use of polymer-based heterogeneous materials, in particular nanocomposites and hybrid structures (31). The need for overall high conductivity also requires percolation of the conducting substructure in the matrix, hence conducting particles with high aspect ratio are preferred and excellent control on dispersion of the conductive filler is essential. Wire-shaped nanocharges as carbon nanotubes (CNT) or metallic nanowires (NW) are a usual choice because of their extremely high intrinsic conductivity and their high aspect ratio (31). Multiwall carbon nanotubes (MWCNT) obtained by the CVD process are a logical choice for the conductive fillers (32) (33) and their easy dispersibility in selected polymers allows reaching the percolation threshold at low loading level. In addition, CNT have an extremely high intrinsic conductivity. The low permittivity matrix allows EM waves to penetrate deeply in the absorbing structure but the conducting network dissipates the EM energy through complex resistive-capacitive coupling and multiple internal reflections (34). Current polymer-based solutions and ideas for EM control use (nano)composites with carbon nanotubes and/or metal particles (35). These composites have an excellent shielding effectiveness but are inefficient in terms of EM absorption because their effective permittivity is still too high and they primarily reflect the signal (36). Foaming the polymer matrix is an efficient method to reduce reflectivity by decreasing the permittivity, but at the expense of thickness (37) and is thus not suitable for compact applications. A recently described multi-scale "hybrid" structure offers a better compromise between EM absorption and structure thickness (38). This last example highlights the importance of structural organisation to exceed the current limitations and improve the performances.

This thesis presents novel hierarchically organised multilayer polymer structures, very effective for EM absorption in the typical microwave frequency range. We aim to maximise the absorption/thickness ratio. Our strategy tries to combine to efficiency of impedance matching absorbers with a drastically lower thickness through a smartly arranged multilayer. The structures are obtained by stacking conductive and insulating layers. The conductive layers can either be obtained in the form of polycarbonate - carbon nanotubes (PC-CNT) nanocomposite films or as CNT-based ink coatings on neat PC films. PC has low relative dielectric constant in the GHz range (2.8). Compounded with CNT, it offers durable mechanical properties (39)(40). Multiwall CNT are also easy to disperse in this polymer (41). The effectiveness of the multilayer structures stems from their gradient periodic arrangement.

Indeed, a controlled gradient of conductivity across the stacked pile is the key to their shielding effectiveness. The structures are easy to make, very thin (thickness much lower than the centimetric wavelength) and conformable. Despite their small thickness, they can, thanks to the specific arrangement, absorb effectively over a broad frequency range (see section V-1.2).

Yet it is possible to further extend the absorption/thickness limit. The combined use of magnetic particles and conductive fillers drastically amplifies the energy absorption because attenuation of the wave results from the addition of resistive and magnetic losses. In this context, new types of high-performance absorbers have emerged. They require using magnetic nanocharges. The contribution of a magnetic substance can come from carbonaceous nanostructures decorated by ferromagnetic particles (42) or even embedding them (43). This method is however limited because the permeability of the composites often is quite weak. Nowadays, excellent results are achieved with ferromagnetic nanowires directly implemented in a polymer matrix (44). In this thesis, we develop hierarchically organised multilayers built from ultra-thin deposits of Nickel nanowires on polymer films which prove highly effective for broadband absorption at very low thickness (45). This allows us to get closer to the ultimate absorption limit defined by Rozanov (46) as explained later. We also propose in section III-1.2 the definition of a figure of merit allowing to compare to each other performances of the various absorbing structures developed in the thesis. The multilayers proposed in this work have the advantage of a very simple process. Moreover, they are "modular", i.e. they can easily be restacked to respond to a new frequency absorption target, without rebuilding them from scratch.

2. Development of electromagnetic bandgap filters

The current compact and integrated telecommunication devices require advancing EMI shielding solutions further than uniform broad frequency absorption or reflexion. It is often necessary to selectively absorb undesired waves while transmitting the signal in other frequency bands (47). This requires organised structures with defined periodicity (48), interacting selectively with certain EM frequencies (49), which fall under the broad definition of metamaterials (50) as electromagnetic bandgap (EBG) and Frequency selective surface (FSS).

2.1. Electromagnetic bandgap metamaterials

Electromagnetic bandgap metamaterials control wave propagation with bandgaps designed to prevent propagation at desired frequencies (51). The period size of EBG is directly related to the wavelength since it is the key for creating constructive and destructive interference.

Based on the concept developed in 1987 that creating a periodicity in dielectric materials could stop the propagation of waves at certain frequencies, lot of work has been carried on the concept of photonic crystals in order to create a so-called photonic bandgap material, more generally termed as electromagnetic bandgap (52). Basically, a photonic crystal is made of a periodic arrangement of inclusions having high dielectric constant in a low dielectric template, and inhibits wave propagation due to destructive interference from scattering on inclusions of the equivalent lattice. 3D and 2D lattices have been investigated extensively. Usually, structures used for GHz-EBG are intrinsically

complex and sensitive to any fabrication defect (53). Most photonic/EBG structures operate at higher frequencies, typically plasmon frequency (54), and they are also facing technical difficulties to achieve stable and robust filters (55). A 2D-EBG structure is easier to fabricate, since it possesses periodicity only in a plane (x-y), and is finite along the third dimension (z). As a result, bandgaps are seen for waves propagating in the plane, while propagation normal to the plane (z) will not see any bandgap since there is no dielectric variation in the z-direction. The declination to 1D-structures is obvious: structures being periodic along a single direction will induce bandgaps for waves propagating along this direction.

In the 2000's, research extended to metallo-dielectric EBG structures, obtained by replacing the periodic high dielectric constant cavities by metallic inclusions. As a result, 2D-EBG metamaterials typically consist in arrays of patterned conductive resonators placed on a dielectric plate. These EBG metamaterials are designed to prevent the propagation of an allocated bandwidth of frequencies, for certain arrival angles and polarisations. Various geometries and structures have been proposed but their use is limited to very specific applications (56), requiring a small shielding surface only (57).

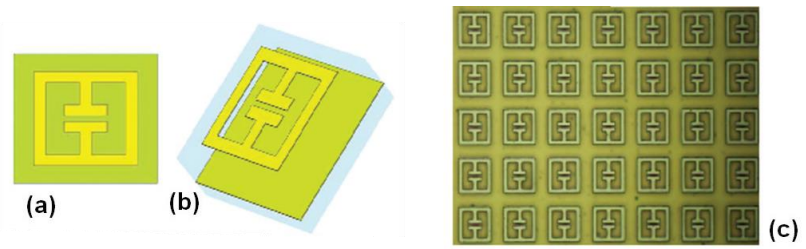


Fig. 4. Example of EBG metamaterial absorbing at 1.6THz over a wide range of angles of incidence for both TE and TM radiation (58).

Our EBG metamaterials is based on gradient multilayers. They are related to Jaumann resonators, improved by the use of materials and a geometry that increase resonance mechanisms. Jaumann layers were initially designed with purely resistive sheets and are normally metal back-covered. In our case, the metal layer is removed since the signal must be transmitted at the wanted frequency. The lossy sheets are calibrated such as the thickness is proportional to $\lambda/2$ for optimising resonance depending on frequency (instead of broad absorption).

Replacement of the typical air sheets with materials providing better mechanical and EM properties such as high-ε substrate, broadens the design scope of the multilayers (see details in section V-4.1).

2.2. Frequency selective surface

Frequency selective surfaces (FSS) are a subclass of 2D-EBG metamaterials that exhibit bandgap and passband depending on the polarisation and angle of arrival of the incident wave. For example, a periodic array of conductors will reflect incident waves at some frequencies while remaining transparent to them at other frequencies. FSS structures mainly contain arrays of metallic patches printed on a substrate arranged in a two dimensional lattice (59), and have found many filtering applications in microwave and millimeter-wave engineering. Some examples are reflector antennas (60), radome design (61), polarisers (62) and beam splitters (63). When active devices are added to the unit cell of these periodic structures, a new group of such surfaces called active grid arrays is obtained, opening the possibility of externally controlling FSS characteristics (64). Some studies have been reported on FSS containing ferrite (65), liquid (66) and chiral substrates (67) in order to improve performance. The probably most widespread application of FSS is the frequency-selective radar absorption (68).

The method developed in this thesis follows a multilayer concept which is improved to get a high reflection at desired frequency. The resonance is controlled thanks to the thickness and EM properties of dielectric slabs sandwiched between two reflective layers. This FSS bears some similarity with Salisbury screens except that used materials are selected for maximising the resonance at one fixed frequency (see section V-4.2). The FSS multilayers are built from strong and simple materials such as natural ceramic which could be advantageous for concrete applications.

3. Development of polarisation controllers

Polarisation transformers have numerous applications, for instance, radar/antenna engineering. A variety of polarisation transformers have been described for different applications, such as circular polarisation (CP) selectivity (69) (70), polarisation rotation of a linearly polarised (LP) plane wave (71), and LP to CP conversions (72). Certain arrays of small resonant particles have been previously used to realise an ultrathin LP to CP transformer (73). The present work focuses on linear polariser for microwave filtering by absorption. The waves with the selected polarisation are transmitted while the others are absorbed.

As additional function, we also introduce a twist polariser. The system forces the polarisation axis to rotate towards a predefined angle. The scientific literature is quite limited in this radar application field. In the next paragraphs, the state of the art in the domain is briefly described and current solutions are compared with the working principle of twist polariser multilayer developed in section V-3.3.

3.1. Linear polariser

Polarisers allow the transmission of only one polarisation state. A linear (or plane) polariser transmits EMW polarised in a single plane. The direction of the output polarisation is adjusted independently of the input polarisation, through the proper rotation/orientation of the linear polariser in the plane perpendicular to the propagation axis (see Fig. 5). Four types of linear polarisers are known: dichroic, beam-splitting, birefringent and wire-grid polarisers. A dichroic polariser is a material

having different absorption for perpendicular incident planes (as an example, a tourmaline crystal has a unique optical axis, and any electric field vector which is perpendicular to that axis is strongly absorbed) (74). Beam-splitting polarisers divide unpolarised incident light into two orthogonal, linearly polarised beams (75). Birefringent linear polarisers exploit the birefringent properties of crystals (such as quartz and calcite) to split a beam of unpolarised light by refraction into two rays. Snell's law holds for one of these rays, the ordinary, but not for the other, the extraordinary (76). The three types of polarisers introduced above work for visible light but are not able to keep their properties at microwaves. Actually, the wire-grid polariser is the unique system working from radar frequencies up to infrared (77) (78). This simple polariser consists of a regular array of fine parallel metallic wires, placed in a plane perpendicular to the incident beam (see Fig. 5). Electromagnetic waves which have a component of their electric fields aligned parallel to the wires induce the movement of electrons along the length of the wires. Since the electrons are free to move in this direction, the polariser behaves in a similar manner to the surface of a metal and the wave component aligned parallel to the wires is reflected backwards along the incident beam.

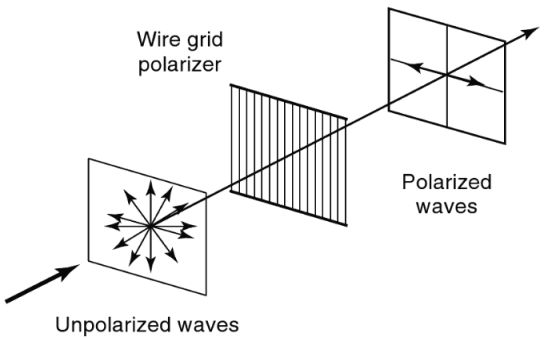


Fig. 5. Microscopic wire grids act as polarisers for centimetric up to infrared radiations. Transmitted electric field oscillates perpendicular to the direction of the wires (77).

The concept of wire-grid polariser can be extrapolated to anisotropic composite films showing a conductivity dependence on the direction in the plane. It has been proven that a film (79) or a multilayer (80) of oriented CNT acts as a polariser in terahertz. We have developed multilayers polarisers for GHz-range based on oriented CNT and

patterned CNT strips. The process of implementation is detailed in section IV-2.1 and IV-2.3, and the experimental results are summed up in section V-3.2.

3.2. Twist polariser

A twist polariser is a system able to change the polarisation angle of the electric field of an EM wave. Fig. 6 gives an illustration of the phenomenon. The literature proposes different designs for various polarisation transformers at microwaves but there is no efficient way of designing such devices (81). In optics, the phenomenon is commonly used in the liquid crystal screen; it is the twisted nematic field effect (82). For microwaves, T. Niemi et. al. has given a simulation of twist polariser comprising an array of chiral elements, i.e. pairs of orthogonal canonical helices (83). Our strategy consists to stack anisotropic layers at a constant angle increment to force the electric field to rotate. The efficiency of this twist polariser is discussed in section V-3.3 and some perspectives are given trough simulations.

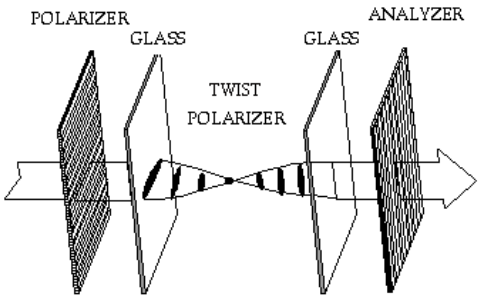


Fig. 6. Illustration of a typical twist polariser. The polariser at the entrance filters a horizontal polarisation and next the twist polariser forces the electric field to rotate perpendicularly to the analyser plate. (84)

4. Development of invisible cloaking

Invisibility has long been employed in works of science fiction and fantasy, from "cloaking devices" on Bond's car in *Die Another Day* to Harry Potter's magic cloak. But it nowadays begins to be imaginable making devices with these properties. To achieve the feat of "cloaking" an object, physicists have developed what are known as metamaterials, some of which can bend electromagnetic radiation, such as microwaves or even visible light, around an object, giving the appearance that it isn't there at all. This concept also includes acoustic cloaking for sonar invisibility. A laboratory metamaterial device that is applicable to ultra-sound waves has been demonstrated in January 2011 (85). It can be applied to sound wavelengths from 40 to 80KHz. The metamaterial cloaking mechanism bends and twists sound or electromagnetic waves by intentional design in the same way the wave is deflected by the surrounding material making the structure invisible. Research in the electromagnetic field has started much earlier and corresponding papers are much more numerous. The latest progress even shows the proposition of an anti-cloak (86) which annihilates some effects of invisibility cloak at a distance outside the cloaking shell (87).

The first artificial dielectrics in microwave engineering have been developed just after World War II. Yet, there are already seminal explorations of artificial materials for manipulating electromagnetic waves at the end of the 19th century and later for optical frequencies (51). In 2006, J. Pendry came up with the idea of bending light in such a way that it could form a container around an object making the object invisible. He wrote, with D. Schurig and D. Smith, the now famous paper demonstrating the idea at the frequency of microwaves (88). This idea has stimulated much recent work in the field of metamaterials. An

experimental device rapidly validates the concept with a cylindrical cloaking at 8.5 GHz (89) (90). However, a cloak that can conceal objects across the entire electromagnetic spectrum is still decades away. Many physics and engineering problems need to be solved.

The effective permittivity of the cloak must range between 0 and 1, which means that no homogenous material can do the job (91). Hence the targeted structures belong to the class of "metamaterials". Their structure is however complex and their implementation is relatively expensive. A current method involves the evaporation of a metallic substance on a dielectric substrate with a specific pattern (89) (92) (93). This yields effective systems with performance close to theoretical prediction. However, the fragility of such structures makes them difficult to use for large constructions such as an entire tower or wind turbine. Our strategy is to replace the metal pattern on the substrate by a hierarchical structure based on polymeric foam and CNT composite. This approach has a strong advantage from the standpoint of simplicity. Some published works confirm the ability of CNT-based structures to control effective permittivity (94) or permeability (95) down to negative values as required.

Chapter III

Theoretical concepts

Research conducted as part of this thesis aims to build and use composites, mainly based on carbon nanotubes (CNT) and polycarbonate (PC) to control the propagation of signals in two different ways, namely absorbing/cancelling or deflecting microwaves. This chapter first explains the strategy used throughout this thesis to implement thin and highly efficient absorbers. It is confronted with the state of the art through reflectivity measurements widely used in the field of radar and stealth applications, and recommended for the application of the formalism of Rozanov. The PC-CNT composites are structured as gradient multilayers for optimal absorption. The absorption/thickness ratio has been ultimately enhanced by the use of magnetic nanowires instead of CNT. Those absorbers are quantified via a figure of merit and situated to the Rozanov limit. The basic building blocks are then modified in order to adapt the absorption spectrum to additional needs. In particular, we analyse the requirements for electromagnetic bandgap (EBG) filters able to absorb or reflect only wanted frequencies. A variant of the composite with aligned nanofillers is also discussed. In the latter case, we obtain a microwave polariser.

Besides absorption, the chapter also envisions the possibility of deflecting the microwaves. The panel of developed composites correctly orchestrated with polymeric substrate can force the microwaves to pass around an object of any nature without disrupting the incoming wavefront. The stack of composite films correctly guides the incident waves through the coating without significant absorption. The theory explaining the interaction between composites and polymer slabs is described and illustrated by simulations. The stack in composite-polymer bilayers is the key concept to engender a precise effective permittivity and then control the deviation of the waves. The effective permittivity of each bilayer approximates the wanted values by a right coordination between polymer thickness and conductivity of the composite. This method fills the condition for getting an invisible cloaking applicable for radar waves. This method is discussed and compared with the current research and development in this field in term of quality and EM loss.

1. EMI shielding by absorption and bandgap multilayers

1.1. Principles of electromagnetic wave propagation

Electromagnetic waves (EMW) have both electric and magnetic field components, which oscillate in a fixed relationship with respect to one another, perpendicular to each other and perpendicular to the direction of energy and wave propagation (96). In vacuum, it propagates at a characteristic speed, the speed of light in straight line. EMW are emitted and absorbed by charged particles. The electromagnetic spectrum is divided, for practical engineering purposes, into radio waves, microwaves, infrared radiation, visible light, ultraviolet radiation, X-rays and gamma rays. The eyes of various organisms are only sensitive to a relatively small range of frequencies of EMW called the visible spectrum or light; what is visible depends somewhat on which species of organism is under consideration. The theory summarised in this thesis is applicable to the entire EM spectrum but the investigation and application are focused on radar waves (GHz-range).

In classical physics, we consider that an electromagnetic wave is emitted when charged particles are accelerated by forces acting on them. Electrons are responsible for emission and also absorption of most EMW because they have low mass, and therefore are easily accelerated by a variety of mechanisms. Absorption in materials is mainly due to electron interaction. The following theory of absorption is based on global material properties such as conductivity, permittivity and permeability. Electrical conductivity is the ability of a material to allow electrical charges to move freely, thus allowing the passage of an electric current. Permittivity is a physical property that describes the response to

a given applied electric field to a medium. At the microscopic level, permittivity is related to the polarisability of the molecules or atoms constituting the material. The permittivity of a material is a tensor since the response of the material may depend on the orientation of the crystallographic axes and reduces to a scalar in isotropic media. Magnetic permeability characterises the ability of a material to change a magnetic field, in other words, to change the magnetic flux lines. The magnetic field influences the migration and/or reorientation of magnetic dipoles. The combination of all those physical properties determines the behaviour of a material in the presence of EMW.

An incoming wave on a typical slab-shaped obstacle can be (partially) reflected, transmitted or absorbed as illustrated by Fig. 7. The absorption index is defined by

$$A = \frac{P_{abs}}{P_{in}} = \frac{P_{in} - P_{ref} - P_{tr}}{P_{in}} \qquad \textit{eq. III-1}$$

where P_{tr} and P_{ref} are respectively the transmitted and reflected power. For maximal absorption, a material with a low electromagnetic transmission but also a low reflection must be chosen. Many structures have been developed to attenuate EM transmission. The transmission (also called attenuation) is mainly controlled by the thickness d and the imaginary parts of ε (related to conductivity σ) and μ (noted μ'') of the component as shown by the following equation (97) :

$$T = e^{-i\omega d\sqrt{\varepsilon\mu}} = e^{-\frac{i\omega d}{c}\sqrt{\varepsilon_r\mu_r}} \qquad \textit{eq. III-2}$$

where ω is the pulsation, c is the speed of light in vacuum and i is the imaginary number. Highly conductive components involve a high imaginary part of ε_r which provides excellent extinction. On the other side, the reflected power also increases with conductivity, drastically reducing the amount of energy actually absorbed. Neglecting multiple reflections, the reflected power is

$$P_{ref} = |R|^2 P_{in} \qquad \textit{eq. III-3}$$

where R is the reflection coefficient at the interface with the incoming wave, expressed as (98) :

$$R = \frac{\sqrt{\frac{\mu_r}{\varepsilon_r}} - 1}{\sqrt{\frac{\mu_r}{\varepsilon_r}} + 1} \qquad \textit{eq. III-4}$$

Reflection is minimal if ε_r is equal to μ_r which is 1 for non-magnetic materials. Those mathematical considerations show that an absorber must combine high conductivity and low permittivity. Unfortunately, no simple material combines those properties. A clever arrangement of high conductivity and low permittivity zones must be imagined. A stack of successive dielectric and conductive layers stands out as an attractive but little studied option to reach the aimed properties (99).

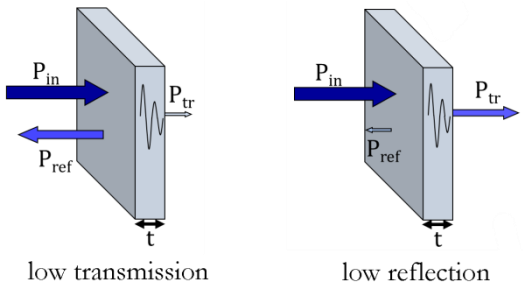


Fig. 7. Diagram of absorbers with low transmission or low reflection

In addition to the intrinsic properties of the material, the arrangement of layers plays an important role for maximal absorption. A stack where the conductive layers have all the same conductivity is not optimal to minimise reflection. Indeed, the incident wave is reflected significantly on the first conductive layers. A gradual increase in conductivity lets the wave propagate deeper into the material (100). As the wave progresses in the multilayer, reflection increases but it takes place inside the multilayer. The energy is "trapped" between the internal conductive layers with less outside reflection. A gradient of conductivity of the conductive layers hence leads to a higher overall absorption due to reduced reflected power. The direction of incidence becomes also critical. Referring to the inset of Fig. 8, the incident wave must penetrate the multilayer at the low conductivity end of the gradient, i.e. at port 1. Reflection would be prohibitive for a wave incident at input interface of port 2.

A simple method based on chain matrix conversion simulates the scattering parameters (S-parameters) and absorption index if the physical parameters of each layer are known. S-parameters are relevant quantities widely used in microwave measurements and analysis. They link, in matrix formalism, the incoming and reflected waves and are helpful to gain precise understanding of the electromagnetic behaviour of a multilayer. We use an analytical model, implemented in Matlab software, which is based on the theory and methodology detailed in ref (101). The physical parameters such as conductivity, permittivity and permeability of each layer are used to compute its chain matrix at each frequency. Those matrices are next multiplied in order to simulate a stack of layers, taking into account the thickness of the layers. The resulting matrix is converted back into S-parameters. The absorption index defined above can indeed be rewritten as a function of the measured or computed S-parameters as:

$$A = 1 - |S_{21}|^2 - |S_{11}|^2 \qquad \textit{eq. III-5}$$

As an example, analytical simulations in Fig. 8 compare a few types of absorbers composed of 12 conductive layers 5µm thick, alternatively stacked between 13 dielectric layers 300µm thick. The conductive layers of the first system are arranged in a linear gradient of conductivity (from 1 to 1999S/m by step of 181.6S/m) while, in the second system, they have the same fixed conductivity. The average conductivity of those two examples is identical and equal to 10^3S/m. Fig. 8 shows a significant difference of absorption in favour of the gradient multilayer. Complementary simulations show the absorption index for the two multilayers with constant conductivity fixed either at the maximum value $\sigma = 1999\mathrm{S/m}$ or the minimum value $\sigma = 1\mathrm{S/m}$. In the latter case, conductivity is insufficient for significant absorption but, on the other hand, high conductivity leads to reflection instead of absorption. A fine balance of conductivity combined with a gradual increase is the most efficient system.

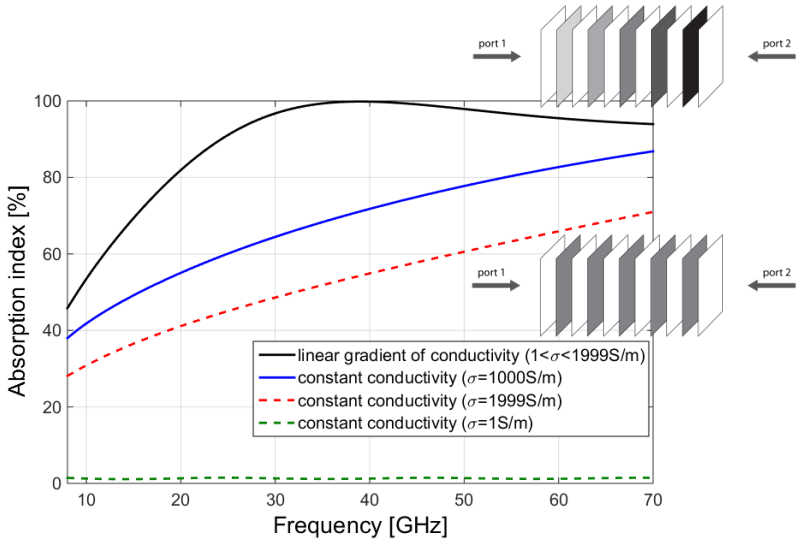


Fig. 8. simulation of a gradient conductivity stack compared with constant conductivity systems. The systems have 12 conductive layers 5 µm thick and 13 dielectric layers 300µm thick. The inset shows a pile in gradient of conductivity of dielectric (white) and conductive (grey) layers.

Making a gradient system requires producing a series of thin films with finely controlled conductivity. In this research, we propose two versatile solutions to this problem, one based on CNT-PC nanocomposites and another using CNT water-based ink deposited on PC substrates.

1.2. Limit and classification of absorbing structures

The Rozanov limit

The theory of absorption suggests at first glance that a perfect absorber working at any frequency band could be created in such a way that the coefficients of reflection and transmission are zero. This requires basic conditions such as $\varepsilon_r = \mu_r$ (see *eq. III-4*) and as large as possible imaginary parts of these quantities (see *eq. III-2*). However, these coefficients cannot be selected arbitrarily because the frequency dependencies of the real and imaginary parts of permittivity and permeability of any actual material are correlated to each other by means of the Kramers-Kronig relations (46). These relations imply that the frequency dependence of material constitutive parameters prohibit the

conception of a perfect absorber. The maximum absorption index can nevertheless be calculated via the Rozanov equation.

The limit of a microwave absorber is determined by the Rozanov method (46), which is often used for radar absorption. The formalism assumes a plane monochromatic electromagnetic wave which is normally incident to an infinite plane of perfect conductive surface coated with the absorber. Indeed, the analysed samples have to be metal-backed to reflect all energy towards the incoming port. The back side metal foil is assumed to act as a perfect electric conductor to fulfil the conditions of applicability of the Rozanov formalism. So, the reflection coefficient $R(\lambda)$ contains all information about the absorbed energy as a function of wavelength (no term of transmission is involved). The following equation, built on Kramers-Kronig relations applied on $R(\lambda)$ (102) and Fresnel theory (103) (details are given in ref (46)), shows the limit of reflection of any material back-covered by a perfect reflector:

$$\left| \int_0^{\infty} \ln|R(\lambda)|\, d\lambda \right| \leq 2\pi^2 \mu d \qquad \textit{eq. III-6}$$

where λ is the wavelength, μ and d respectively are permeability and thickness of the absorbing material. This inequality *eq. III-6* can be readily extended to the case of a multilayer slab. Insofar as the thickness of each layer is much lower than wavelength λ, the multilayer slab can be treated as a stratified medium and be characterised by the effective permeability of each independent layer (103). Furthermore, the integral must be reduced to a measurable range of wavelength (from λ_i to λ_f). It quickly yields to the so-called Rozanov equation:

$$\left| \int_{\lambda_i}^{\lambda_f} \ln|R(\lambda)|\, d\lambda \right| \leq 2\pi^2 \sum_n \mu_n d_n \qquad \textit{eq. III-7}$$

We impose an approximation here since, on one hand, the integral does not apply any more over an infinite frequency range, and, on the other hand, the wavelengths must be larger than the thicknesses d_n. For those reasons, the experimental characterisation is preferably performed over a broad frequency range and with the condition: $\lambda \gg d$. This is in agreement with the recommendations of the Rozanov formalism. It favours longer wavelengths and thinner samples which is by the way relevant because it reflects the practical challenge to extend the operating absorption spectrum. Current radar absorbers are known to have very

high performance over a narrow frequency band (104). A narrow absorption band is penalised as well a large thickness by the Rozanov formalism (105). The integral of the reflectance over a given wavelength range provides the upper theoretical limit for a given structure. We are now able to locate an absorber with respect to the ultimate limit. The multilayers of this thesis are compared to the Rozanov limit in section V-1.3 and V-2.2. However, this formalism is not adapted for a general comparison between different absorbers. So, a complementary classification based on a figure of merit (FOM) is introduced in the next section.

Classification of absorbers by a figure of merit

Performance criteria for absorbers depend on the targeted purpose. In this work, we will concentrate on the range 8.2-67GHz corresponding to the spectrum fully accessible with our equipment. The objective is to maximise the absorption index for a minimal thickness of the multilayers. It is then relevant to set the following formula as figure of merit Q:

$$Q = \int_{\lambda_i}^{\lambda_f} \frac{A(\lambda)}{t} d\lambda \qquad \textit{eq. III-8}$$

where λ is the wavelength, $A(\lambda)$ is the absorption index and t is the total thickness of the multilayer. The factor of merit is higher for absorption close to 1 over as large as possible a spectrum. Moreover, it is favoured if the thickness is small. As reference, the upper limit of an ideal perfect absorber is $Q = \frac{0.0321}{t}$ over the considered spectrum. Of course, no real structure has the ideal property of absorption, and the equation *eq. III-8* is unable to provide any physical upper limit. It is thus interesting to compare a characterisation of the multilayers, in one hand, with the FOM and, in the other hand, from the Rozanov formalism to know the position with regard to the physical limit.

1.3. Electromagnetic bandgap (EBG) absorption/reflection by EM resonance

The "simple" absorber is now modified to explore an avenue to other applications. A multilayer absorber can be modified to open narrow bands of reflection or absorption at desired frequencies. Such a feature is possible by changing the geometric parameters of the structures described above. Indeed, the choice for the thickness and permittivity of the insulating films influences the position of the minima or maxima in the absorption spectrum. Actually, the dielectric layers are used to create a constructive or destructive resonance at a given frequency. It can be considered that the basic structure of the filter is a dielectric layer surrounded by two conductive films. The wave is partially "trapped" in the dielectric layer acting as a resonator. The multilayer thus forms a series of resonators in order to amplify the effect of each. The conductivity of the conductive layers is adjusted so that the transmission and reflection of the microwave is controlled. Two opposite behaviours are possible via the multilayer EBG: either a broadband absorber with narrow reflecting windows or a reflective coating with some absorption peaks acting as a frequency selective surface (FSS). Both are considered below.

EBG with narrow reflection windows

This first type of filtering structure absorbs the entire spectrum with the exception of a weak-absorption peak at defined frequencies. Actually, the transmission is low for the entire spectrum; only the reflectivity drastically rises on a very narrow band. In this work, the conductive layers can either be obtained in the form of polycarbonate - carbon nanotubes (PC-CNT) nanocomposite films or as CNT-based ink coatings on neat PC films (see section V-4.1). Such structure can, for instance, function as a prefilter for an incoming signal, e.g. on a parabolic antenna. It is made from flexible and resistant materials conceivable for large and outside application. Scientific literature is poor about EBG with narrow reflection peaks. Researches have been done on this field but they operate at much higher frequencies (106) (107). Some structures have been performed for GHz range but they are complex and fragile (57).

The dielectric layers are the dominant building blocks in the creation of narrow reflection peaks. It appears when their thickness is close to

$$t_{sub} = \frac{n}{2} \frac{c}{f\sqrt{\varepsilon_{sub}\mu_{sub}}} \qquad \textit{eq. III-9}$$

where t_{sub}, ε_{sub} and μ_{sub} are the thickness, the permittivity and the permeability of the substrate respectively, f is the frequency and $n \in \mathbb{N}^0$ as demonstrated in ref (18). This condition implies a constructive resonance between couples of conductive layers. The simulation in Fig. 9a shows the evolution of weak-absorption bands as a function of the thickness of the dielectric layers and frequency. The multilayer consists of 8 layers of dielectric films sandwiched by thin conductive layers which are stacked in a gradient of conductivity. For simulation, the permittivity of the dielectric layer is 1 in order to maximise the global absorption index (see section III-1.1). Of course, the advantage gained in absorption is lost in terms of total thickness of multilayer. On the left of Fig. 9, S-parameters and absorption graphs are given for a dielectric thickness fixed at 7.5 mm. The "fundamental" absorption peak appears at 20 GHz, followed by its harmonics. Fig. 9c shows that transmission (S_{12} and S_{21}) is very low in high absorption frequency range; the reflection S_{11} is weak except at resonance where the reflection jumps. The variations of S_{11} are significant in dB and give the shape of the absorbed power $P_{1\to2}$.

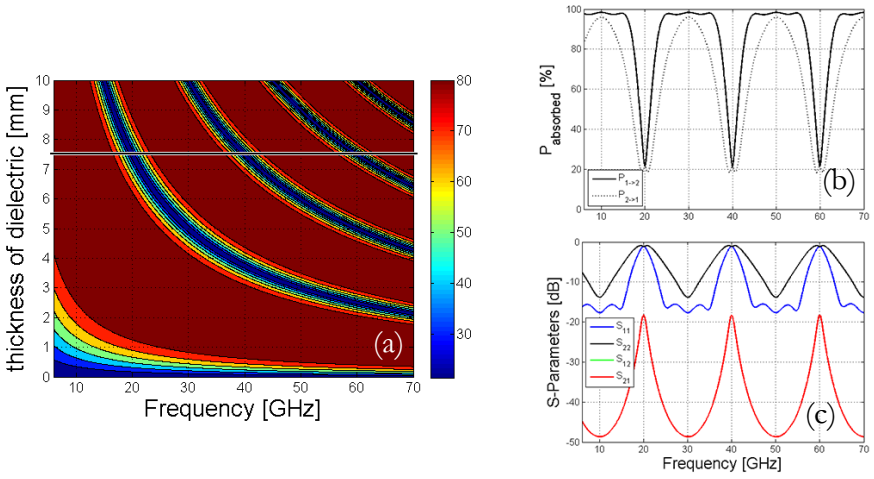


Fig. 9. simulation of absorption according to frequency and thickness of dielectric layer in (a). The multilayer is composed of 8 dielectric layers whose permittivity is 1. The 9 conductive layers are 6µm thick and the average conductivity is $50 < \sigma < 1800 S/m$ for

an average conductivity of 900S/m. The graphs on the right show the absorption index in (b) and S-parameters in (c) for a selected thickness of 7.5mm.

The simulations in Fig. 9 are carried out with CNT composites and polymeric substrates as shown in section V-4.1. The selection of the thickness or permittivity of the dielectric layers allows a complete freedom of the choice of filtered frequency.

FSS with narrow absorption peaks

The complementary structure possible is a filter absorbing one frequency (and its harmonics) over the spectrum and reflecting the rest. We adapt the previous structure so as to create some narrow windows/gaps in the spectrum where absorption jumps. In our implementation, the conductive layers are still CNT-based ink coatings on neat polycarbonate (PC) films. The dielectric layers require a high permittivity material in order to minimise the total thickness (see *eq. III-10*). We use a high-ε polymeric substrate or a ceramic such as concrete or granite. Indeed, construction materials are very efficient to build microwave frequency selective surfaces (FSS). The FSS built in this study aims to shield the massively used band of 2.4GHz which corresponds to Wi-Fi network frequency (see section V-4.2). The Wi-Fi frequency has been chosen as an interesting and challenging illustration for microwave FSS. Furthermore, the scientific literature is quite poor in this frequency range. On the other hand, the MHz is relatively well controlled for absorption (108) (109). FSS and EBG filters are mainly developed for frequencies around plasmonic oscillations (110) or higher (111). Wi-Fi shielding usually requires specific and particularly thick (usually foamed) materials (112) without the advantage of the selection of a FSS. The uses of construction materials such as concrete or granite allow considering large shielding areas at low cost.

For EBG with narrow absorption peaks, a gradient of conductivity stacking is not optimal. The absorption peaks are significantly larger for a system with constant conductivity. The dielectric spacers produce an absorption peak at frequencies verifying

$$f = \left(\frac{1}{4} + \frac{n}{2}\right)\frac{c}{t_{sub}\sqrt{\varepsilon_{sub}\mu_{sub}}} \qquad \textit{eq. III-10}$$

where t_{sub}, ε_{sub} and μ_{sub} are the thickness, the permittivity and the permeability of the substrate respectively, f is the frequency and $n \in \mathbb{N}$. This is the condition to induce an interference between two conductive layers. Fig. 10 is a simulation of a multilayer composed of 4 dielectric layers with high permittivity ($\varepsilon = 10$ and 1.2mm thick) sandwiched between 3 conductive films ($\sigma = 10^4 S/m$ and 6µm thick). The other wavelengths undergo a high reflection as shown by the S_{11} parameter. Note that the variations of S_{12} are minor in dB.

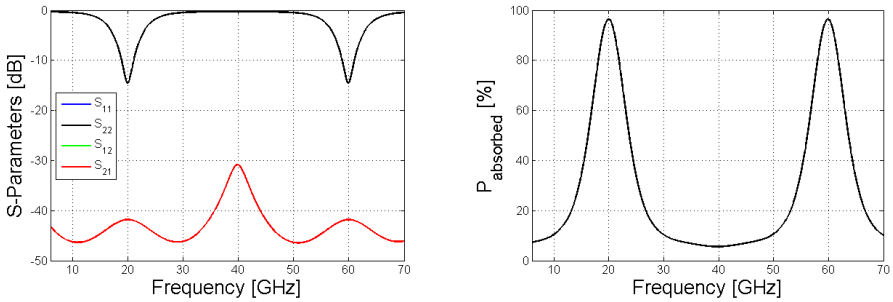


Fig. 10. simulation of a multilayer of 4 dielectric layers 1.2mm thick and whose permittivity is 10. The 3 conductive layers are 6µm thick and their conductivity is 10^4S/m.

The example of high absorption peaks in Fig. 10 shows the feasibility of such an EBG with thin CNT composite films and dielectric slabs. The method is of course applicable at other frequencies as proved in section V-4.2 by Wi-Fi frequency filter. Our structure fills a significant gap in the state of the art and offers an original and smart combination of materials.

1.4. Operating on S-parameters

S-parameters are widely used to characterise the propagation of high frequency signals into materials, electron devices, circuits and communications systems. They describe the input-output relationship between ports (or terminals) in an electrical system. In general, S_{nm}

represents the power transferred from port m to port n in a multi-port network. For instance, if we have 2 ports (called port 1 and port 2), then S_{12} represents the power transferred from port 2 to port 1; S_{11} represents the power reflected onto port 1 itself. Referring to Fig. 11, port 1 emits a wave having a frequency f and intensity a_1. The reflected intensity b_1 is measured at port 1 and the transmitted intensity b_2 at port 2. It is then possible to calculate the S-parameters, S_{11} corresponding to the intensity ratio $\frac{b_1}{a_1}$, while S_{21} corresponds to the ratio $\frac{b_2}{a_1}$. Port 2 also sends the same wave in order to determine S_{22} and S_{12}.

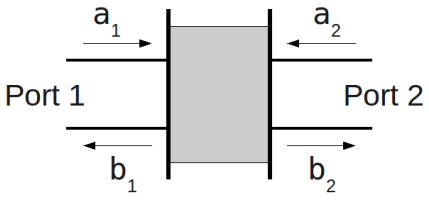


Fig. 11. scheme of input and output ports of a vectorial network analyser

S-parameters are complex numbers taking into account the magnitude of received energy (real part) and the phase of the wave (imaginary part). The complex S-parameters contain all necessary information to characterise a material. It means that it is theoretically possible to extract from them the complex permittivity and complex permeability (see paragraph III-1.6) or simply quantify the absorption index. The S-parameters are measured by a vectorial network analyser (VNA). It is used mostly at high frequencies, for a range from a few MHz up to THz. The standard is using 2 ports (as shown in Fig. 11) but an arbitrary number of ports can be used.

1.5. Simulation by chain matrix

Simulation of mono- or multi-layered materials is possible thanks to a Matlab code developed at UCL. This routine simulates the S-parameters based on the physical properties of each film. Each layer is treated like a transmission line with associated characteristic impedance Z_c and propagation constant β (see Fig. 12). The layers are assumed isotropic in the three spatial dimensions. 50 Ω impedances are placed at

port 1 and 2 on each side ports to account for the internal reference impedance of the Vector Network analyser (VNA).

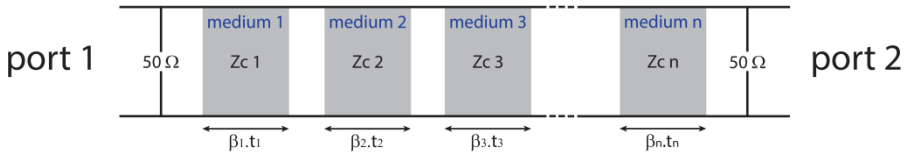


Fig. 12. equivalent circuit of impedances simulating successive media of a multilayer

Basically, we enter the values of relative permittivity ε_r', conductivity σ, relative permeability μ_r and thickness d of each layer. The routine is optimised to repeat sequences of alternating bilayers since they are the key to an efficient absorption system (presented in paragraph III-1.1). Layer by layer, the physical parameters are converted to a chain matrix by the following equations:

$$\begin{cases} \varepsilon_r = \varepsilon_r' - \dfrac{i\sigma}{\varepsilon_o \omega} \\ \gamma = \dfrac{i\omega}{c}\sqrt{\varepsilon_r \mu_r} \\ Z_C = \sqrt{\dfrac{\mu_o}{\varepsilon_o}}\sqrt{\dfrac{\mu_r}{\varepsilon_r}} \end{cases} \rightarrow \quad T = \begin{pmatrix} \cosh(\gamma d) & Z_c \sinh(\gamma d) \\ \dfrac{1}{Z_c}\sinh(\gamma d) & \cosh(\gamma d) \end{pmatrix} \qquad \textit{eq. III-11}$$

Relative permittivity ε_r is treated as complex entity from the given ε_r' and σ values; relative permeability μ_r may directly be introduced as complex number. The propagation constant γ and characteristic impedance Z_c are determined and used for the conversion into chain matrix T. The interest of the chain matrices is the simplicity to simulate a series of impedances by multiplication of matrices. Matlab is very efficient for the treatment of matrices, hence computing the equivalent chain matrix goes fast. The equivalent matrix T_{total} of the entire multilayer must next be converted back to S-parameters. This conversion to S-parameters is done as follows:

$$T_{total} = \begin{pmatrix} A & B \\ C & D \end{pmatrix} \rightarrow S_{total} = \begin{pmatrix} S_{11} & S_{12} \\ S_{21} & S_{22} \end{pmatrix}$$

$$= \begin{pmatrix} \frac{Z_1 + B - C\overline{Z_1}Z_2 - D\overline{Z_1}}{AZ_1 + B + CZ_1Z_2 + DZ_1} & \frac{2(AD - BC)\sqrt{\Re\{Z_1\}\Re\{Z_2\}}}{AZ_1 + B + CZ_1Z_2 + DZ_1} \\ \frac{2\sqrt{\Re\{Z_{n1}\}\Re\{Z_{n2}\}}}{AZ_1 + B + CZ_1Z_2 + DZ_1} & \frac{-A\overline{Z_2} + B - CZ_1\overline{Z_2} + DZ_1}{AZ_1 + B + CZ_1Z_2 + DZ_1} \end{pmatrix}$$

eq. III-12

where Z_1 and Z_2 are respectively port 1 and port 2 impedances (which are 50Ω here). The overall S-parameters are generally used to calculate the absorption index of a multilayer. The direction of measurement is significant for non-symmetric stacks of layers. The *eq. III-5* gives absorption for characterisation from port 1 to port 2, the absorption index in the opposite direction is

$$A_{2\to1} = 1 - |S_{12}|^2 - |S_{22}|^2 \qquad \textit{eq. III-13}$$

S-parameters contain all the necessary information to know the physical properties of the material being measured. The computer processing to extract them is complex. The following paragraph focuses on the mathematical development to derive ε'_r, σ and μ_r from raw S-parameters.

1.6. Extraction of physical parameters from raw S-parameters

S-parameters as measured by a VNA are four complex numbers (S_{11}, S_{12}, S_{21} and S_{22}) that describe the phase and amplitude in both directions of the sample at each frequency. These values give the signature of the material. It is thus possible to extract essential data to characterise the produced films. This inverse calculation (in the usual sense of inverse models) requires analytical equations that must be integrated into Matlab.

Nicolson model

A commonly used model is the method of A. M. Nicolson (113) which has been completed by William B. Weir (114). The Nicolson

method is useful for the measurement of the transmission and reflection scattering coefficients of microwave networks by Fourier analysis. It is demonstrated that the method can reduce errors due to mismatch of the components of the measurement system. For very broadband measurements with moderate resolution, the method has a potential accuracy of about Â±0.1 dB and Â±1Â°, with a significant reduction in mismatch errors (113). W. B. Weir improves the model by solving the inaccurate determination of the wave phase. The imaginary part of propagation coefficient of a complex quantity is equal to the angle of the complex value plus $2\pi n$, where n is equal to the nearest integer to the ratio of the length of the sample divided by the transmission line guide wavelength. The phase ambiguity is then resolved by finding a solution for permittivity and permeability from which a value of group delay is computed that is compatible with measured data at two or more frequencies. Other models follow the same reasoning with a variant to define the integer n. Indeed, the reliable calculation of n is difficult to achieve. The code should yield a correct integer n in spite of the unavoidable fluctuations of electromagnetic measurements. A bad choice of n indirectly induces a jump of at least 2π in the imaginary part of permittivity and permeability. That's why a lot of models have been developed for approaching the correct phase angle. J. Huixin uses the "phase jump" method to determine n (115), Y. Guang gives a new method to get the reflection coefficient more exactly when the reflection scattering coefficient (S_{11}) is too small (116). A.-H. Boughriet uses improved equations for better agreement of the complex permeability and permittivity with the sample (117). In this thesis, we use the method of A. M. Nicolson supplemented by the method described in ref (118). The complete mathematical derivation is given hereafter.

The extraction process of ε_r, σ and μ_r starts from S-parameters provided by the VNA. For an isotropic material, these are defined as

$$S_{11}(\omega) = \frac{(1 - T^2)R}{1 - R^2T^2} \qquad \textit{eq. III-14}$$
$$S_{21}(\omega) = \frac{(1 - R^2)T}{1 - R^2T^2}$$

where T is transmission and R reflection coefficient (detailed by *eq. III-2* and *eq. III-4*). We define

$$X = \frac{1 - S_{21}^2(\omega) - S_{11}^2(\omega)}{2S_{11}(\omega)} \qquad \textit{eq. III-15}$$

The reflection coefficient becomes

$$R = X \pm \sqrt{X^2 - 1} \qquad \textit{eq. III-16}$$

where the appropriate sign is chosen so that $|R| \leq 1$ (118). When R is defined, we compute the transmission coefficient

$$T = \frac{S_{11} + S_{21} - R}{1 - (S_{11} + S_{21})R} \qquad \textit{eq. III-17}$$

Now that T and R are known, it is easy to find, thanks to *eq. III-2* and *eq. III-4*, the following relationship:

$$\begin{cases} c_1 = \sqrt{\frac{\mu_r}{\varepsilon_r}} = \frac{1 + R}{1 - R} \\ c_2 = \sqrt{\mu_r \varepsilon_r} = -i\frac{c}{\omega d}\ln\left(\frac{1}{T}\right) \end{cases} \qquad \textit{eq. III-18}$$

It then becomes possible to obtain the complex entities ε_r and μ_r. We immediately see that there is an unavoidable ambiguity about the signs. For instance, if ε_r only is negative, the equations do not unambiguously assign this sign to permittivity rather than permeability, and vice versa. This method does not work for the materials of the so called "double negative" or "left hand" region of the metamaterial chart. Indeed, if ε_r and μ_r are negative, the sign of c_1 and c_2 is necessarily positive and the information is lost. Supplements to the Nicolson method found in the literature often prove ineffective. At best, it is possible to determine the correct sign of the physical quantities in each part of the spectrum but the algorithm is not able to handle a change of sign in the spectrum. This is unfortunately problematic for materials that go from negative to positive permittivity as the frequency increases. On the other hand, the undeniable strength of this method is its accuracy in terms absolute values of ε_r and μ_r and its robustness with respect to measurement noise. Since the sign of these physical quantities is essential in the context of this thesis, another method is discussed below.

Kramers-Kronig based model

The second procedure invokes the Kramers-Kronig relations to ensure the uniqueness of the solution (119). Indeed, this algorithm provides the wave impedance and the imaginary part of the refractive index with the right sign from S-parameters. It requires a cumbersome iterative method based on Taylor series in order to determine the real part of the refractive index. In addition, when the usual passive material conditions $\Im\{\varepsilon\} \geq 0$ and $\Im\{\mu\} \geq 0$ are imposed, the method cannot find the material effective parameters for some frequency regions (120). However, as it has been pointed out in ref (121), the magnetic and electric dipoles induced in metamaterials are not independent of each other, and the passivity condition can be fulfilled even when $\Im\{\varepsilon\} \leq 0$ or $\Im\{\mu\} \leq 0$. Relaxing this condition allows us to calculate effective parameters in AC (119).

This second method starts from same *eq. III-14* for S-parameters. The reflection and transmission coefficients are related to the effective refractive index N_{eff} and effective impedance Z_{eff} (96).

$$\begin{cases} R = \dfrac{Z_{eff} - 1}{Z_{eff} + 1} \\ T = e^{-\frac{iN_{eff}\omega d}{c}} \end{cases} \qquad \textit{eq. III-19}$$

It has been pointed out in ref (120) that the refractive index N_{eff} and impedance Z_{eff} are obtained by inverting *eq. III-14* with the help of *eq. III-19*. It gives:

$$\begin{cases} Z_{eff} = \pm\sqrt{\dfrac{(1+S_{11})^2 - S_{21}^2}{(1-S_{11})^2 - S_{21}^2}} \\ e^{-\frac{iN_{eff}\omega d}{c}} = X \pm i\sqrt{1-X^2} \end{cases} \qquad \textit{eq. III-20}$$

where $X = \frac{1}{2S_{21}(1-S_{11}^2+S_{21}^2)}$. Since the metamaterial under consideration is a passive medium, the signs in *eq. III-20* are determined by the requirement

$$\begin{aligned} \Re\{Z_{eff}\} &\geq 0 \\ \Im\{N_{eff}\} &\leq 0 \end{aligned} \qquad \textit{eq. III-21}$$

The value of refractive index N_{eff} can be determined as

$$N_{eff} = \frac{c}{\omega d}\left(\left(\Im\left\{\ln\left(e^{-\frac{iN_{eff}\omega d}{c}}\right)\right\} + 2m\pi\right) - i\Re\left\{\ln\left(e^{-\frac{iN_{eff}\omega d}{c}}\right)\right\}\right) \qquad \textit{eq. III-22}$$

where m is an integer related to the branch index of $\Re\{N_{eff}\}$. As mentioned above, the imaginary part of N_{eff} is uniquely determined, but the real part is complicated by the branches of the logarithm function. If we separate the real and imaginary parts of the above expression (as $N_{eff} = n_{eff} + i.\kappa_{eff}$), the refractive index and the extinction coefficient become

$$\begin{cases} n_{eff} = \dfrac{c\,\Im\left\{\ln\left(e^{-\frac{iN_{eff}\omega d}{c}}\right)\right\}}{\omega d} + \dfrac{2m\pi}{\omega d}c = n_{eff}^{o} + \dfrac{2m\pi}{\omega d}c \\ \kappa_{eff} = -\dfrac{\Re\left\{\ln\left(e^{-\frac{iN_{eff}\omega d}{c}}\right)\right\}}{\omega d}c \end{cases} \qquad \textit{eq. III-23}$$

where n_{eff}^{o} is the refractive index corresponding to the principal branch of the logarithmic function. The parameter extraction procedure takes advantage of the fact that the imaginary part of the refractive index is not affected by the branches of the logarithmic function. Therefore, it can be calculated without ambiguity. Knowing the imaginary part of the refractive index, we can determine the real part thanks to Kramers-Kronig relation. This relationship connects the real part and the imaginary part of any complex functions. It provides for the real part of N_{eff} :

$$n_{eff,KK}(\omega) = \frac{2}{\pi}\int_0^{\infty} \frac{\Omega\kappa_{eff}(\Omega)}{\Omega^2 - \omega^2}\,d\Omega \qquad \textit{eq. III-24}$$

The integral is bound between 0 and ∞ following the theory. Actually, it is impossible to measure S-parameters over the entire frequency range. The integral must be truncated and the Kramers-Kronig relations yield an approximation of the refractive index. For accuracy, the range of the integration should be as large as possible. On the other hand, if the frequency range becomes too large, we may reach a point where the concept of effective parameters is no longer meaningful when the guided

wavelengths are on the order of the characteristic dimensions of the metamaterial structure.

The integration of *eq. III-24* can be performed numerically by applying the trapezoidal rule of integration. The branch m is computed by substituting the refractive index predicted by the Kramers–Kronig relation. We use the Matlab function *round* to determine the nearest integer for m

$$m = \mathrm{round}\left(\left(n_{eff,KK} - n_{eff}^{o}\right)\frac{\omega d}{2\pi c}\right) \qquad \textit{eq. III-25}$$

So, the closest value predicted by the Kramers-Kronig relation is selected to calculate the refractive index. The branch number m is substituted in *eq. III-25* to get the right value of the refractive index. The algorithm then checks the continuity of the refractive index N_{eff}. A discontinuity close to the limit of the calculation zone may be caused by the truncation error in the Kramers-Kronig integral. If the discontinuity is far from the limits of the covered frequency range and the discontinuity is persevered even when the frequency interval of the simulation is increased, this indicates that the limit of the effective medium theory has been reached (119). We finally obtain the complex form of ε_r and μ_r by the relations:

$$\begin{cases} N_{eff} = \sqrt{\varepsilon_r \mu_r} \\ Z_{eff} = \sqrt{\dfrac{\mu_r}{\varepsilon_r}} \end{cases} \qquad \textit{eq. III-26}$$

Discussion of the models

Both models presented above have each advantages and limitations. Nicolson's model is very accurate and stable even with a very small number of measurement points. Ten points often are enough to give a graph well-fitting input values. However, the model is unable to handle a change of sign of permittivity or permeability. The passage of ε (or μ) from negative to positive values implies a wrong overall estimate of three physical parameters. The Kramers-Kronig model overcomes this

ambiguity by determining exactly the real part of the refractive index. However, the accuracy of n_{eff} depends on the integer m, itself extracted by the Kramers-Kronig integral. This integral is defined on a finite frequency range and generates imprecision. We see here the limits of the model. If m is poorly determined, the following operations will be inaccurate. The model has therefore been consolidated to minimise the risk of choosing a wrong m branch.

Nicolson's model is completely reliable in a wide range of cases. Typically when ε_r and μ_r are constant, this model is the most suitable. Nicolson's model gives only the absolute value of ε_r and μ_r, while the Kromers-Kronig model remains reliable up to the sign. The Kamers-Kronig code is preferably used for its ability to manage complex behaviour of ε_r and μ_r. The reliability of this model is controlled by analysing the behaviour of the intermediate calculations, i.e. the real and imaginary part of Z_{eff} and N_{eff}. If they do not undergo unexpected jump, it means that m branches have been properly determined. In practice, both models are used to exploit all information. Let's assume an extraction of ε_r, σ and μ_r graphs via S-parameters. If both models agree, reliability is anticipated. On the other hand, the situation can be that the Kramers-Kronig model displays one or more jumps in those extracted graphs. It is then obvious that the areas of disagreement with the Nicolson model are due to a wrong choice of the m branch and the analysis must take into account that the Nicolson model displays the absolute value of the material parameters. The ideal extraction procedure runs the two models in parallel. For each S-parameter extraction, a comparison between the models is carried out in order to estimate the reliability. The majority of the measurements obviously give identical results with both models. For those rare situations where a part of the spectrum raises a question, additional simulations are performed to disambiguate the results.

1.7. Nanoparticles-polymer composites

The efficiency of composites for EMI shielding is strongly related to the nature of the charges (always called "fillers" in polymer science literature), their concentration and their dispersion. They must be conductive to qualify for absorption enhancement. The aspect ratio also plays an important role in the creation of a percolating network. Slender nanocharges facilitate percolation at a lower concentration. The selection

of the charges in terms of nature, shape and affinity with the polymer matrix is thus primordial for maximal efficiency, i.e. sufficient conductivity at the lowest possible filler concentration. High filler concentration is indeed almost always linked to reduced mechanical properties and increased cost.

Efficiency of nanowire charges in polymer composites

Polymer nanocomposites are a new class of hybrid materials that are particle-filled polymers in which at least one dimension of the dispersed component is below 100nm. The reduction of particle size obtained in such materials increases the specific surface area of the filler, providing a larger matrix/filler interface and so more mutual interactions (122). As a result, a large reinforcing effect may be reached at much lower filler content when compared to classical microcomposites (123). Besides, the geometrical shape of the particles plays an important role in determining the properties of nanocomposites (124).

Three types of nanocomposites are distinguished depending on how many dimensions of the dispersed filler are in the nanometric scale (see left schemes on Fig. 13). "Zero-dimension" charges such as carbon black or isotropic inorganic nanoparticles need a high concentration to percolate (31). Intuition suggests (and theory shows) that anisotropic nano-objects will be more effective to create a connected network through the matrix. Fig. 13 compares the conductivity of a polycarbonate composite reinforced with 5% by weight of carbon black (0D), carbon nanotubes (1D) or exfoliated graphite (2D). Conductivity is measured in the AC regime to fit with further investigations explained in details in section V-1.1. The highest effective conductivity at a given nanofiller concentration is found for carbon nanotubes (CNT) whereas graphene has a higher intrinsic conductivity than CNT. The concentration threshold for high electrical conductivity is indeed the lowest for one-dimensional particles (125). Large platelets such as graphene nanoplatelets (GNP) do not as easily create an electrical network. We say that the network is percolating or not. GNP needs a higher concentration to reach the percolation threshold. Carbon black (CB) is even less effective to percolate as shown by Fig. 13[1].

[1] polycarbonate-carbon black composite was provided by A.-C. Baudouin.

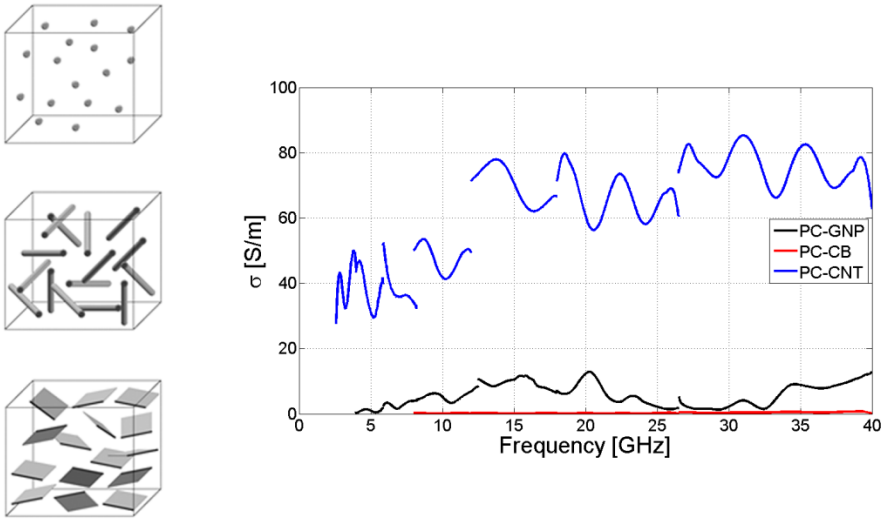


Fig. 13. representation (on left) of the three types of nanocomposites: 0D nanoparticles, 1D nanotubes/nanowires, 2D nanosheets. Conductivity in AC regime is given for polycarbonate (PC) composite reinforced with 5%wt. of carbon black (CB), carbon nanotubes (CNT) or graphene nanoplatelets (GNP).

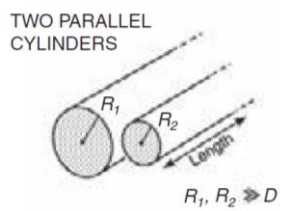
The wire-shape is the best choice for electrical percolation at low concentration (125). The nature of the particles also plays an important role in effective conductivity. Carbon nanotubes are excellent conductors and their aspect ratio is of the order of 10^2. They have an exceptional mechanical strength and they are relatively cheap (126). Metallic nanowires (such as gold nanowires) present interesting properties too. Their conductivity is more or less comparable with that of CNT (depending on the type of CNT). Their aspect ratio reaches the same or even higher values (details in section IV-1.2). Metallic nanowires-polymer composites are analysed in the section V-2.4. Besides the nature and aspect ratio of the charges, their dispersion inside the polymer matrix is preponderant. The challenge is to disperse homogeneously and bypass the attractive forces favouring the formation of clusters.

Dispersion in polymer matrix

The dispersion of CNT or nanowires is crucial for electrical percolation at an acceptable concentration of the conductive loads. The fillers should be homogeneously dispersed through the entire matrix. It

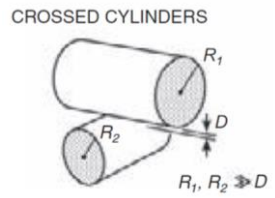
is necessary to overcome the van der Waals (vdW) attraction to avoid segregation of clusters of fillers. In the case of CNT, vdW interactions are due to the high polarisability of the tubes. Depending on the CNT size and mutual orientation, the vdW attraction can act on distances up to a few nanometers (127). It is therefore essential to tackle the mechanisms of interaction in order to select an appropriate polymer and manufacturing process.

Thermodynamics shows that entropic effects are dominated by conformation loss of macromolecules close to the nanotubes, and that enthalpic effects are dominated by van der Waals interactions for native nanotubes (128). The vdW interaction between two mesoscopic cylinders of length L, radii r_1 and r_2 and separated by a short distance D are given for parallel and perpendicular case. The Van der Waals interaction energy W can be derived in interaction force F as $F = -\frac{\partial W}{\partial D}$.



$$W = -\frac{A}{12\sqrt{2D^3}}\sqrt{\frac{r_1 r_2}{r_1 + r_2}}$$

$$F = -\frac{A}{8\sqrt{2D^5}}\sqrt{\frac{r_1 r_2}{r_1 + r_2}}$$



$$W = -\frac{A}{6D}\sqrt{r_1 r_2}$$

$$F = -\frac{A}{6D^2}\sqrt{r_1 r_2}$$

Fig. 14. configurations of parallel and perpendicular cylinders with the corresponding interaction energy and force (127)

Fig. 14 provides equations for the interaction energy W and force F between the cylinders, where A is the Hamaker constant. It is defined as $A = \pi^2 C \rho_1 \rho_2$ where ρ_1 and ρ_2 are the number of atoms per unit volume in the two bodies and C is the coefficient in the atom-atom pair potential. The Lifshitz theory allows evaluating the vDW interaction between particles and the influence of the neighbouring particles while

ignoring the atomic structure and treating the bodies as continuous media (129). According to this theory, the Hamaker constant is calculated based on bulk properties such as the dielectric constant ε, and refractive index n. The Hamaker constant evaluated according to this theory applies for all media, as opposed to the conventional expression. The development of this theory is not presented here but can be found in the very complete references (130) and (131) or in (127). The corresponding equation for the Hamaker constant for two identical charges in a polymer is

$$A = \frac{3}{4} k_B T \left(\frac{\varepsilon_{fil} - \varepsilon_{poly}}{\varepsilon_{fil} + \varepsilon_{poly}} \right)^2 + \frac{3 h f_e}{16\sqrt{2}} \frac{\left(n_{fil}^2 - n_{poly}^2 \right)^2}{\left(n_{fil}^2 + n_{poly}^2 \right)^{3/2}} \qquad \textit{eq. III-27}$$

where k_B is the Boltzmann constant, T is temperature, h is the Plank constant, f_e is the main electronic absorption frequency in the UV (typically around $3.10^{15} s^{-1}$), ε_{fil} and ε_{poly} are respectively the dielectric constant of filler and polymer and n_{fil} and n_{poly} are respectively the refractive indexes of filler and polymer. As a first observation, A is always positive and therefore the interaction force F is negative between the cylinders which implies attraction. The permittivities of the chosen polymer and nanofiller must be as close as possible to minimise the Hamaker constant. The same applies for the refractive indices but they vary relatively little from one polymer to another; this is therefore not a major selection criterion. The dielectric constant of the carbon nanotubes is unknown. The transverse dielectric constant for most carbon nanotubes (metallic or semiconducting single wall CNT) is of the order of 10 (132). The longitudinal dielectric constant is of the order of 1000 and 30 respectively for metallic and semiconducting single wall CNT. The value for multiwall CNT is located somewhere between those extremes (133). In short, ε_{CNT} is very high, and much higher than the permittivity of polymers in general! Hence, in order to minimise mutual CNT attraction in a polymer matrix, we must chose a polymer with as high as possible dielectric constant. Experiments previously performed[2] have shown that polycarbonate (PC), polyvinyl chloride (PVC) and polymethyl methacrylate (PMMA), whose ε_r is respectively 3, 3.4, 3.5 in the low frequency limit (DC), are characterised by a good dispersion of multiwall CNT. Conversely, the dispersibility in polypropylene ($\varepsilon_r = 1.5$) is very bad. In this thesis, polycarbonate is used for all composites

[2] collaboration of UCL (A.-C. Baudouin) and ULg (J.-M. Thomassin, C. Detrembleur, C. Pagnoulle, R. Jérôme)

because the CNT dispersion is particularly suited for the desired electromagnetic response. Percolation is quickly obtained and the contacts between CNT provide adequate conductivity.

Conditions for electrical percolation

Percolation is a physical process that describes the brutal transition of a system from a dispersed to a (co-)continuous structure and the corresponding properties changes. In this study, we focus on electrical percolation, or the insulator-conductor transition of a material. The first systems studied from this standpoint in literature consisted of a mixture of conductive and insulating powders, e.g. a blend of polymer and carbon black. The corresponding percolation threshold was found to be very high $p_c \cong 0.30$ (134). As the challenge is to minimise the percolation threshold, CNT or metallic NW are excellent candidates to improve over carbon black. We will first approach the general percolation theory and next try to adapt it to the wire-shaped fillers in order to predict percolation threshold and extrapolate precisely the conductivity as a function of filler concentration.

Let's consider a general percolation system using a grid of sites where each site of the lattice is either in an open state (black point) with probability p, or in a closed state (empty site) with probability $1 - p$ (see Fig. 15). One possible outcome is presented in Fig. 15b where we can observe the formation of clusters, which are not satisfying the condition for percolation. A system is percolating if a path connecting the boundaries via the open sites exists (see Fig. 15c). For a large network, the conductivity is zero if the network does not percolate, namely when $p < p_c$. Forgetting contact resistances between particles, conductivity theoretically tends to the value of the bulk filler when p is significantly higher than p_c (135).

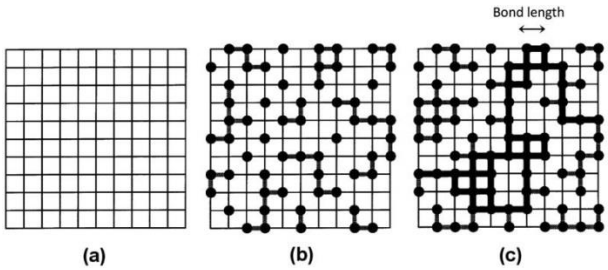


Fig. 15. Grids of sites with open or closed state. (136)

The theory of percolation assumes that the fillers are spheres randomly dispersed in a matrix. This basic model neglects the shape factor and the potential interaction between fillers. However, it is well known that the morphology of conductive fillers has significant effect on the formation of conductive network and the electrical properties of the composite (137). A theoretical study has been devoted to compare the effective conductivity of the composites reinforced by graphene nanosheets (GNS) or CNT (138). Surprisingly, experimental investigations on polymer composites using CNT or GNS have shown different results while the conductivity of their fillers is similar. These contrary results can be attributed to a gap in the current models to consider all parameters involved in the formation of a percolating network. The aggregation of fillers can be incorrectly estimated (139). The percolation threshold of one-dimensional fillers (as CNT or NW) is sensitive to aspect ratio (140). For the two-dimensional fillers (as GNS) or aligned CNT (141), the percolation threshold and conductivity depend on the direction of measurement (142). Moreover, there are many kinds of contact between GNS in a composite: plane to plane, edge to edge (cross or parallel) and edge to plane, among which we can imagine only the plane-to-plane contact is helpful for electrical transfer, while overlapping contact among CNT is the main way in electrical transfer and ensures a high conductivity (139). The factors mentioned above make the modelling of percolation very complex. Actually, at present, no consistent theory is able to model the behaviour of the conductivity as a function of the filler concentration. Experience shows that the correlation between the probability theory of percolation and measured conductivity is only partial (143). The most commonly accepted laws are strictly experimental (144). Empirical power laws are reported in literature to yield reliable fits to experimental data together with an estimation of the percolation threshold for most nanoparticles (143). We will use the formulation:

$$\sigma = k(\phi - \phi_c)^{\mu} \qquad \textit{eq. III-28}$$

where k and μ are fitting constants, ϕ is the weight ratio of reinforcement and ϕ_c is the percolation threshold (143). The constants k, μ and the percolation threshold ϕ_c are defined by fitting experimental data. The formula is applicable for $\phi > \phi_c$, otherwise σ is assumed to be equal to the conductivity of the dielectric matrix. Fig. 16 illustrates a typical graph for a polymer matrix blended with wire-shaped conductive particles.

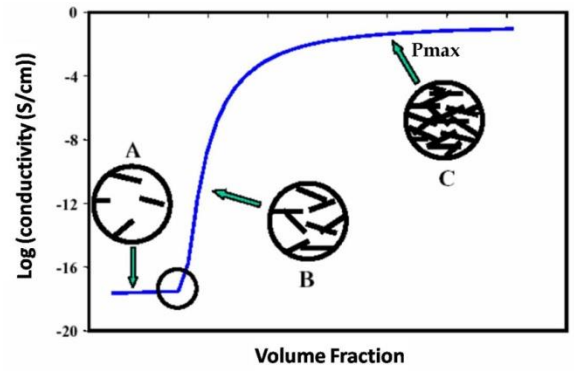


Fig. 16. example of the evolution of conductivity as function of volume fraction of conductive fillers. No conductivity is observed below the percolation threshold, beyond the conductivity follows an experimental power law.

The experimental law (*eq. III-28*) is used in this thesis for fitting independently DC and AC conductivity. In practice, a series of measurements are displayed in a graph and the free parameters are determined by the best corresponding fit. The equation provides an approximation of the percolation threshold and a reliable estimate of the conductivity between experimental points. The percolation theory is a useful tool to determine the best concentration to use in order to produce a composite having the desired conductivity for a given EM application and is used in this work.

2. Invisible cloaking

Recent research focuses on deflecting microwaves rather than absorbing or reflecting them. Pendry et al. (88) and Leonhardt (145) found that the electromagnetic field can be controlled, bent around an interior region and return to their original propagation direction without perturbing the exterior field. Deviation of an EM wave can be achieved by surrounding the structure to be hidden by a shield consisting of layers with a precisely controlled gradient of effective permittivity and permeability (88). Numerous theoretical, numerical and experimental developments have been reported in the last few years (146) (147). The key idea of cloaking is to expand one point or a line segment into a circular or spherical cloaking space. The derivation of the material parameters of the cloaking layer follows the conventional route for design of cylindrical cloaks. The mathematical development is first detailed in the next sections. The method of implementation is afterwards described for a cylindrical invisible cloaking.

2.1. Working principle

Invisible cloaking can be considered if it is possible to generate a curved coordinate system containing an internal region void of EMW. This internal region will be invisible to any incoming radiation A simple way to visualise this is to lay out the curved coordinate lines in the original Cartesian coordinate system. Consider a coordinate transformation from the Cartesian space x^i where $i = 1, 2, 3$ into an arbitrary deformed space described by coordinates $x^{i'}, i' = 1, 2, 3$. Quantities in the corresponding spaces can have physical meaning when

they satisfy corresponding governing equations. Although the two spaces are mathematically identical, we would like to distinguish them by names of virtual space and physical space, respectively, according to their roles. Quantities in the physical space are given notations with prime; while no primes are associated with the virtual space. A spatial region in the Cartesian space that is not passed through by any curved coordinate lines is a void – invisible- region. This situation is illustrated in Fig. 17 with the coordinates before (a) and after transformation (b). The material outside S_1 remains the same in Fig. 17a and Fig. 17b due to the identity transformation in that region of space. In Fig. 17b, a void region has appeared corresponding to a point of zero size in the original coordinate system shown in Fig. 17a. The annular shape bound by S_1 and S_2 in Fig. 17b is electromagnetically equivalent to the region bound by S_1 in Fig. 17a. However their material parameters are different owing to the change of coordinates. A medium obtained through coordinate transformation, such as the illustrated annular shape, is referred to as a transformation medium. So, hiding objects becomes possible since light will be unable to penetrate the void region. In the case where the original space is empty, the resulting transformation medium is an object with anisotropic material properties, which is invisible and at the same time provides shielding to other objects enclosed in S_2.

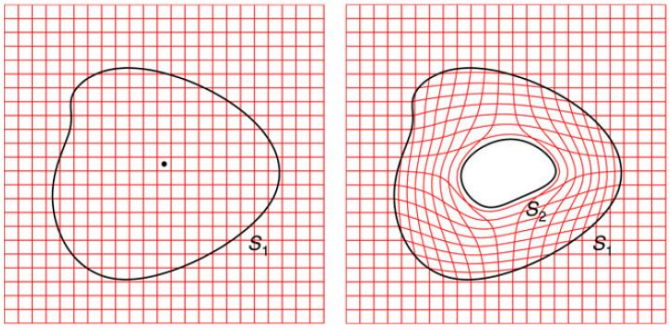


Fig. 17. Illustration of coordinate transformation leading to the cloaking of an arbitrary shape. The original Cartesian coordinate (a) is transformed (b) to introduce an invisible region S_2 by the medium constituting a cloaked between S_1 and S_2. (148)

2.2. Mathematical derivation

The mathematical approach to cloaking can be very general and applicable to a large variety of shapes. As the implementation in this thesis is focusing on a cylindrical shape, the mathematical development is performed for this particular case.

Coordinates transformation

The theory of electromagnetic transformation requires consideration of Maxwell's equations in arbitrary coordinates. This means that the natural mathematical language of transformation media is that of differential geometry, the mathematics that are used to describe curved spaces. The derivation of electromagnetic transformation is largely treated in ref (149). The starting equations are valid in an arbitrary spatial coordinate system defined by x^i where $i = 1, 2, 3$. The transformation is performed to another set of coordinates distinguished from the original by a prime such as $x^{i'}, i' = 1, 2, 3$. We can always switch between the Cartesian coordinates $\{x, y, z\}$ and cylindrical polar coordinates $\{r, \theta, z\}$ by using the following relationships:

$$\{x^i\} = \{x, y, z\} \qquad \{x^{i'}\} = \{r, \theta, z\}$$

$$\begin{cases} x = r\cos\theta \\ y = r\sin\theta \\ z = z \end{cases} \qquad \begin{cases} r = \sqrt{x^2 + y^2} \\ \theta = \arctan\left(\frac{y}{x}\right) \\ z = z \end{cases} \qquad \textit{eq. III-29}$$

We introduce at this point the Einstein summation convention. A summation is henceforth implied over repeated indices, in a product or differential operation, which makes notations much more compact. Summations are generally over a pair of indices in which one index is subscript and one is superscript. An example shows the concept hereafter:

$$a_i b^i \triangleq \sum_{i=1}^{3} a_i b_i = a_1 b_1 + a_2 b_2 + a_3 b_3 \qquad \textit{eq. III-30}$$

The Einstein range convention is also introduced. It means that a free index is understood to range over all possible values of the index.

Indeed, we already wrote x^i implying $\{x^i, i = 1, 2, 3\}$. The summation and range conventions together allow an economy of notation as shown in the following example:

$$a^i_{jik} \triangleq \sum_{i=1}^{3} a^i_{jik} \quad \{j, k = 1, 2, 3\} \qquad \textit{eq. III-31}$$

The set of coordinates x^i and $x^{i'}$ are of course related by the chain rule for differentials:

$$\begin{cases} dx^i = \dfrac{\partial x^i}{\partial x^{i'}} dx^{i'} \\ dx^{i'} = \dfrac{\partial x^{i'}}{\partial x^i} dx^i \end{cases} \qquad \textit{eq. III-32}$$

Differential operators follow the same rule:

$$\begin{cases} \dfrac{\partial}{\partial x^{i'}} = \dfrac{\partial x^i}{\partial x^{i'}} \dfrac{\partial}{\partial x^i} \\ \dfrac{\partial}{\partial x^i} = \dfrac{\partial x^{i'}}{\partial x^i} \dfrac{\partial}{\partial x^{i'}} \end{cases} \qquad \textit{eq. III-33}$$

The transformation matrices corresponding to those operators are noted $J^i_{i'}$ and $J^{i'}_i$. The prime indices are important to differentiate the set of coordinates.

$$J^{i}_{i'} = \frac{\partial x^{i}}{\partial x^{i'}} = \begin{pmatrix} \frac{\partial x}{\partial x'} & \frac{\partial x}{\partial y'} & \frac{\partial x}{\partial z'} \\ \frac{\partial y}{\partial x'} & \frac{\partial y}{\partial y'} & \frac{\partial y}{\partial z'} \\ \frac{\partial z}{\partial x'} & \frac{\partial z}{\partial y'} & \frac{\partial z}{\partial z'} \end{pmatrix} \qquad \textit{eq. III-34}$$

$$J^{i'}_{i} = \frac{\partial x^{i'}}{\partial x^{i}} = \begin{pmatrix} \frac{\partial x'}{\partial x} & \frac{\partial x'}{\partial y} & \frac{\partial x'}{\partial z} \\ \frac{\partial y'}{\partial x} & \frac{\partial y'}{\partial y} & \frac{\partial y'}{\partial z} \\ \frac{\partial z'}{\partial x} & \frac{\partial z'}{\partial y} & \frac{\partial z'}{\partial z} \end{pmatrix}$$

The matrix of first order partial derivatives is called the Jacobian matrix. In vector analysis, the Jacobian matrix is a matrix associated with a vectorial function at a given point. In the case of a curvilinear coordinates system, we cannot define the system base globally. The vectors of base e_i vary with x^i coordinates of a point. However, the Jacobian matrix J provides a linear approximation of this type of transformation in the vicinity of a point; the local base (e_1, e_2, e_3) is simply the triplet of tangent vectors to the coordinate axes. For example, the application of the theory to a Cartesian to cylinder transformation (referring to *eq. III-29*) gives to following matrices:

cylinder to Cartesian: $$J^{i}_{i'} = \begin{pmatrix} \cos\theta & -r\sin\theta & 0 \\ \sin\theta & r\cos\theta & 0 \\ 0 & 0 & 1 \end{pmatrix} \qquad \textit{eq. III-35}$$

Cartesian to cylinder: $$J^{i'}_{i} = \begin{pmatrix} \cos\theta & \sin\theta & 0 \\ -\frac{\sin\theta}{r} & \frac{\cos\theta}{r} & 0 \\ 0 & 0 & 1 \end{pmatrix} \qquad \textit{eq. III-36}$$

This makes sense since $J^{i}_{i'}$ and $J^{i'}_{i}$ are the inverse to each other. It is easy to prove that $J^{i}_{i'}J^{i'}_{j} = \delta^{i}_{j}$, with δ^{i}_{j} the Kronecker delta, because $dx^i = J^{i}_{i'}dx^{i'} = J^{i}_{i'}J^{i'}_{j}dx^j$.

Of course *eq. III-32* and *eq. III-34* can be written in compact form $dx^i = J^{i}_{i'}dx^{i'}$ and $dx^{i'} = J^{i'}_{i}dx^i$. The Jacobian matrix J provides a local

linear approximation of the transformation. The metric tensor G is now introduced to allow calculation of scalar products of the local tangent vectors. This is equivalent to calculate $J^t J$ (150). The metric tensors G under the Cartesian coordinate system are simply δ_{ij} and δ^{ij} but under a curvilinear coordinate system, G is determined through transformation

$$g_{ij} = J^{k}_{i'} J^{l}_{j'} \delta_{kl} \quad \text{or} \quad G = (J^{-1})^t \; J^{-1} \qquad \textit{eq. III-37}$$

Those relationships can be used for coordinate system transformation and tensor transformation. In the course of this section, we have given all useful equations to open a void space for EM waves thanks to the invariance of Maxwell's equations.

Invariance of Maxwell's equations

The method of coordinate transformation can be used to impart a curvature of space (i.e. to generate the closed void volume), but also to calculate the field profile in the transformation medium through Maxwell's equations. Thanks to concepts introduced in the previous section, we are now ready to treat the electromagnetic transformation, namely, the form invariance of Maxwell's equations. Two spaces are treated in parallel, the virtual space and the physical space. The two spaces are univocally related by the coordinate transformation but play different roles when EM fields are introduced. The virtual space is assumed to be filled with an anisotropic medium and its constitutive complex ε and μ parameters. The EM fields characterised by $\vec{E}$, $\vec{D}$, $\vec{H}$ and $\vec{B}$ in this medium follow a trajectory depending on ε and μ satisfying Maxwell's equations.

$$\begin{cases} \vec{\nabla} \times \vec{E} = -\dfrac{\partial \vec{B}}{\partial t} \\ \vec{\nabla} \times \vec{H} = \dfrac{\partial \vec{D}}{\partial t} + \vec{j} \\ \vec{\nabla}.\vec{D} = \rho \\ \vec{\nabla}.\vec{B} = 0 \end{cases} \qquad \textit{eq. III-38}$$

where $\vec{E}$ and $\vec{H}$ are respectively the electric and magnetic fields, $\vec{D}$ and $\vec{B}$ are respectively the electric and magnetic flux and $\vec{j}$ and ρ are respectively

the current and charge densities. The set of *eq. III-38* must be completed by the constitutive equations for full determination of the system:

$$\begin{cases} \vec{D} = \varepsilon_0 \bar{\bar{\varepsilon}}\, \vec{E} \\ \vec{B} = \mu_0 \bar{\bar{\mu}}\, \vec{H} \end{cases} \qquad \textit{eq. III-39}$$

In all generality, permittivity and permeability $\bar{\bar{\varepsilon}}$ and $\bar{\bar{\mu}}$ are order 2 tensors represented by 3x3 matrices. The tensors are physical quantities independent of the coordinate system but their matrix representation depends of course on the vector base. The trick to create the illusion of cloaking is to act on the tensors $\bar{\bar{\varepsilon}}$ and $\bar{\bar{\mu}}$ to force the fields E and H to take a desired path. By using the invariance of Maxwell's equations under coordinate transformation, we attempt to construct a set of EM fields in the physical space, different from those in the virtual space, that preserves the form of Maxwell's equations and produces the desired EM behaviour, i.e. a closed cylindrical void space at some location (151). The medium specified by the new set in the physical space is called a medium transformation. That's why this space is called physical space while the other space is called virtual space!

We first need to find the correspondence between the EM field in the physical and virtual space by using the form invariance of Maxwell's equations. This is detailed in ref (151). The resulting equations are listed below:

$$\begin{cases} \vec{E}' = (J^{-1})^t\, \vec{E} \\ \vec{D}' = \det(J^{-1})\, J\, \vec{D} \\ \vec{H}' = (J^{-1})^t\, \vec{H} \\ \vec{B}' = \det(J^{-1})\ J\, \vec{B} \\ \vec{j}' = J \det(J^{-1})\, \vec{j} \\ \rho' = \det(J^{-1})\, \rho \end{cases} \qquad \textit{eq. III-40}$$

In order to keep such invariant forms, the permittivity and permeability tensors must fulfil the following conditions:

$$\begin{cases} \bar{\bar{\varepsilon}}' = \det(J^{-1})\, J\, \bar{\bar{\varepsilon}}\, J^t \\ \bar{\bar{\mu}}' = \det(J^{-1})\, J\, \bar{\bar{\mu}}\, J^t \end{cases} \qquad \textit{eq. III-41}$$

The electromagnetic transformation is possible thanks to the covariance property of the Maxwell's equations. Indeed, the tensors can be decomposed as a linear combination of tensor products (152). In the next paragraph, we develop the toolboxes which allow us to define the conditions for invisible cloaking.

In the formulation of electromagnetic transformation, the relation between the two spaces is often characterised in Cartesian coordinates systems. However in many situations, other orthogonal coordinate systems (such as cylindrical and spherical coordinate systems) are more convenient for practical shape description. The Cartesian formulation of electromagnetic transformation becomes awkward in these situations. Here, we will build a formulation based on a cylindrical coordinate system which is more suited for our study of invisible cloaking.

The physical and virtual spaces are described by two orthogonal coordinate systems. The permittivity tensor in the virtual space orthogonal (cylindrical) coordinate system must be derived from the permittivity tensor in the physical space Cartesian coordinate system by the tensor transformation rule:

$$\tilde{\varepsilon} = \mathrm{T}^{-1}\,\bar{\bar{\varepsilon}}\,\mathrm{T} \qquad \textit{eq. III-42}$$

where T is the Jacobian matrix of the coordinate system change. The permittivity tensor $\tilde{\varepsilon}$ can now be transformed by the medium transformation. For that, $\tilde{\varepsilon}$ is substituted in *eq. III-41* to give the desire tensor ε' providing the conditions for invisible cloaking.

$$\bar{\bar{\varepsilon}}' = \mathrm{T}'^{-1}\,\widetilde{\varepsilon'}\,\mathrm{T}' = \det(\mathrm{M}^{-1})\,\mathrm{M}\,\mathrm{T}^{-1}\,\bar{\bar{\varepsilon}}\,\mathrm{T}\,\mathrm{M}^{\mathrm{t}} \qquad \textit{eq. III-43}$$

In order to avoid any confusion between two kinds of Jacobians, we note here T the Jacobian matrix of coordinate system change (eg Cartesian to cylindrical coordinate system), and M is the matrix of the medium transformation. The matrix M can be decomposed as $\mathrm{M} = \mathrm{T}'^{-1}\mathrm{J}\,\mathrm{T}$ where J is the Jacobian matrix of a transformation between the orthogonal coordinate systems (eg. the conditions for cloaking inside a cylinder) (151). The *eq. III-43* is then simplified to:

$$\bar{\bar{\varepsilon}}' = \det(\mathrm{M}^{-1})\,\mathrm{T}'^{-1}\mathrm{J}\,\mathrm{T}\,\mathrm{T}^{-1}\,\bar{\bar{\varepsilon}}\,\mathrm{T}\,\mathrm{T}^{\mathrm{t}}\,\mathrm{J}^{\mathrm{t}}\,(\mathrm{T}'^{\mathrm{t}})^{-1} \qquad \textit{eq. III-44}$$

The permittivity tensor in an arbitrary orthogonal coordinate system can now be expressed with the help of the metric tensor G (see *eq. III-37*):

$$\bar{\bar{\varepsilon}}' = \det(M^{-1})\, G' J\, \bar{\bar{\varepsilon}}\, J^t\, G^{-1} \qquad \textit{eq. III-45}$$

The covariant permittivity tensor is finally completed to take into account its covariance (more details are given in ref (151)). This provides the final equation of the permittivity tensor:

$$\varepsilon' = \frac{S\, \bar{\bar{\varepsilon}}\, S^t}{\det(S)} \quad \text{where } S = G'^{\frac{1}{2}}\, J\, G^{-\frac{1}{2}} \qquad \textit{eq. III-46}$$

For convenience, the derivation of the permeability tensor $\bar{\bar{\mu}}$ was not developed because it is similar to $\bar{\bar{\varepsilon}}$. This concludes the mathematical formalism needed to open any void area in any medium. The theory is applied hereafter for a cylindrical cloak of invisibility.

Cylindrical invisible cloaking

Let's apply the theory to the current case of invisible cloaking: the cylindrical cloaking. We consider a cylinder with a virtually empty domain in its centre. The invisible zone is constructed by compressing EM field lines initially present in a cylindrical region $r < b$ into a concentric cylindrical shell $a < r' < b$. Fig. 18 illustrates the transformation.

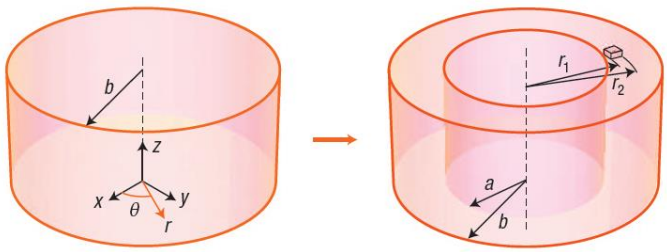


Fig. 18. coordinate transformation from a cylindrical region $r < b$ into a concentric cylindrical shell where $a < r' < b$. The z and θ coordinates are unchanged (92).

Here we consider a generalised coordinate transformation in cylindrical coordinates in which $r' = f(r)$ with $f(a) = 0$ and $f(b) = b$, while θ and z are kept unchanged. The transformation works by using the following equations:

$$\begin{cases} r' = \frac{b-a}{b} r + a \\ \theta' = \theta \\ z' = z \end{cases} \qquad \textit{eq. III-47}$$

where a and b are respectively the radii of the inner and the outer cylinders. For $0 < r < b$ in the transformed space, we obtain the values for $a < r' < b$. The Jacobian matrix of the transformation is

$$J = \begin{pmatrix} \frac{b-a}{b} & 0 & 0 \\ 0 & 1 & 0 \\ 0 & 0 & 1 \end{pmatrix} \qquad \textit{eq. III-48}$$

To proceed further, the Jacobian matrices of the cylindrical coordinate system and the transformation must be found too. Referring to *eq. III-36*, the transformation from Cartesian system to cylindrical system is the matrix:

$$T = \begin{pmatrix} \cos\theta & \sin\theta & 0 \\ -\frac{\sin\theta}{r} & \frac{\cos\theta}{r} & 0 \\ 0 & 0 & 1 \end{pmatrix} \qquad \textit{eq. III-49}$$

The metric tensor G obtained thanks to *eq. III-37* for this transformation is defined as:

$$G^{-1} = T\,T^{t} = \begin{pmatrix} 1 & 0 & 0 \\ 0 & \frac{1}{r^2} & 0 \\ 0 & 0 & 1 \end{pmatrix} \qquad \textit{eq. III-50}$$

$$G = \begin{pmatrix} 1 & 0 & 0 \\ 0 & r^2 & 0 \\ 0 & 0 & 1 \end{pmatrix}$$

The S matrix (introduced with *eq. III-46*) and its determinant is quickly calculated:

$$S = \begin{pmatrix} \frac{b-a}{b} & 0 & 0 \\ 0 & \frac{r'}{r} & 0 \\ 0 & 0 & 1 \end{pmatrix} \text{ and } \det(S) = \frac{b-a}{b}.\frac{r'}{r} \qquad \textit{eq. III-51}$$

The permittivity tensor is then revealed by using the *eq. III-46* and eliminating the radial variable r.

$$\varepsilon'_r = \frac{b}{b-a}.\frac{r}{r'}\begin{pmatrix} \left(\frac{b-a}{b}\right)^2 & 0 & 0 \\ 0 & \left(\frac{r'}{r}\right)^2 & 0 \\ 0 & 0 & 1 \end{pmatrix} \qquad \textit{eq. III-52}$$

$$= \begin{pmatrix} \frac{r'-a}{r'} & 0 & 0 \\ 0 & \frac{r'}{r'-a} & 0 \\ 0 & 0 & \frac{r'-a}{r'}\left(\frac{b}{b-a}\right)^2 \end{pmatrix}$$

This result is available for the permittivity tensor and also for the permeability tensor since the mathematical process is obviously similar. We know now how to modify ε and μ tensors in order to deviate E and H fields as shown in Fig. 19. We consider, for ease of illustration, that the systems are two-dimensional.

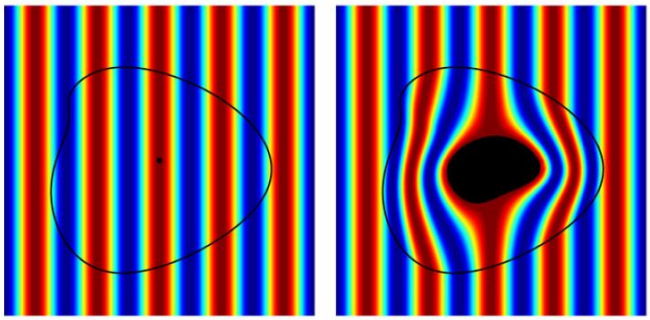


Fig. 19. In the case of a right-propagating plane wave with E_z polarisation, the electric field distribution is drawn before (a) and after (b) transformation (149).

The conditions on $\bar{\bar{\varepsilon}}$ and $\bar{\bar{\mu}}$ tensors for cylindrical cloaking can be simplified. The experimental measurement uses a polarised electric field. Aligning the incoming electrical field along the z axis (cylinder axis) allows benefiting from a substantial simplification. Conditions become:

$$\begin{cases} \mu_r = \left(\frac{r-a}{r}\right)^2 \\ \mu_\theta = 1 \\ \varepsilon_z = \left(\frac{b}{b-a}\right)^2 \end{cases} \qquad \textit{eq. III-53}$$

with the attractive advantage that only μ_r depends on r (89). The cloaking system in this study aims to control permittivity only. Let's now swap the electric and magnetic fields, hence we now work with transverse magnetic (TM) polarisation. In this case only ε_r, ε_θ and μ_z are of interest and must satisfy the requirement of *eq. III-53*. This allows us to completely remove the need for magnetic response of the material (153).

$$\begin{cases} \varepsilon_r = \left(\frac{b}{b-a}\right)^2 \left(\frac{r-a}{r}\right)^2 \\ \varepsilon_\theta = \left(\frac{b}{b-a}\right)^2 \\ \mu_z = 1 \end{cases} \qquad \textit{eq. III-54}$$

The *eq. III-54* suggests the use of a non-magnetic material where ε_r is the unique parameter space-dependent. There is no difficulty to have $\mu_z = 1$. However, It is important to design the thickness of the cloak such that azimuthal permittivity ε_θ tends to a value corresponding to the intrinsic property of the materials in order to most closely match the theoretical conditions.

2.3. Practical approach

The theory shows the way to deflect the waves as desired around a cylinder to render it invisible. The condition $a < r < b$ implied on *eq. III-54* indicates that we must use materials with permittivity and/or permeability lower than 1. No natural or unstructured material offers this

property. Recent research aims to develop structures with these new features. Metamaterials commonly created in this frame are periodic structures based on the interaction between networks of conductive motives. Two examples are presented below.

A line network structure manages the effective permittivity requirement in one, two or three directions of the space. Fig. 20 shows a scheme of continuous metallic wires aligned in 3 dimensions whose radius r and period a are such that r is small compared with a. It has a zero transmission in a frequency band from 0 Hz to the plasma frequency ω_p whose expression involves the geometrical parameters of the network. We can represent the dielectric permittivity of the network by a Drude model of the form:

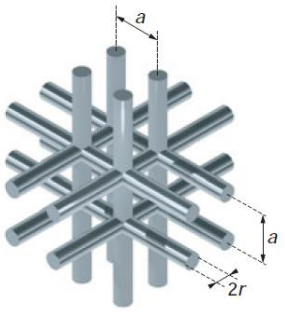


Fig. 20. 3D network of wires whose effective permittivity is negative below plasma pulsation ω_p (155)

$$\varepsilon(\omega) = 1 - \frac{\omega_p^2}{\omega(\omega + i\gamma)} \qquad \textit{eq. III-54}$$

where ω_p is the plasma frequency and γ is the collision pulsation. Actually, ω_p indirectly depends on radius r and space a separating the wires, and γ is intrinsically linked to nature of the conductive rods. Fig. 21 shows the transmission of an array of copper wires (r = 0.25mm, a = 6mm) for a transverse magnetic (TM) incident wave (electric field parallel to the rods). The real part of the permittivity is calculated using expressions of the reference (154). The effective permittivity is negative up to 15 GHz, the frequency corresponding to the plasma frequency. It is therefore a broadband material which behaves like a dilute metal, that is to say where the electron density is lower than in a normal metal.

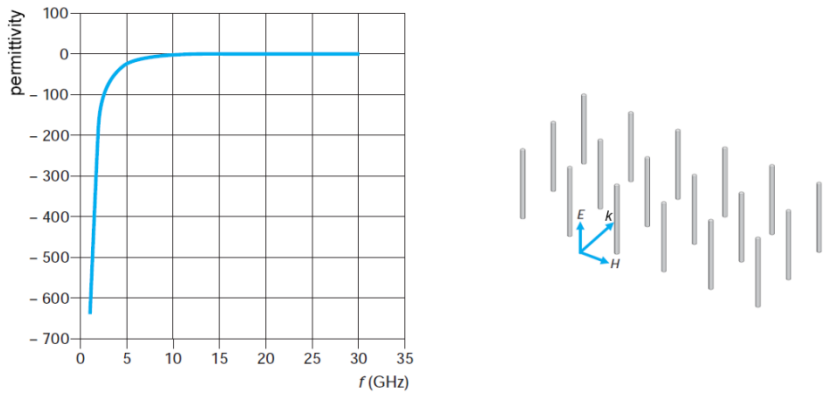


Fig. 21. real part of effective permittivity of the array of copper wires ($r = 0.25mm$, $a = 6mm$) (155)

A complementary network controls the permeability of the material. The network is formed of split ring resonator (SRR) having a permeability lower than 1 in a frequency band which is a function of the geometrical parameters. The expression of this permeability is (156):

$$\mu(\omega) = 1 - \frac{\frac{\pi r^2}{a^2}}{1 + \frac{2l\sigma}{\omega r \mu_o} i - \frac{3lc_o^2}{\pi \omega^2 r^3 \ln\frac{2d}{g}}} \qquad \textit{eq. III-54}$$

where c_o is the speed of light in vacuum, a is the distance between SRR in the plane, l is the distance between the successive plane of SRR, σ is the conductivity of SRR and g, r, p and d are geometric parameters defined by Fig. 22 and i is the imaginary number.

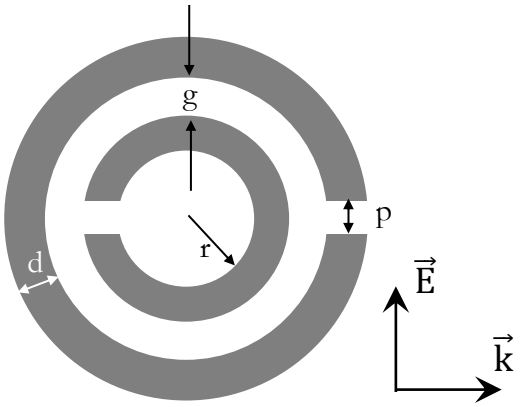


Fig. 22. example of a single slit ring resonator (SRR)

Fig. 23 shows the behaviour of the effective permeability of the SRR network. The permeability is only positive below ω_o and beyond ω_p. For other application, it is interesting to note that permeability is negative between those two particular frequencies. For the present research, we focus on values just beyond ω_o, where μ_{eff} is located between 0 and 1. The SRR network has to be very carefully designed because the resulting permeability is highly sensitive to geometry.

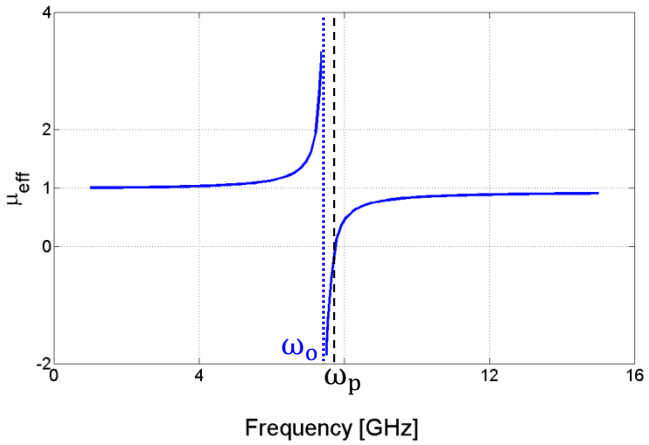


Fig. 23. effective permittivity of a SRR network with $\sigma = 5.10^3 S/m$, $r = g = p = 3mm$, $d = 2mm$, $a = 20mm$ and $l = 0.2mm$

The patterns described above are obviously made of a conductive substance on an insulating substrate. In practice, it is a metal such as copper or gold evaporated on printed circuit board substrate widely used in electronics (89). This method enables highly accurate patterns and thus, excellent control of the EM propagation. The negative refractive index materials follow the same fabrication strategy (155). Pendry et. al. have also achieved a cylindrical cloaking system operating at 8.5GHz (89). A network of SRR defines the radial permeability as necessary (see Fig. 24). Any object in the centre of the structure is indeed invisible to this radar frequency. The narrow frequency band is a major drawback. The scientific literature has not presented an approach capable of widening the frequency band yet. Fragility and production cost of SRR or network lines on PCB limit this approach to small scales and specific applications. That is why, we propose to develop a cloak entirely based on polymers and carbon nanotubes to ensure good mechanical strength and allow large scale applications. The implementation strategy must be adapted to the possibilities offered by composites. The new concept and the design are explained in detail in the next paragraph.

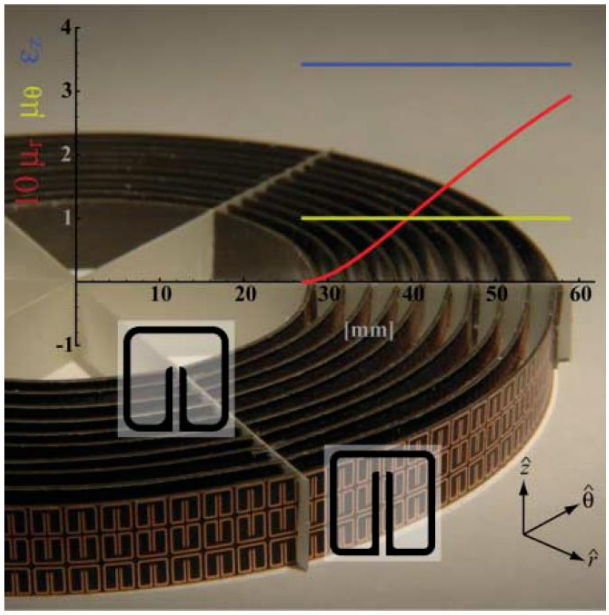


Fig. 24. microwave cloaking structure with a plot of the material parameters that are implemented. The SRR of inner cylinder and outer cylinder are shown in expanded schematic form (transparent square insets). (89)

2.4. Implementation of ε-only controlled multilayer invisibility cloak

The *eq. III-54* opens the possibility of invisibility by controlling radial permittivity $\varepsilon_r(r)$ as function of the radius. The thickness of the cloak (b-a) has to be designed in order to get as close as possible to the azimuthal permittivity ε_θ defined by the second equation (see *eq. III-54)*. The z-permeability μ_z is of course 1. The strategy developed in this work is the production of a series of bilayers made by superimposing a dielectric polycarbonate and a conductive composite film. A correct control of the polymer thickness and composite conductivity leads to a decrease of permittivity below 1 (and even negative values) at a few GHz. On the example in Fig. 25, the effective permittivity at 6GHz of a bilayer is shown as function of polycarbonate thickness. The composite is 400µm thick and $\sigma = 100S/m$. We select 6GHz as reference frequency for the study of the cloaking for particle reasons detailed in section IV-3.3. The effective permittivity becomes positive when the thickness of the dielectric layer goes beyond 6.851mm and exceeds 1 beyond 8.366mm.

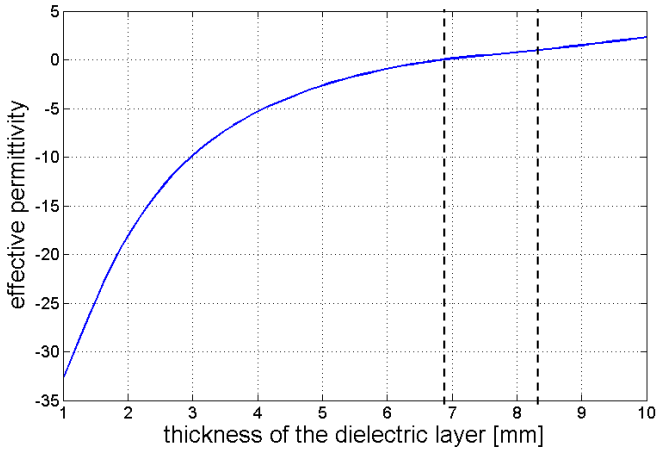


Fig. 25. simulation of variation of permittivity of a polycarbonate-composite bilayer. The PC layer has $\varepsilon_r = 2.8$ and the composite is 400µm thick and $\sigma = 100S/m$.

A cloaking multilayer designed for 6GHz needs successive bilayers from $\varepsilon_r(a) = 0$ up to $\varepsilon_r(b) = 1$. It is feasible by an adjustment of the polymer thickness in order to shift ε_r (for a fixed frequency). The

effective value of ε_θ of a bilayer is very close to the one of dielectric layer because the polymer/composite thickness ratio is high enough to neglect influence of the composite.

We have made the choice to control radial permittivity which is required for cylindrical shape cloaking. Each bilayer has hence to be bent into concentric tubes (see Fig. 26). Afterwards, the bilayers are stacked in order to produce the increasing permittivity from inner radius to outer radius. This method has the advantage to allow independent characterisation of each bilayer to validate the effective permittivity.

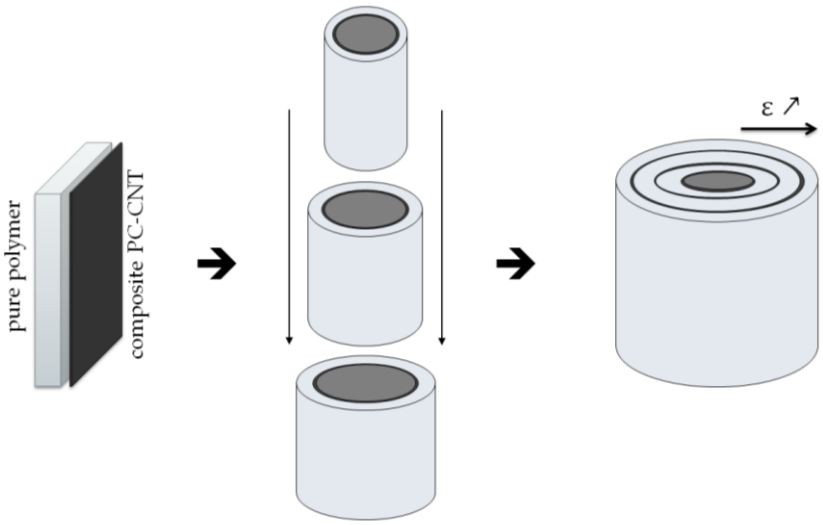


Fig. 26. The bilayers (on left) have an effective permittivity defined by their geometry. Each bilayer is shaped to tube and stacked to form successive concentric layers where ε_r increases from inner to outer radius.

Chapter IV

Materials and methods

This section aims to sum up the reference stuffs and methods used for chemical, physical and electromagnetic characterisations and microscopic observations. We take a bottom-up description in the sense that the production of nanofillers is explained (when they are produced at UCL) and then the process of implementation is discussed. The latter describes the elaboration of conductive or ferromagnetic composite films and the more complex structure of oriented nanocharges in the polymer. The electric and electromagnetic characterisation methods are also given for single film, multilayer structures and the complete invisible cloaking device.

1. Nanocharges for composites

The carbon nanotubes and solutions based on CNT have been ordered from outer company. Their grade and origin are given in this section. The nanowires were produced at UCL by a process described in the second section.

1.1. Origin of nanocharges

The used carbon nanotubes are multi-walled NC 7000 provided by the company NanoCyl. These carbon nanotubes have high aspect ratio (>150) which enables them to form a conductive network at a very low concentration. The NC 7000 series is produced by a Catalytic Chemical Vapor Deposition (CCVD) process. The characterisation of this product is listed in Table 1.

Table 1. characterisation of NanoCyl™ NC 7000 carbon nanotubes[3]

Property	Value	Method
average diameter	9.5 nm	TEM
average length	1.5 μm	TEM
carbon purity	90%	TGA
metal oxide	10%	TGA
amorphous carbon	/	HRTEM
surface area	250-300 m^2/g	BET

[3] data sheet of NanoCyl™ NC 7000 thin multi-wall carbon nanotubes

NanoCyl also produces a water based suspension of CNT called AquaCyl™. The carbon nanotubes with the highest compatibility with water are selected for this product; furthermore AquaCyl™ composition has an ionic surfactant for superior dispersion and stability. The information about the used grade is in Table 2.

Table 2. general information about AQ0101 AquaCyl™ series[4]

Property	AQ0101
carbon concentration	1%
surfactant concentration	1%
deionised water	98%
pH	7-11
boiling point	100°C
melting point	0°C

1.2. Production of metallic nanowires

CNT are now mass producible and they have many advantages as conductive nanofillers. Nevertheless, it is interesting to compare the properties of CNT nanocomposites to those based on another type of nanofillers. Metallic nanowires (NW) have a very high intrinsic conductivity and their possible magnetic nature can bring new opportunities impossible to achieve with CNT. Gold nanowires (Au-NW) as well as nickel nanowires (Ni-NW) have been produced and embedded into composites. All the nanowires have been synthesised in the BSMA laboratory by an electrodeposition process. The process involves the reduction of metal ions from an electrolyte solution in the pores of a nanoporous alumina template in order to form an array of nanowires. This process produces metallic nanowires of the wanted element or alloy with a well-defined aspect ratio.

Electrolytic solution

The electrolytic solution to synthesise gold nanowires (Au-NW) is the commercial solution Goldbath SF (15.0 g/l) from Metakem GmbH. Its stability is limited to only a few months if stored in a cool and dark

[4] data sheet of AquaCyl™ Carbon Nanotubes Aqueous Dispersions

place. When these conditions are not met, the ions precipitate, making the solution unusable. The electrolytic solution of nickel has better stability. We use nickel sulphate dissolved in an acidic medium composed of 0.6 M boric acid (H_3BO_3) and 0.5 M nickel sulphate hexahydric ($NiSO_4.6H_2O$) mixed at room temperature.

Electrodeposition into alumina template

The nanowires are formed in the pores of a UniKera Standard alumina membrane (Al_2O_3) from Synkera (see Fig. 27). The selected template provides a very homogeneous distribution of pores. The pore areal density is up to 35% which is enough for small scale production. The diameter of the pores is 150nm and the membrane is 100µm thick. Hence, the length/diameter ratio of the nanowires is about 667 (assuming a perfect filling of the pores).

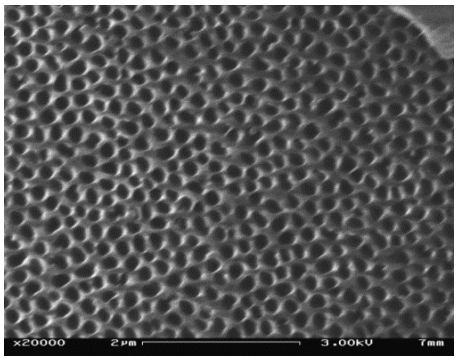


Fig. 27. SEM image of the surface of UniKera Standard template (from Synkera)

Growth starts from the cathode which is deposited on the membrane. First, a chromium layer of 20nm is evaporated by e-beam (Pfeiffer Vacuum Classic 500 supplied by Intellemetrics IL150) on one side of the membrane to make a strong interface between the alumina and the actual cathode. Next, 1000nm of copper are evaporated as the actual cathode on the Cr adhesion layer. Of course, the opposite side of the template is free to let the electrolytic solution flow into the pores. The membrane is placed in an electrochemical cell with a suitable electrolytic solution as illustrated in Fig. 28. A potentiostat (model 263A from EG&G Princeton Applied Research) brings electrons to the cathode which reduce the ions in order to form the array of nanowires. The potentiostat also measures the quantity of reduced ions. In this way, we are able to precisely calculate the mass of nanowires inside membrane.

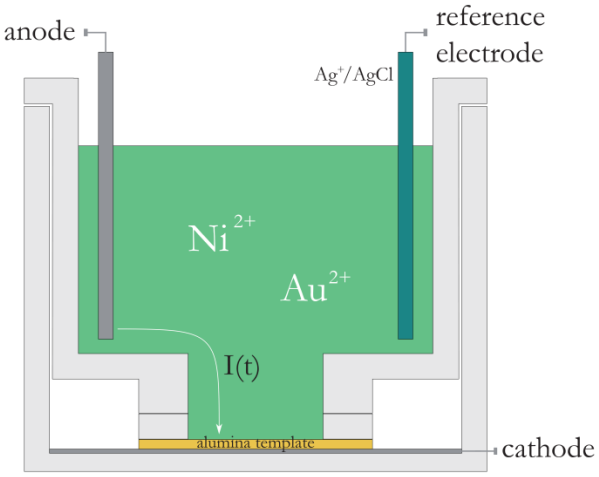


Fig. 28. Scheme of an electrochemical cell. The voltage between the anode and the cathode forces ions to be reduced inside the pores of alumina template.

The electrodeposited metal gives precise information on the amount of reduced ions in the pores. Suppose a chemical species X reduced by electrochemical reaction, the balance for this reaction is

$$X^{\pm n} \pm ne^{-} \rightarrow X \qquad \textit{eq. IV-1}$$

The threshold voltage of the reaction depends on the ion to be reduced. The electroreduction of gold requires pulsed voltage to improve the growth homogeneity of the nanowires. The profile follows the experimental rule:

- $U_1 = -0.55V$ for 12ms
- $U_2 = -0.35V$ for 88ms

Nickel is homogeneously reduced at constant optimal voltage determined by experience to be 1.1V. The potentiostat maintains the potential between the electrodes while measuring the intensity of the current flowing in the solution. This current $I(t)$ passes through the electrochemical cell during a time t, and the electrical load involved is given by the Faraday law

$$Q = \int_0^t I(t)dt \qquad \textit{eq. IV-2}$$

The electric charge Q corresponds to the consumption (reduction) or production (oxidation) of Q/F moles of electrons. Considering the stoichiometry of the reaction, Q also corresponds to the consumption n_x moles of species X such that

$$n_X = \frac{Q}{nF} \qquad \textit{eq. IV-3}$$

where F is the Faraday constant, or 96485C/mol. The amount of reduced material is equivalent to the weight of produced nanowires.

Collecting nanowires from the alumina template

The aim of the electrodeposition process is to obtain a large amount of nanowires. Once synthesised, the nanowires have to be extracted from their membrane. First, the cathode is completely etched away. Copper is etched by 0.5M $FeCl_3$ acid in 3-4 minutes. Afterwards, chromium is etched in 2-3 minutes by a caustic solution of 0.33M $KMnO_4$ and 5M NaOH. Preliminary experiments have proven that a residue of the cathode maintains nanowires attached together. It could be required to extend the exposure time to acids for ensuring the complete etching of cathode. At this stage, the nanowires are still strongly embedded in the template. The set is dived in 8M caustic soda heated at 70°C for 24 hours. During the last minutes, ultra-sonication is applied to ensure a good separation of the residual cluster of NW. The suspension of nanowires in suspension is filtered with the help of a polycarbonate ipPORE™ Track Etched Membrane from it4ip. This is a 25µm thick porous film with a pore density of $5.10^8 cm^{-2}$ and a pore diameter of 200nm. The pure NW are so collected on the filter. Acetic acid at 50% is next passed through the filter in order to neutralise potential adsorption/residue of caustic soda on the surface of the NW. Next the NW, still on the membrane, are rinsed with pure water and finally dried in an oven for 24 hours at 120°C. The processes of embedding NW in polymer is explained in the next section.

2. Processing of nanocomposites

The nature and origin of nanofillers require specific mixing processes. Pure CNT are not dispersed in the same way as AquaCyl™ CNT. The metallic nanowires are quite tricky and require complex methods which have been developed in this thesis to disperse them in the polymer matrix. The implementation methods for each type of nanofillers are described in this section.

2.1. Compounded polymer-carbonaceous nanofillers composites

Blending by extrusion

CNT – polycarbonate conductive nanocomposites are the basis for the wideband absorbers and electromagnetic bandgap filters developed in this thesis. They are usually stacked with other polymer films to induce the desired behaviour of the EM waves. For wideband absorbers, the composite layers are alternated with pure Lexan™ polycarbonate sheets (from the company Sabic). For EBG filters, the dielectric substrate is made of Arlon AD1000 from the company Arlon Microwave Materials. It is based on a PTFE-ceramic powder composite with woven glass, has a permittivity of 10.7 and 1.5 mm thickness. The polymer matrix used for conducting nanocomposites is Bayer Makrolon® OD2015 polycarbonate. The CNT are multi-walled NC 7000 nanotubes provided by the company NanoCyl. The nanocomposite compounds are melt-blended at 280°C for 5 minutes at 150 RPM in a micro 15 DSM micro-compounder. The mixing temperature is 280°C, 130°C above the

glass transition of PC, in order to ensure sufficient fluidity for optimum dispersion of the CNT. The composite pellets are twice hot pressed under 10 T at 250°C for 30 seconds in a Fontijne press to produce films of approximate 175μm thickness. The first pressing is done to shape a first film (400μm thick) from pellets. Some irregularities on the surface remain where the pellets were present in the mould. After cooling, a second pressing gives the final thickness (175μm) and flattens the surface.

Orientation of CNT by stretching

Oriented CNT films are produced from a custom-made (Makrolon® 2805 polycarbonate reinforced with 2% of CNT NC7000) compound provided by NanoCyl. A preliminary experiment has shown that stretching of 2% CNT films works properly. A test with a 5% CNT composite has quickly concluded that the viscosity becomes too high. The material breaks during stretching. This fact limits the CNT concentration in oriented films to about 2%. Lower concentrations have not been tried since they bring the risk of not reaching the percolation threshold. Indeed, we aim to form trains of connected CNT aligned in the stretch direction.

Compounded pellets are continuously injected into the micro 15 DSM extruder at 150 RPM while material also continuously comes out through a film shape die. The hot film is directly connected to a stretching roll (DSM Xplore roller). The outgoing ribbon is driven by a take-up reel which stretches the composite. The rolling speed and torque are imposed at respectively 700mm/min and 30Nmm when the extrusion temperature is 280°C. If the temperature is raised to 300°C the rolling speed and torque can be increased up to 1000mm/min and 45Nmm. The enhancement of the stretching makes the films thinner so that the thickness after stretching is about 40x smaller than at the die. The mechanical stress aligns CNT in the strain direction. The process should also work for wireframes but it has no relevance to the application of this thesis.

2.2. CNT ink based composites

Compounding of polymer-CNT nanocomposites is probably the most usual process for making conductive films. Another method has been developed in the frame of this thesis, still based on polycarbonate and CNT. NanoCyl produces a water based suspension of CNT called AquaCyl™. Its composition is 98% of pure water, 1% of multi-walled CNT and 1% of surfactant. AquaCyl™ is applicable as a coating on large surfaces of polycarbonate films just like a conventional ink. In this way, we obtain an alternative for forming a dielectric-conductor layer stacking. The dielectric is still Lexan™ polycarbonate but the conductive layer now becomes an ultra-thin coating of entangled carbon nanotubes. After drying of AquaCyl™ ink, there is a solid CNT deposit on the PC sheet. Actually, the polycarbonate is hydrophobic; its contact angle must be modified to allow the adhesion of a significant amount of CNT. A surface treatment of the PC sheets has hence been performed to increase wettability (10). All the practical details of the plasma treatment are given in Annex A. After the plasma treatment, adhesion of the CNT is satisfactory and it is possible to cover uniformly a large polymer area. The amount of deposited CNT controls the resulting level of conductivity. AquaCyl™ is deposited by dip coating or airbrushing on the polymer. This leaves entangled CNT whose thickness varies from 1.5 to 7µm. Fig. 29 shows an image of an AquaCyl™ deposit sandwiched between two thin sheets of PC.

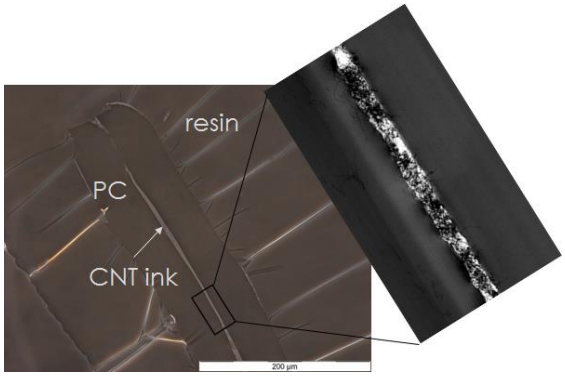


Fig. 29. CNT ink airbrushed on prepared polycarbonate sheet and trapped by a second PC sheets. The optical microscope image is zoomed 20x and the TEM one is zoomed 5000x.

A series of dip coatings was performed with different dilutions of AquaCyl™. The amount of CNT attached to the polycarbonate surface

is inversely proportional to the dilution with a resulting control on conductivity. However, the simulations of absorbers and EBG filters sometimes demand a higher level of conductivity which is not reachable by dip coating. A second method, airbrushing, was hence developed to extend the range of conductivities. Pure AquaCyl™ is coated by a Paasche VL-3W airbrush on treated polycarbonate surface. The solution is airbrushed several times to increase the conductivity. A drying time of one hour at room temperature is allowed between each projection. The electrical characterisation (detailed in section V-1.1) shows that the two complementary processes (dipping and airbrushing) cover all required conductivity levels.

2.3. Structured patterns in CNT

The latter method developed from carbon nanotubes adds complexity to the structure. We "draw" now periodic patterns via AquaCyl™ on PC. Initially, the polycarbonate sheet is activated by plasma as explained in section IV-2.2. The CNT ink is then airbrushed through a mask beforehand designed. The mask is machined from a nickel foil (from Kurt J. Lesker company) of thickness 100µm. This thickness is the best compromise between flexibility and strength. The foil must be flexible enough to perfectly fit the light surface irregularities the PC sheet but it must be handled without tearing. The patterns are burned by Oxford laser (picosecond laser-etching system model Oxford J-1064/355, Oxon, UK) used with a wavelength of 355nm. It is clear that any pattern can be burned. Among the tested units, we focus here on a network of parallel lines (explanations in V-3). The line length is 65mm which is substantially larger than the size of the used wave guides. Structured films may be characterised on the whole spectrum. Line width was imposed 0.5mm. This choice is empirical; it is the thinnest width allowing correct AquaCyl™ flow through those slots. Having narrowest lines has a relevance to the application explained in section V-3. The distance between lines varies in the different masks. For convenience, we give a label to all structures (see Table 3).

Table 3. geometric characteristic of the network of CNT striplines

label	narrow	medium	large	wide
gap between lines	1.5 mm	2.5 mm	3.5 mm	4.5 mm

The mask is placed on the PC sheet and a magnetic plate (Nd-Fe-B protected by a coating of epoxy resin produced by SuperMagnete). With the magnetic character of Nickel, the mask puts pressure on PC and greatly reduces the infiltration of AquaCyl™ between the mask and polycarbonate. Indeed, the PC surface has become relatively hydrophilic (due to plasma treatment) and ink has tendency to spread beyond the patterns by capillary suction. The mask is also coated with hydrophobic lubricating agent to reduce this phenomenon. AquaCyl™ thus remains confined in the slots of the mask and faithfully reproduces the pattern.

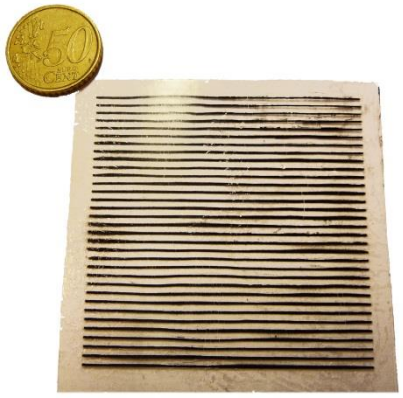


Fig. 30. picture of "narrow" CNT striplines sandwiched between PC sheets

2.4. Metallic nanowires composites

Implementation by solvent

Dispersion of metal nanowires in polycarbonate from a solution has proved to be effective. It is difficult to homogeneously disperse nanowires in a polymer because of Hamaker forces tend to segregate them and their density induces decanting. The *eq. III-27* shows that it is favourable to select a solvent with a dielectric constant close to that of nanowires to minimise the tendency to agglomeration. It is not possible to give a precise value for the dielectric constant of the nanowires because it depends on the shape (157) and size of particles (158) and the measurement direction. Anyway, the estimated value is high, which requires a high-ε solvent. Among polycarbonate compatible solvents, dichloromethane (DCM), dimethylformamide (DMF) or dimethyl sulfoxide (DMSO), have a permittivity of respectively 8.93, 36.7 and

46.7[5]. Experimental tests show that DMSO which gives the best dispersion, possibly as a combined result of the Hamaker forces and the high density of this solvent, which somehat reduces the tendency to decantation. We will use only DMSO for further experiments.

Gold or nickel nanowires are filtered through a nanoporous polycarbonate membrane (see section IV-1.2). The filter containing nanowires is directly dissolved in 50 ml of DMSO at 150°C. Depending on the amount of reduced ions during electrodeposition, we can calculate the mass of the nanowires. For example, the reduction of 20 C of Au^{2+} corresponds to $n_{Au} = \frac{20}{2.96485} = 1.04\,10^{-4}$ moles (*eq. IV-3*) or 20.4 mg of gold. Usually, we add 1 to 1.5 g of Makrolon® OD2015 polycarbonate in order to obtain 1% by weight of nanowires in PC. The solution/suspension is next heated up to 300°C to evaporate all the solvent. An alternative to evaporation could be the mixing of the solution with a non-solvent such as water. A preliminary experiment using this method has shown the presence of small agglomerates and this route has not been pursued further but it could be improved in future research. During solvent evaporation, an Omni-Ruptor 400 Ultrasonic Homogenizer applies sonication at medium power to maintain a good suspension while density and viscosity increase. A long process at high temperature and under ultra-sonication (plus possible residues of NaOH) could degrade PC. Annex B discusses this possibility with the help of a GPC analysis and concludes that the damage is limited. After complete evaporation of DMSO, the nanocomposite is placed in an oven at 120°C for at least 24h to eliminate all residue of solvent. The final step is a hot pressing at 250°C under 10T for 30s to shape a composite film.

Ultra-thin nanowires film by filtering

A complementary method of producing a "composite" of nanowires and PC is based on the deposition of ultra-thin layers of entangled metallic nanowires. The nanowires already form a thin mesh on the filter. To facilitate handling, the filter is directly sandwiched between two 55µm thick Lexan™ polycarbonate films. The sandwich is hot pressed at 210°C, 10T for 30s. The process has the advantage of simplicity and yields a confined thin conductive and magnetic film. Fig. 31 sums up the

[5] source: http://depts.washington.edu/eooptic/linkfiles/dielectric_chart[1].pdf

steps from the NW inside the alumina template up to the hot pressing of filter covered by NW.

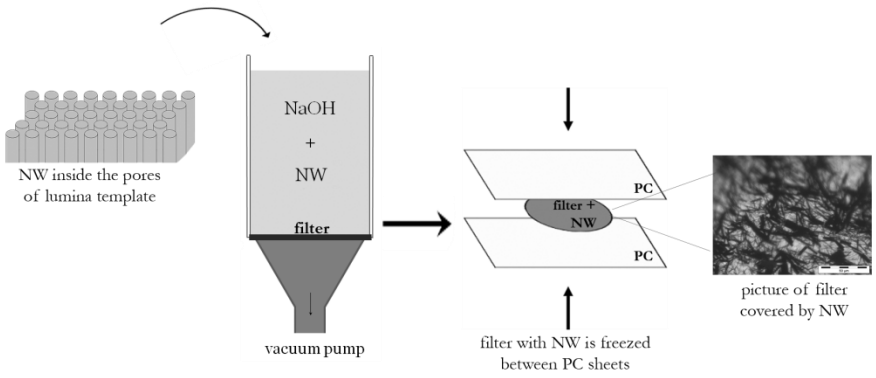


Fig. 31. Main steps for the implementation of ultra-thin NW film between PC sheets

2.5. Machining of dielectric spacers for cloak of invisibility

The invisible cloaking is based on polymer-composite bilayer. The composite production is detailed in IV-2.2. It is AquaCyl™ sandwiches rolled in tubes to conform to the cylindrical multilayer. The dielectric spacer is designed as a function of its intrinsic permittivity. Indeed, the thickness of the tube is the critical point to finely control the effective permittivity of the bilayer (explanations are given in III-2.4). The selection of the spacer is then made according to its ability of shaping. A quick, easy and very fashion solution is to print directly tubes with a 3D printer! We printed concentric tubes with a Fortus 250mc (Stratasys) in acrylonitrile butadiene styrene (ABS*plus*-P430). The advantage of this technique is the printing accuracy of 178µm. Unfortunately, the dielectric constant of ABS is not precisely defined in the data sheets, it is in between 2.3 and 2.85 [6]. Actually, the printing mesh has an impact on the effective permittivity. Furthermore, the structure is porous which has a dramatic consequence for EM response since permittivity varies slightly with humidity of the air (housed in the pores). All samples were printed with the maximum density in order to limit the air inside the structure.

[6] see data sheet: http://www.stratasys.com/~/media/Main/Secure/Material Specs MS/Fortus-Material-Specs/Fortus-MS-ABSplus-01-13-web.pdf

The required properties such as permittivity have been precisely measured by wave guide method (see section V-5.1).

Rohacell® HF71 (from Evonik Industries) is used as second alternative as spacer. This polyacrylate foam is commonly utilised in RF free space applications for its extremely low dielectric constants close to unity with associated loss tangent factor less than 0.001, making it particularly favourable to emulate signal transmission through air in the microwave region. It has the strong advantage of a stable permittivity in frequency fixed at 1.106. All cells of the material are fully-closed so that the exposed cut cells at the surface prevent all gas or liquid from infiltrating further into the foam. Rohacell® can be processed by common machining methods without modifying intrinsic properties. The tubular shapes required for our cloaking applications were realised by water cutting with abrasive particles processed by Grando. The accuracy is satisfactory for our application.

The design of cloaking is adapted for the two types of spacers. The 3D printer has the advantage of high accuracy while Rohacell® has a well-defined dielectric constant. These devices are compared and discussed in section V-5.3. A photo of the machined Rohacell® and printed ABS tubes is shown in Fig. 32.

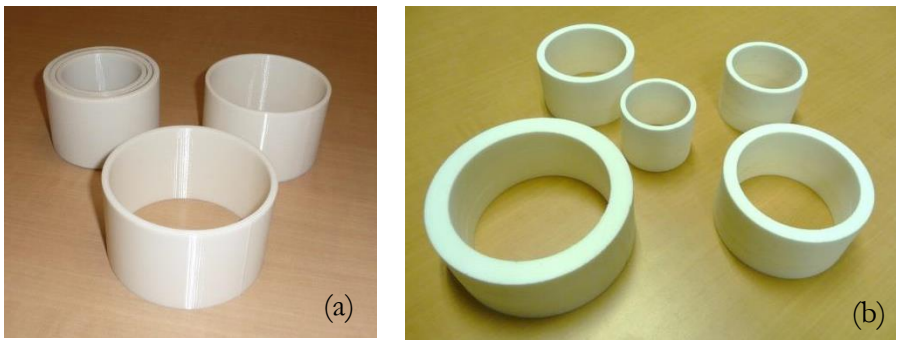


Fig. 32. photo of ABS in (a) and Rohacell® tubes in (b) designed for invisible cloaking

3. Electrical characterisation

3.1. DC characterisation

The measurement of in-plane DC conductivity σ is performed by 4-point probes method which is performed by Keithley K2400 or K6430 equipped with a SP4 Four Point Probe Head (Lucas Labs). It is an electrical impedance measuring technique that uses aligned separate pairs of current-carrying and voltage-sensing electrodes to make more accurate measurements. The current is supplied by a current generator between the points 1 and 4, while the voltage is measured between points 2 and 3 as shown in Fig. 33. The ratio of voltage measured on the current flowing through the sample gives the resistance of the section between the points 2 and 3. We assume that the electron propagation depth is smaller than the gap between probes which is totally satisfactory since the thickness itself of the samples is often thinner than this gap. For equidistant probe, the in-plane conductivity as given by:

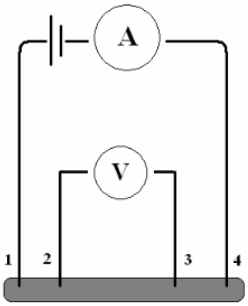


Fig. 33. scheme of 4-point probe method

$$\sigma_{DC} = \frac{\ln(2)}{\pi}\frac{I}{U} \qquad \textit{eq. IV-4}$$

The out-of-plane DC conductivity (along the thickness of the film) is measured using an LCR-meter (NovoControl αlpha-A High Performance Frequency Analyzer). In this method, the film acts as the insulating material between two planar metallic electrodes forming an equivalent resistance-capacitor couple. The meter measures the voltage across and the current through the sample and, the phase angle between the voltage and current to calculate impedance, yielding finally the capacitance and resistance of the sample.

3.2. AC/microwave characterisation

The frequency response of the samples is characterised using a PNAX-70 (Agilent) Vector Network Analyzer operating up to 70 GHz (or VNA Wiltron 360 up to 40GHz). Physical properties (as dielectric constant, permeability and conductivity) in the direction perpendicular to the film are extracted from measurements using a microstrip Anritsu 3680v Test Fixture plugged on PNAX-70. We use the line–line (LL) method for measuring all DUT which is based on the well-known line–return–line (LRL) calibration technique developed for microwave circuits (159).

The in-plane corresponding parameters are obtained from a configuration close to waveguide method. The techniques are explained and illustrated in ref (160). Unlike microstrip characterisation, the wave guide method induces spurious ripple observed on measured S-parameters. It is caused by a variable impedance matching of the DUT with the frequencies (161). The impedance matching maximises transmission while minimising reflections. As explained in (160) however, the coax-to-waveguide to transitions used for the waveguide method are not necessarily very directive antennas. The emitted field has therefore the shape of a cone of unknown dispersion, and part of it might not reach the opposite transition or might also be reflected by the flanges that embed the device. Even a proper calibration procedure does not totally suppress these residual reflections.

3.3. Set up for wave propagation mapping

The invisibility cloaking performances are characterised through free space propagation of waves. The incident EM wave is generated by the PNAX-70 (Agilent) Vector Network Analyzer. Port 1 is connected to wave guides adapted to the frequency ranges 3.95-5.85 GHz or 5.85-8.2 GHz. A homemade probe is connected to port 2 for measuring the electric field in free space. The probe design is in accordance to ref (162). A separate Comsol simulation has shown a high frequency stability of the probe. The antenna is fixed in front of an XY table at a sufficient distance to have quasi planar wave front entering the mapped plane. The probe is attached to two ILS Series arms (High-Performance Mid-Range Travel Linear Stages) from Newport which are controlled in x and y-direction with the help of an ESP300 1–3 Axis Motion Controller/Driver. A photo of the assembly in shown in Fig. 34 and a photo of our probe is in inset. The table is covered by absorbing foam surmounted with Rohacell® from Evonik to avoid parasitic reflection. A script made in LabView creates the interaction between the PNAX-70 and the XY table. For each position, the PNAX-70 measures S-parameters after 0.2s of delay to ensure the stabilisation of the probe. The plane is so scanned by steps of 1mm (or 500μm). The 2D spatial map of the electric field is afterwards generated by Matlab.

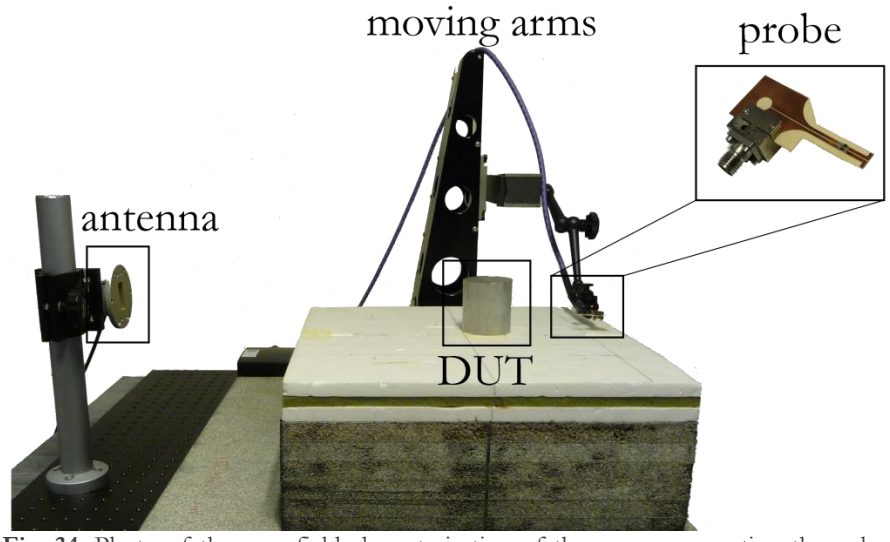


Fig. 34. Photo of the near field characterisation of the wave propagation throughout the XY table. The inset shows the homemade probe.

Chapter V

Experimental results and discussion

The current chapter focuses on the experimental electromagnetic characterisation, modelling and discussion of the set of all the structures presented in the previous chapter. The analysed multilayers are listed in Annex C for convenience.

In the first section, we study broadband absorbers based on extruded CNT composite films and CNT ink on polymer films. In Section 2, we introduce a novel multilayer structure based on nickel nanowires opening a route towards ultrathin high efficiency absorbers. In both cases, each individual film is measured independently in order to determine the percolation threshold and physical properties (i.e. complex permittivity and permeability), which are used as crucial inputs for our model of hierarchical stacking optimisation. The experimental characterisation of the polymer-composites multilayers is performed by wave guide measurements. The results are analysed by making a comparison with the theoretical Rozanov limit and quantified by the figure of merit drawn for this thesis.

In the third section, we use CNT orientation in a polymer nanocomposite and anisotropic "macro" structuration of CNT conductive paths to produce microwave absorbers sensitive to wave polarisation. When the anisotropic composites are stacked, the multilayer either absorbs preferably one angle of polarised wave or forces the electric field of the wave to rotate a certain angle.

In section 4, we study electromagnetic bandgap (EBG) filters based on CNT and polymeric or ceramic substrates. The geometry and nature of the dielectric layers open up either high absorption or reflection peaks in the spectrum. The filters can be tuned from low frequency (~1GHz) up to very high frequency (70GHz).

The last section focuses on cylindrical invisible cloaking. The control of wave propagation no longer aims at absorption but rather deviation of microwaves. The building blocks of the cloaking structures are made of PC-CNT composites and bulk ABS or Rohacell® foam. The physical properties of each building block and their controlled stacking are analysed. The experimental near field behaviour is mapped over an XY table to observe to propagation of the EM wave around the cloaking structure. The effect is quantified and some theoretical avenues are discussed for future improvements.

1. Broadband absorber based on CNT

The broadband absorbers considered in this section are made of stacks of films with a conductivity increasing successively from layer to layer. The individual elements of the stacks are either made of CNT - PC composites or PC films coated with a CNT-based ink. They are individually characterised in order to know their physical properties precisely. The set of films is then stacked, thereby creating a thin absorber multilayer studied from 6 to 67GHz. The efficiency is gauged by comparison with the ultimate limit of thickness defined by Rozanov.

1.1. Electrical and morphological characterisation

Compounded PC-CNT composites

The melt-blending process yields films whose conductivity is determined by the CNT concentration. Experiments have shown that the required conductivity range can be achieved with CNT concentrations not exceeding 5%. By extrusion, we achieve excellent dispersion of the CNT, leading to adequate electrical percolation. TEM images in Fig. 35 show different load concentrations in the PC matrix. Very homogeneous dispersion is achieved at low CNT concentration (e.g. 1%), while some heterogeneities start showing up at high concentrations (e.g. 7.5%). The latter are well above percolation threshold and the heterogeneity does not significantly affect the electrical performance.

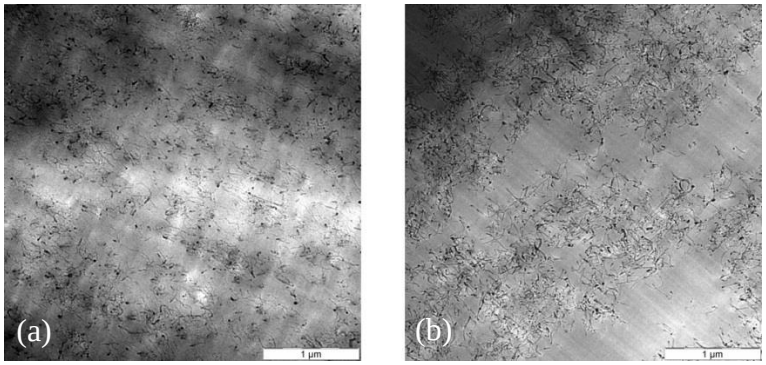


Fig. 35. TEM images of PC-CNT melt-blended composites. The composite in (a) has 1% CNT; the composite in (b) has 7.5% CNT.

The carbon nanotubes are mainly oriented by the squeeze flow generated by compression moulding in the plane of the film, so that a high anisotropy of electrical properties is expected, requiring a careful combination of different DC and frequency-dependent electrical characterisation techniques. The in-plane DC conductivity is measured by 4-contact probe while an LCR-meter provides the out-of-plane DC conductivity. As expected, the anisotropy of the CNT in the film induces much higher values for in-plane conductivity than for out-of-plane, as shown in Fig. 36. It is not obvious to fit the data of DC conductivity with a rigorous model (144). Power laws are however reported in the literature to yield reliable fits to experimental data together with an estimate of percolation threshold. In this thesis, we use the empirical formulation (detailed in section III-1.7): $\sigma_{DC} = k(\phi - \phi_c)^{\mu}$ where k and μ are free constants, ϕ is the weight ratio of reinforcement and ϕ_c is percolation threshold (141). The free constants are fitted by the nonlinear least squares method computed by the *Trust-Region* algorithm provided by Matlab. For the in-plane configuration, ϕ_c is found equal to 0.024 ($k = 527.4$ and $\mu = 1.01$), which means that in-plane percolation already starts at 2.4%. The conductivity is 3 orders of magnitude lower in the perpendicular direction. The conductivity measured along the thickness of the film is almost constant instead of following the behaviour given by the empirical power law. This means that percolation is probably never reached even for the highest concentrations considered in this work, due to the in-plane orientation of the CNT induced by squeezing.

High frequency conductivity follows different physical mechanisms than its DC counterparts. However, a similar power law with suitable free parameters gives a convincing fit: $\sigma_{AC} = k(\phi - \phi_c)^{\mu}$. Samples are characterised using different methods for the in-plane and out-of-plane configurations: dielectric constant and conductivity in the direction perpendicular to the film are extracted from microstrip measurements from 10MHz to 67GHz, while the in-plane corresponding parameters are obtained from a waveguide configuration. The plotted conductivity is the average value along the spectrum from 8 to 67GHz. AC-conductivity is well fitted for k, μ and ϕ_c respectively equal to 375, 0.32 and 2.10^{-3} for wave guide characterisation. It means that percolation in the plane is reached at 0.2% wt. The skin effect is also investigated to verify that conductivity is not limited. Actually, the thickness of the samples is smaller than the skin depth for most composites (assuming that the medium is homogenous). We note that the thickness of the most conductive layers slightly exceeds the skin depth at the highest frequencies. Anyway, the extraction model of conductivity via S-parameters takes into account this effect and provides exact conductivity. For microstrip characterisation, the coefficients k, μ and ϕ_c are equal to 41, 0.67 and 2.10^{-3} respectively. About 2 orders of magnitude separate the out-of-plane and in-plane conductivity.

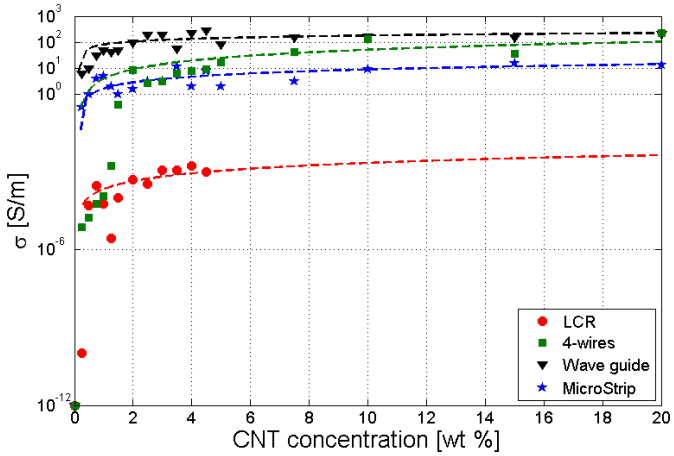


Fig. 36. conductivity of blended polycarbonate-CNT composite. In DC, 4-wires characterisation gives conductivity in the plan xy and LCR characterisation gives conductivity along z in terms of CNT concentration. In AC, wave guide characterisation gives in-plane conductivity and microstrip gives out-of-plane.

CNT ink based composites

An alternative option for dielectric-conductor layer stacking is the deposition and drying of AquaCyl™ on PC films. The dielectric is still pure PC film whereas the conductive layer becomes an ultra-thin coating of entangled CNT. A series of dip coatings has been performed at different AquaCyl™ dilutions. In this subsection, PC is used as support for CNT but the given conductivity is the one of CNT only. Due to practical constraints, we have to measure PC|CNT|CNT|PC double film sets for certain characterisation methods but in this case, we have subtracted the contribution of PC to obtain the pure CNT layer properties. For clarity, when the overall conductivity of sandwiches is mentioned, we are talking about effective conductivity. The amount of CNT attached to the polycarbonate surface is inversely proportional to ink dilution with a resulting control on conductivity. The anisotropy of those films is very strong as evidenced in Fig. 37. DC characterisation shows that conductivity in the plane (4-contact method) is 14 orders of magnitude higher than that measured out-of-plane (by LCR). The CNT cover the polymer as a thin carpet so that the conductivity perpendicular to the film is mainly that of pure polymer. The in-plane conductivity is high and almost constant. The percolation threshold is immediately reached and the conductivity is mainly due to multiple contacts between the carbon nanotubes that are only limited by the presence of residual surfactant from AquaCyl™. The anisotropy is less pronounced in the AC regime. The contact resistance between carbon nanotubes is short-circuited by micro-capacitances between neighbouring CNT, so that AC conductivity is higher than in the DC case. Despite the thinner conductive coating, no skin effect is noticed since the skin depth is far larger than the CNT deposition thickness.

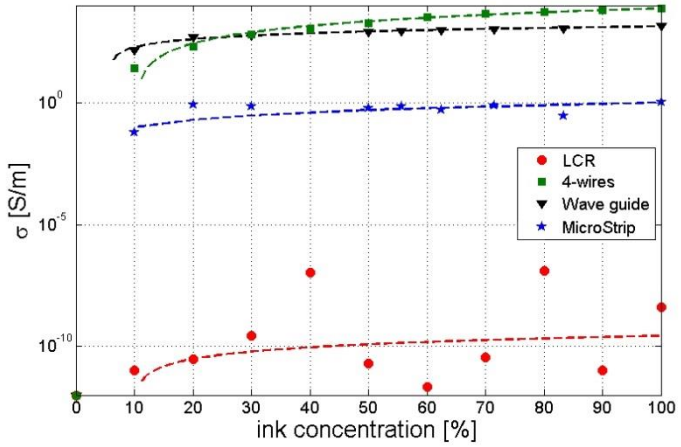


Fig. 37. conductivity of dip coated CNT on polycarbonate surface in terms of dilution of AquaCyl™. DC characterisation is realised in the plan xy (4-wires) and along z (LCR). AC characterisation is measured in the plan (wave guide) and along z (microstrip).

Using pure AquaCyl™ and dip coating is not sufficient to reach the conductivity level needed for maximal absorption. In fact, conductivity must be higher for thin CNT deposits than for blended composites to compensate for the thickness reduction, since the propagation loss equation links σ and thickness t by $|T| = \left|e^{-i\omega t\sqrt{\varepsilon\mu}}\right|$ where $\varepsilon = \varepsilon' - \frac{i\sigma}{\omega\varepsilon_o}$. In other words, a thinner layer must have a higher conductivity to keep the same level of absorption. Dip coating enables to reach conductivity values σ up to ~1500S/m, while the analytical model indicates that conductivity values up to 10^4S/m are needed. So, a new process has been developed to increase the amount of CNT fixed on the polymer. Pure AquaCyl™ has been airbrushed on plasma activated PC surface. After drying, a second layer can be airbrushed to enhance again conductivity (see Table 4). In this way, in-plane conductivity can be increased up to 2.10^5S/m in AC regime for 3 airbrushed layers.

Table 4. conductivity of CNT layer airbrushed on polycarbonate sheet in DC and AC expressed in S/m.

	4-wires	**LCR**	**wave guide**	**microstrip**
1 layer	$4.2x10^3$	$2.2x10^{-9}$	$1.0x10^5$	0.20
2 layers	$8.7x10^3$	$2.7x10^{-9}$	$2.0x10^5$	0.25
3 layers	$12.3x10^3$	$2.4x10^{-9}$	$2.1x10^5$	0.29

For AquaCyl™ based conductive layers, conductivity follows a linear proportionality law rather than a power law as observed for the melt-blended composites. Actually electrical percolation is directly reached because all carbon nanotubes are interconnected, either physically or virtually (via nanoscaled capacitors).

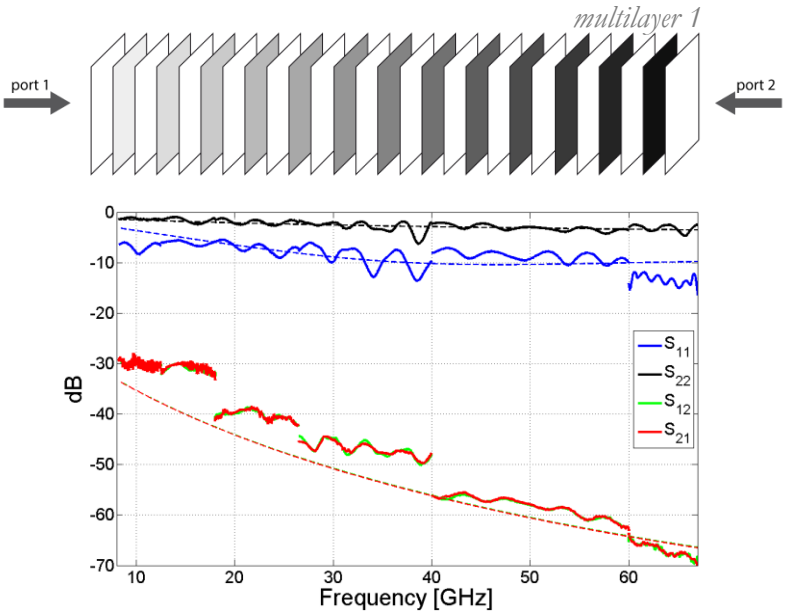
The performed set of electromagnetic characterisations is essential to know the relationship between the CNT concentration (varying according to the implementation method) and the resulting conductivity. We now get an almost continuous range of conductivity from ~$1x10^0$ to $2x10^5$ S/m which directly enters in the composition of absorber multilayers. It has already been shown (in section III-1.1) that stacking alternatively dielectric-conductor film in a gradient of conductivity is particularly effective in terms of absorption (see Fig. 8). Such multilayers are experimentally characterised and discussed in the next subsections. Thereafter, a study of the maximisation of the absorption/thickness ratio is conducted for multilayers based on CNT AquaCyl™ sandwiches.

1.2. Structure for wide band EMI shielding

The model based on chain matrix (explained in section III-1.5) computes the absorption index of a multilayer from the physical parameters and thickness of each layer. We can directly input the measured properties of each layer to simulate the absorption (or other properties) by testing different ways of stacking. It helps us, in the first time, to predetermine especially the best arrangement of the successive composite layers and highlight the potential necessity of additional composite layers to extend the range of conductivity to higher or lower values. It gives also a view of the improvement rate of the absorption in function of the increase of the number of layers. We can so decide of a compromise between absorption and total thickness. Here, conductivity and the number of conductive layers have been defined in order to minimise the total thickness for an overall absorption index above 80%. All theoretical curves fitting the experimental data are stemmed from this model.

The electromagnetic characterisation of each film has been performed using a Vector Network Analyzer with the waveguide technique. We first analyse a multilayer CNT-PC melt-blended composite. It consists of 13 conductive layers whose conductivity

increases gradually from 6 to 290S/m, each with a thickness of about 175µm. By reference to Fig. 36, the range of conductivity is achieved with the help of composites containing from 0.25 to 5% CNT. The 14 dielectric PC layers are 110µm thick each. Further information about this absorber is presented in Annex C (see *multilayer 1*). The absorption index in Fig. 38 clearly depends on the direction of measurement, which is explained by the conductivity gradient effect. The preferred direction is from port 1 to port 2, which is correlated with a lower reflection coefficient at port 1. The figure of merit (see III-1.2) in this direction gives $Q_{1\to2} = 5.2$, which is obviously higher than the same FOM in the opposite direction $Q_{2\to1} = 2.0$. This absorber ensures a level of absorption higher than 80% over the frequency spectrum for a total thickness equal to 4.90mm. The oscillations of the spectrum are due to limitation of the calibration procedure as explained in section IV-3.2. The real value of absorption is a fit through these oscillations.



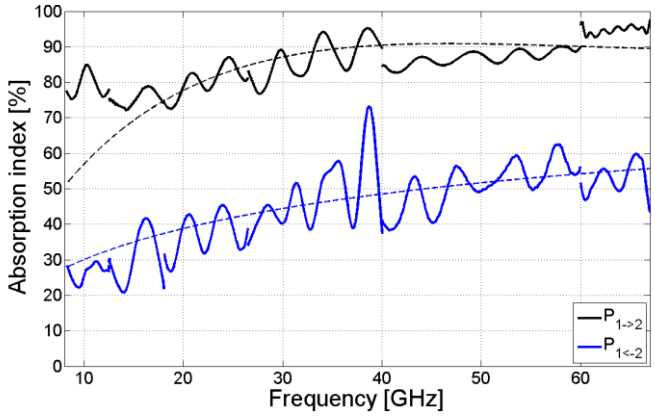


Fig. 38. S-parameters and absorption index of the multilayer at 13 CNT-PC composite layers and 14 dielectric layers according to frequency. Measurements (full lines) are fitted with simulations (dotted lines).

The multilayer based on CNT-ink layers (see *multilayer 2* in Annex C for additional information) is measured in the same way and shows a similar absorption for a lower total thickness (compare Fig. 38 and Fig. 39). By the way, the figure of merit shows a drastic enhancement compared to previous multilayer with $Q = 9.2$. This increase is exclusively due to the decrease of the thickness since the integrals of absorption over wavelength are more or less equivalent. S-parameters highlight a slightly lower transmission for this second absorber. It is probably due to the smaller thickness which is inappropriate for attenuating transmission. Furthermore, the difference in transmission is not compensated by a lower S_{11} reflection (significant in dB) which is even larger at lower frequencies. The ink based gradient nevertheless keeps an advantage over blended composites, since its overall thickness is only 2.56mm. This reduced thickness comes at a price since the lower frequencies are less absorbed, but the difference becomes quickly insignificant beyond ~20GHz.

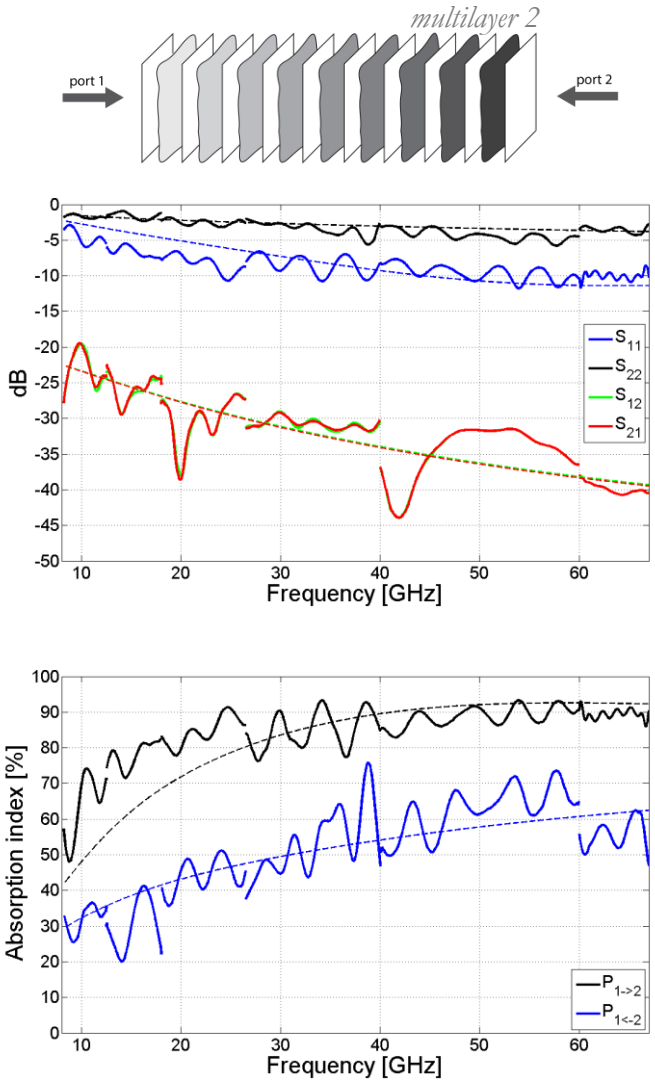


Fig. 39. S-parameters and absorption index of the multilayer at 9 AquaCyl™ coats sandwiched between 10 dielectric layers according to frequency. Measurements (full lines) are fitted with simulations (dotted lines).

The measurements and simulations for the two systems highlight that the direction of incidence has a critical influence on total absorption for a gradient multilayer. Simulations (not shown) prove that absorption below 15GHz is possible at the price of a drastically higher thickness. A suitable conductivity range would lead to an absorber working at lower frequencies.

1.3. Performance assessment through the Rozanov method

The alternation of polycarbonate-composite layers produces an excellent combination for broadband absorber. Furthermore, the stack in gradient of conductivity enhances the efficiency as shown previously. The current subsection aims to gauge the quality of our multilayers so as to assess their effectiveness vs. the state of the art. This requires a method independent from geometrical aspects (such as thickness) and frequency band. The efficiency of any radar absorber is usually determined by the Rozanov method (46). The objective is to obtain the thinnest absorber showing the highest possible absorption. The method is effective over a defined frequency band, but the equation sharply favours a wide band of operation. The samples have to be metal-backed to fulfil the conditions of applicability. Indeed, reflection coefficient only is taken into account by *eq. III-7*:

$$\int_{\lambda_i}^{\lambda_f} \ln R(\lambda)\,|d\lambda| \leq 2\pi^2 \sum_n \mu_n d_n$$

The multilayers studied in the previous subsection are characterised in this way. The gradient multilayer based on extruded PC-CNT composites (*multilayer 1*) has a thickness of 4.90mm, hence $2\pi^2 \sum_i(\mu_i d_i) = 0.0967$. Its integral reflectance equals 0.0275 so the Rozanov inequality is verified since $0.0275 \leq 0.0967$ but we are far from the optimum. It is obvious that extruded composites are less suited for approaching the Rozanov limit due to their larger thickness. Actually, the ink-based absorber (*multilayer 2*) does not radically give better result. The Rozanov integral (*eq. III-7*) gives 0.0245 which is far from $2\pi^2 \sum_i(\mu_i d_i) = 0.0505$. The poor performance comes from the substantial reflection of these multilayers for lower frequencies. In addition to a small thickness, the Rozanov formalism favours a weak reflectivity especially for longer wavelengths λ. The previous multilayers were suited for a maximal mean absorption index over the spectrum at the expense of greater thickness. They must be now adapted to come closer to the optimum according to the Rozanov conditions. To this end, we have developed a Matlab script to compare all possible structures and select the most adapted according to the Rozanov formalism.

1.4. Optimisation of the gradient stacks for the Rozanov optimum

Preliminary simulations have quickly confirmed that the previous multilayers have, as major inconvenient, an excessive reflectivity. The thickness also becomes problematic for PC-CNT composites based absorbers. An ink based absorber has better aptitude to achieve the Rozanov optimum thanks to its very low thickness. For this reason, we focus in this section our simulations and characterisations on AquaCyl™ based multilayers. We run a series of simulations to determine the best parameters and arrangement. We use the chain matrix method (see section III-1.5) to simulate the scattering parameters (S-parameters) and absorption index. Some conditions are imposed to match the available materials with the model. Dielectric spacers are polycarbonate whose the physical properties are fixed. On the other hand, the thickness of each layer is taken as a free variable. Simulations studying this variable have proven that the larger the dielectric thickness d, the higher the absorption, especially at lower frequencies. However, the incident and reflected waves are in phase, when the thickness spans half a wavelength:

$$\mathrm{d} = \frac{1}{2}\frac{\mathrm{v}}{\mathrm{f}} \qquad \textit{eq. V-1}$$

where v is the speed of light in polycarbonate and f the frequency. At the corresponding frequency, the absorption abruptly vanishes and hence the condition described by *eq. V-1* represents an upper limit for the thickness of the dielectric layers. The corresponding thickness is equal to 1.016mm, much higher than our multilayers. So, dielectric layers do not require any free variable. In summary, the properties ascribed to the dielectric layers are those of polycarbonate: $\varepsilon_r' = 2.8$ (in GHz-range, corresponding velocity $\mathrm{v} = 1.79\,10^8\mathrm{m/s}$), $\mu_r = 1$ and $\sigma = 10^{-12}\mathrm{S/m}$. With regard to the conductive layers, they are made of entangled CNT. In the absence of magnetic particles, the effective permeability is thus equal to 1. The CNT concentration controls conductivity but it imposes permittivity at the same time. Actually, permittivity is related to the concentration of CNT but its variation is negligible compared to the influence of conductivity. However, the model takes into account the evolution of permittivity with CNT concentration via the empirical law ($\varepsilon_{\mathrm{comp}} = 3 + \frac{\sigma_{\mathrm{comp}}}{1500}$). The thickness of the CNT layers only has a minor impact in the sense that increasing thickness is almost equivalent to increasing conductivity. We decide for convenience to fix the thickness

of conductive layers at 120µm (which fits the real composites). The major part of the optimisation lies then in the best evaluation of the conductivity for each conductive layer. The numbers of layers is also a free variable so that the operation is reiterated for different numbers of conductive layers.

The Matlab function *fmincon* uses the analytical model implemented as a Matlab routine to determine independently the optimal conductivity of each conductive layer. This optimum for a maximum of absorption averaged over the 8-70 GHz spectrum is determined for configurations having 1 to 10 conductive layers. The result is shown in Fig. 40 (bullets). For comparison, we also show a stack with a linear gradient of conductivity (stars). For a correct correspondence, each linear gradient stack is built with an average conductivity equal to the average conductivity of the equivalent optimum stack. For example, the optimum multilayer based on 3 conductive layers has an average conductivity of 27S/m, the stack with linear gradient is built such as the average conductivity is the same.

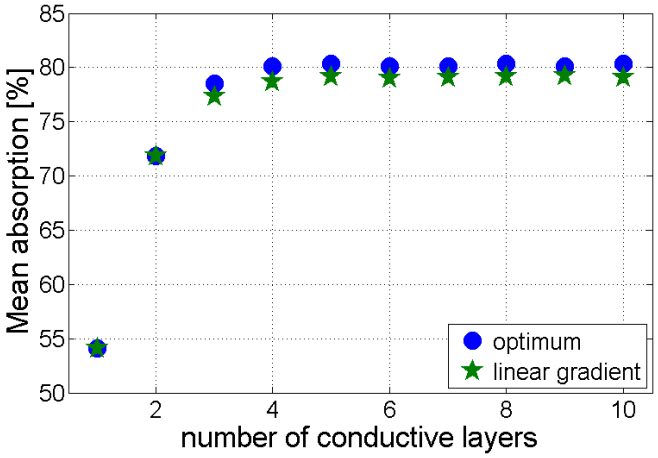


Fig. 40. average absorption calculated over 8-70GHz spectrum versus the number of conductive layers in the multilayer. Dots show results for optimisation of conductivity of each layer while stars show absorption resulting from a linear gradient of conductivity from layer to layer (163).

Fig. 40 shows that a linear gradient of conductivity provides average absorption nearly equivalent to the arrangement resulting from the optimisation of the conductivity of each layer. The average absorption reaches a plateau at ~80%. It is not possible to absorb beyond this limit

because the permittivity of first layer is higher than one. The absorption index would be higher if the permittivity of layers starts from 1 (avoiding reflection at input). It also appears useless to exceed 4 conductive layers (and 5 dielectric ones) since it is obvious that the average absorption reaches a plateau beyond that number.

The measurement of the improved topology (*multilayer 3*) is shown in Fig. 41. The inset scheme illustrates the measurement method. The incident wave enters the multilayer at port 1 only and is totally reflected by the metal plate (in black) at the boundary. The Rozanov inequality *eq. III-7* gives the encouraging result: $0.0675 \leq 0.0720$. This shows that we are very close to the Rozanov limit. Reaching this ultimate limit would require having a thickness of 3.42mm instead of 3.65mm. The absorber presented here is very effective because of its relatively small thickness and broadband of operation. However, the optimisation for the Rozanov formalism is not optimal for a high FOM. The FOM is based on measured absorption index (without back-covered metal) instead of reflection only. This multilayer gives a theoretical factor $Q = \frac{0.0223}{t} = 6.1$ (not measured).

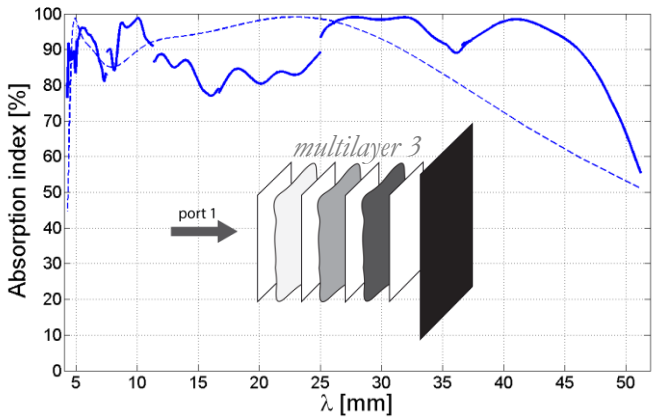


Fig. 41. Characterisation of AquaCyl™ based composites following metal-backed topology of Rozanov. The multilayer is composed of 4 pure polycarbonate films sandwiching 3 CNT depositions. The inset shows the structure in gradient of conductivity with a metal foil at the back.

1.5. Conclusion

The concept of multilayers organised in gradient of conductivity opens up new routes for broadband microwave absorbers. The multilayer structures can be considered as relatively flexible and thin foils. They can cover electronic devices, medical devices or others small systems to isolate them from external and internal fields. Such absorbers could be produced on a larger scale, and could cover a room or a building for a complete isolation. The analytical model developed to simulate the structures is built on the relatively simple concept of chain matrix. The correlation with the measurements is nevertheless totally acceptable. Furthermore, the model is the core of an optimisation study performed to determine the most efficient configuration in order to get closer the ultimate limit defined by Rozanov. It highlights the versatility of the model and the experimental method. The multilayers provide excellent results over the 8-67GHz spectrum in terms of absorption index only and according to the Rozanov formalism.

2. Nanowires based composites for EMI shielding

CNT have proved their efficiency in the broadband absorption area. We aim to compare and potentially improve the previous results by similar multilayer based on nanowires. The strategy of stack in gradient of conductivity described in previous section is kept. The first section describes the use of PC nanocomposites containing gold nanowires (Au-NW) for EMI shielding. The composites exhibit potentially interesting absorption because of the higher intrinsic conductivity and aspect ratio of Au-NW as compared to CNT. The characterisation of the corresponding composites is detailed and compared to CNT composites.

Metal NW composites have the advantage over CNT composites of the choice of the metal. In the second section, we evaluate nickel nanowires (Ni-NW) combined with PC which confers a complex permeability μ_r to the systems. With magnetic films, we attenuate the magnetic field as well as the electric field of the incoming waves. Referring to Rozanov equation (*eq. III-7*), this opens the possibility to further decrease the total thickness (or the reflectance). The method of production of the nanofillers, their implementation and their EM response are presented and discussed.

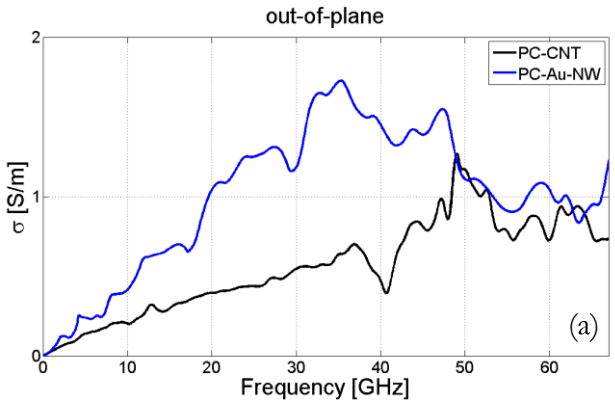
2.1. Gold nanowire-polycarbonate composites

Gold nanowires (Au-NW) have a flexible wire shape similar to that of carbon nanotubes. Their aspect ratio (as produced) is of the order of

1000 while that of CNT does not exceed 100. Conductivity of the multiwall CNT used in this thesis is difficult to determine precisely especially because they contain a collection of different types of tubes with defects. We can still estimate that the intrinsic conductivity of Au-NW is higher than that of CNT. Gold is chosen for its high conductivity and its very low tendency to oxidation. Others metal (like copper) quickly form a coat of oxide drastically reducing the surface conductivity. Gold is inert and avoids this kind of problem.

Compounded PC - Au-NW composite

The nanowires have a significantly higher volumetric mass density than CNT so that a composite PC-1%wt. NW contains a lower volume of fillers than the equivalent 1%wt. CNT composite. The experimental practice forces us to work in term of weight regardless of the difference in volume of nanocharges. The Au-NW are produced by the process described in section IV-1.2. They are implemented into polymer by two methods given in section IV-2.4. In the present subsection, we focus the investigation on the implementation by solvent only. Fig. 42a shows the microstrip characterisation of a PC composite with 1%wt. Au-NW compared to a 1%wt CNT composite. While the volume of gold nanowires is clearly lower than that of CNT, the out-of-plane conductivity is slightly higher for the PC-Au-NW composite. However, in-plane conductivity of the CNT composite exceeds that of the Au-NW composite.



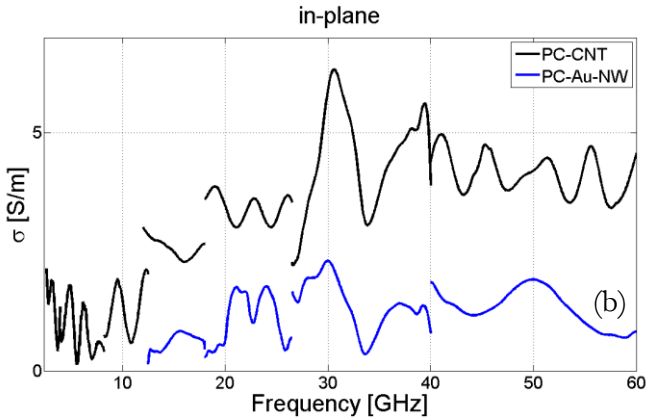


Fig. 42. out-of-plane conductivity (in a) and in-plane conductivity (in b) of PC-Au-NW and PC-CNT composites filled at 1%wt.

An interpretation of Fig. 42 could be that the spatial distribution of Au-NW is more isotropic than that of CNT. Actually, this is probably not due to any specific property of the NW; the origin resides in the blending process. In order to produce samples which are easy to handle, the Au-NW-PC films are kept thicker. Indeed, PC-NW composites are more brittle than their CNT counterparts. The origin of this change of mechanical property is discussed in Annex B. The composites are kept thicker during compression moulding (the minimum thickness is 1mm instead of 400µm or even less for CNT composites). This implies a lower planar orientation of nanofiller. As proof, a much thinner (~20µm) highly squeezed film containing 1% Au-NW was produced by using a PTFE film as support to make the Au-NW-PC film handlable. The stronger orientation of the nanowires is directly visible from the electromagnetic characterisation. The average out-of-plane conductivity is 0.02S/m and the average in-plane conductivity reaches 20S/m.

The size of gold nanowires allows their individual observation under the optical microscope. Pictures in Fig. 43 show a good general dispersion with some rare agglomerates. We observe also that the mean length of the nanowires is shorter than initial 100µm (thickness of alumina membrane).

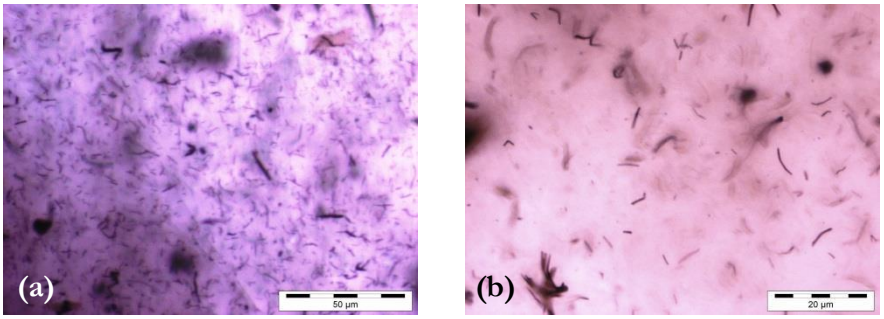


Fig. 43. PC-1%wt. Au-NW composite observed in optic (50x in (a), 100x in (b))

The PC-Au-NW composites exhibit same order of magnitude conductivity as CNT composites at similar weight concentration. This is evidence of the effectiveness of conductive nanowires to quickly generate a percolating network despite a small volume of nanoparticles. The Au-NW composites form a viable (albeit expensive) alternative to CNT composites. Their poor mechanical strength nevertheless remains a major limitation. We have hence decided then to modify our method of combining metal nanowires with PC bypassing the brittleness issue. The method introduced hereafter cumulates the advantage of a thinner conductive film with a much better mechanical resistance.

Thin Au-NW deposition on PC film

This section presents a method of depositing entangled Au-NW over a PC surface. The nanowires are first extracted from the alumina template by the method described in section IV-1.2. The dispersion of NW in caustic soda is ensured by a strong ultra-sonication. At this stage, the Au-NW are directly filtered through a nanoporous polycarbonate membrane. A carpet of nanofillers is next sandwiched between two PC films to protect the structure. More details are given in section IV-2.4. Optical microscope pictures show the very high density of nanowires over the filter surface in Fig. 44a, and after hot-pressing of this filter between PC films Fig. 44b.

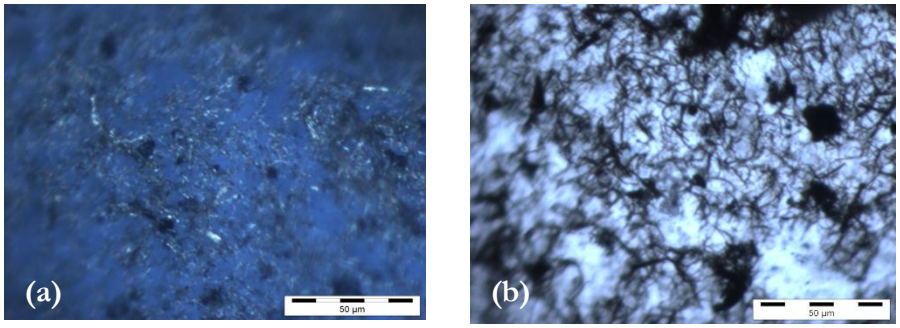


Fig. 44. filter covered of entangled Au-NW in (a) and the same filter stacked between polycarbonate sheets in (b)

The ultra-thin Au-NW-PC sandwiches present undeniable similarities with AquaCyl™ based CNT-PC sandwiches. It is not relevant to perform a detailed comparison between those two types since the quantity of nanofillers is very difficult to quantify in the CNT case. However, an analysis of their in-plane and out-of plane conductivity brings important information. The EM response of a sandwich containing 34mg of Au-NW (over a surface of 950mm²) is given in Fig. 45. The in-plane conductivity is significant which proves that we have an electric percolation. Fig. 45b shows that conductivity increases with frequency. This behaviour is probably due to capacitances which are short-circuited at higher frequencies.

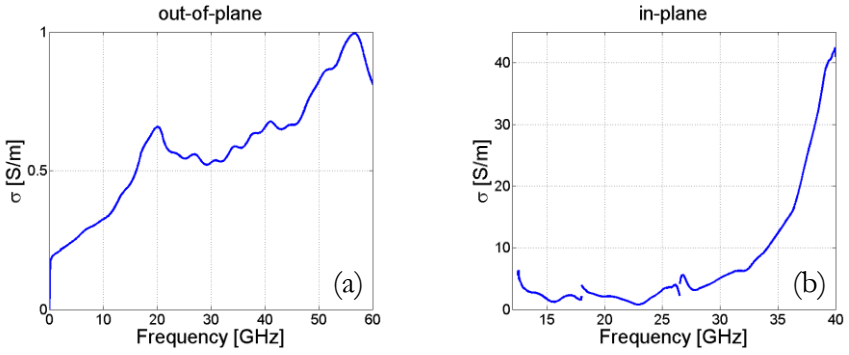


Fig. 45. out-of-plane conductivity (in a) and in-plane conductivity (in b) of 34mg of Au-NW sandwiched between two PC sheets.

The studied Au-NW systems are an interesting step towards the development of homogenous dispersions of metallic nanowires in

polymers. However, they lack magnetic properties. The next section introduces Ni-NW composites and sandwiches to assess the potential advantage of this additional characteristic.

2.2. Nickel nanowires-polycarbonate composites

Gold was initially chosen because it is an inert metal having a high conductivity. We now extend this investigation to magnetic nickel nanowires. The corresponding composites and sandwiches hence possess non-trivial permeability characteristics on top of permittivity and conductivity. Playing with the magnetic field of an incoming wave opens new possibilities. The absorption index can be increased since the system acts on the magnetic field of an electromagnetic wave as well as the electric field. This ability is confirmed by the Rozanov equation (*eq. III-7*) which shows that the thickness of an absorber can be decreased if μ is higher than 1. The control of permeability enters also in the design of invisibility systems. Even if it is not mandatory to manage μ, it extends the possibilities for layered invisible cloaks.

EM characterisation and absorption measurements

Some PC-Ni-NW composites at low nickel content of 0.5%wt were produced by the implementation by solvent given in section IV-2.4, despite their poor mechanical strength, in order to determine their EM properties. The observation by optical microscopy shows a very good dispersion considering that the magnetic particles tend to agglomerate. Unfortunately, the EM characterisation does not allow detecting a magnetic behaviour. The 0.5%wt. concentration of Ni-NW is totally insufficient to detect any magnetic response. The Ni-NW concentration needed to generate magnetic response should be increased. Moreover, the random orientation of nanofillers does not participate to the alignment of the magnetic dipoles of nanowires. Those considerations confirm the interest to use the sandwiching process for Ni-NW systems. It should hopefully enhance the magnetic response thanks to a potential higher concentration (not limited by brittleness) and significantly increase the in-plane orientation.

The sandwiches offer two main advantages. First, the mechanical properties of the PC films are not degraded by the interaction with the NW. Next, the confinement of the NW allows an efficient use of the nanofillers since the percolation threshold is quickly reached (also helped by the very high aspect ratio of the NW). Fig. 46 illustrates the distribution of nanowires on a filter. Fig. 46a is an optical microscopy image of a sandwiched filter covered by 30mg Ni-NW, corresponding to 100C electrodeposition (see *eq. IV-3*). Fig. 46b is a direct view of the filter covered by 4.5mg (or 15C) of Ni-NW.

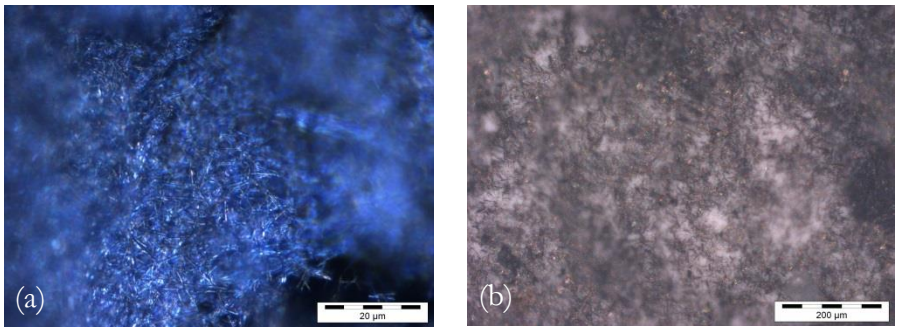


Fig. 46. Optical picture of a sandwich of 30mg of Nickel nanowires in (a) and a filter covered by 4.5mg of Ni-NW in (b).

The ferromagnetic properties of the sandwiches have been revealed by hysteresis loops. Fig. 47 shows in-plane and out-of-plane characterisation of sandwiches corresponding to 4.5mg (or a density of 0.47mg/cm²) and 30mg (3.16mg/cm²) of Ni electrodeposition respectively. The saturation magnetic moments and anisotropy are more pronounced as the quantity of Ni-NW increases. For instance in Fig. 47b, the out-of-plane hysteresis loop is more tilted than in-plane proving that this film has a stronger permeability depending on the direction. The hysteresis loops reveal a magnetic response of the material but they are not valid to quantify any property since it is depending on frequency (164). We hence proceed next to characterisation in the GHz-range in order to obtain the required parameters for preliminary simulations.

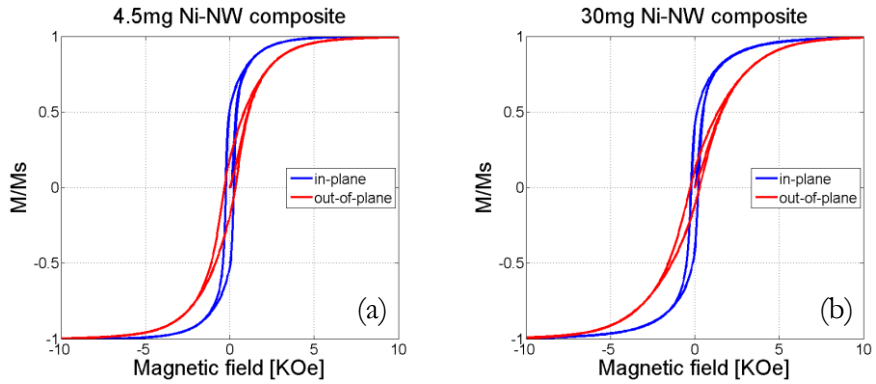


Fig. 47. In-plane and out-of-plane hysteresis loops of composite with 4.5mg in (a) and and 30mg of Ni-NW in (b)

The thin sandwiches have been characterised in order to define their complex permittivity ε and complex permeability μ in the microwaves range. Complex permittivity (described by *eq. III-11*) contains information about the dielectric constant, which is close to pure PC for all composites, and about conductivity which is dominated by the imaginary part of ε. Permeability is also defined by a complex number $\mu_r = \mu'_r + i\mu''_r$ in AC where i is the imaginary number. The sandwich with 4.5mg of Ni-NW is measured by wave guide in order to determine the in-plane properties. Fig. 48 reveals the conductivity and magnetic response provided by NW network. Note that the experimental oscillations are due to a slight impedance mismatch of the wave guide over the swept frequency range. Furthermore, the algorithm for extracting the physical properties from S-parameters inevitably amplifies these oscillations.

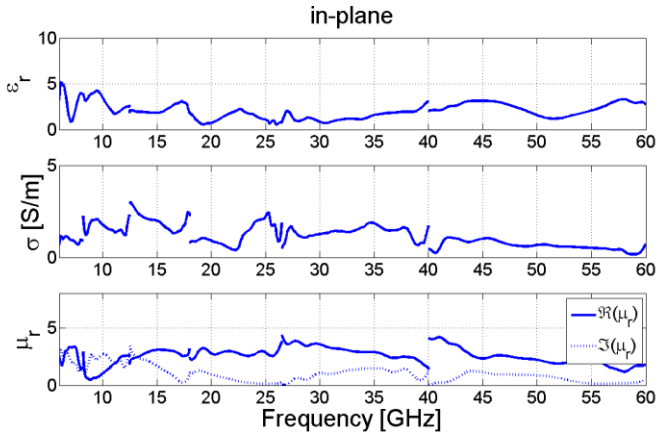


Fig. 48. in-plane characterisation of a sandwich based on 4.5mg of Ni-NW deposited on a PC filter and sandwiched between 2 PC sheets

Besides the above example, composites with different amounts of Ni-NW have been characterised. It is possible to obtain a range of values for ε_r', σ, μ_r' and μ_r'' depending on the quantity of deposited nanowires. Fig. 49 gives the complex permittivity and permeability of Ni-NW based composites as a function of the mass of nanowires for the fixed surface of 950mm². The values of σ, μ_r' and μ_r'' tend to increase with the concentration of nanofillers which is suited to enhance the absorption. Complex permittivity as a function of the fillers concentration is fitted with the experimental formulation given by *eq. III-28*. A variant of this law is used for permeability to match the physical response of its real part: $\mu_r' = k(\phi - \phi_c)^v + 1$. The objective is to reach more or less balanced increase for conductivity and permeability to maximise the absorption. This compromise could not be achieved with, for instance, a nanometric surface deposition of Nickel because the magnetic influence would be negligible compared to conductivity. Indeed, the bulk conductivity of Nickel is highly dominant compared to gain on ferromagnetism. The entangled nanowires strategy decreases drastically the effective conductivity of the Ni-NW network because of presence of electrical contact resistances which reduce conductivity but are not significantly affecting the permeability. Furthermore, it is simple to control precisely conductivity and permeability by the quantity of the Ni-NW. This is advantageous here to control favourable properties for absorption.

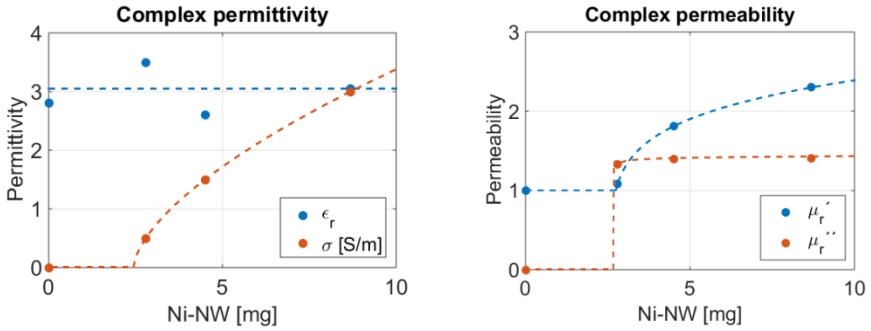


Fig. 49. conductivity and permeability of Ni-NW PC sandwiches as a function of the mass of Nickel

The so-made series of conductive-magnetic sandwiches is useful to build absorbing multilayers obtained by stacking such sandwiches. An arrangement in a gradient of conductivity-permeability is the best solution to progressively attenuate the incoming EM waves. The increasingly conductive network absorbs the electric field through the multilayer (163) without significantly reflecting the energy. The same applies for the layer by layer increase of permeability that gradually attenuates the magnetic field of the waves. Fig. 50 shows the results of a 4-layers absorber built from Ni-NW sandwiches (listed as *multilayer 4* in Annex C) measured in Fig. 49. The measurement is compared with a 4-layers stack 700µm thick of CNT composites arranged with the same gradient strategy described in section III-1.1. The conductivity of each CNT composite layer is equivalent to that of the Ni-NW composites in order to separate the contribution of the sole magnetic component. Complementary information is provided in Annex C for this absorber listed as *multilayer 5*. The two multilayers follow the same gradient. Unsurprisingly, the absorption index favours the Ni-NW based multilayer. Its total thickness is only 600µm while the mean absorption index over the spectrum is 90%. S-parameters in Fig. 50 show that reflection (S_{11}) and transmission (S_{21}) are still significant for the PC-CNT multilayer, explaining the worse absorption. Decrease of S_{11} is favoured by a characteristic impedance Z_c closer to that of air, meaning that μ_r' has to get value higher than 1 to compensate the permittivity of the composite. Likewise, S_{21} is decreased thanks to high μ_r'' via transmission coefficient T. Fig. 50 hence confirms that magnetic nanowires-based sandwiches combined with a gradient arrangement are very efficient for microwave shielding. The dotted lines are the predictions of the multilayer computed from measured physical parameters of each separated layer directly used as input. Unsurprisingly, the FOM also

confirm the advantage of the Ni-NW based multilayer (*multilayer 4*) over the CNT based multilayer (*multilayer 5*) with respectively $Q_{m4} = \frac{0.0323}{600.10^{-6}} = 53.8$ and $Q_{m5} = \frac{0.0271}{700.10^{-6}} = 38.8$. Actually, *multilayer 4* is favoured by a better absorption index and the smaller thickness.

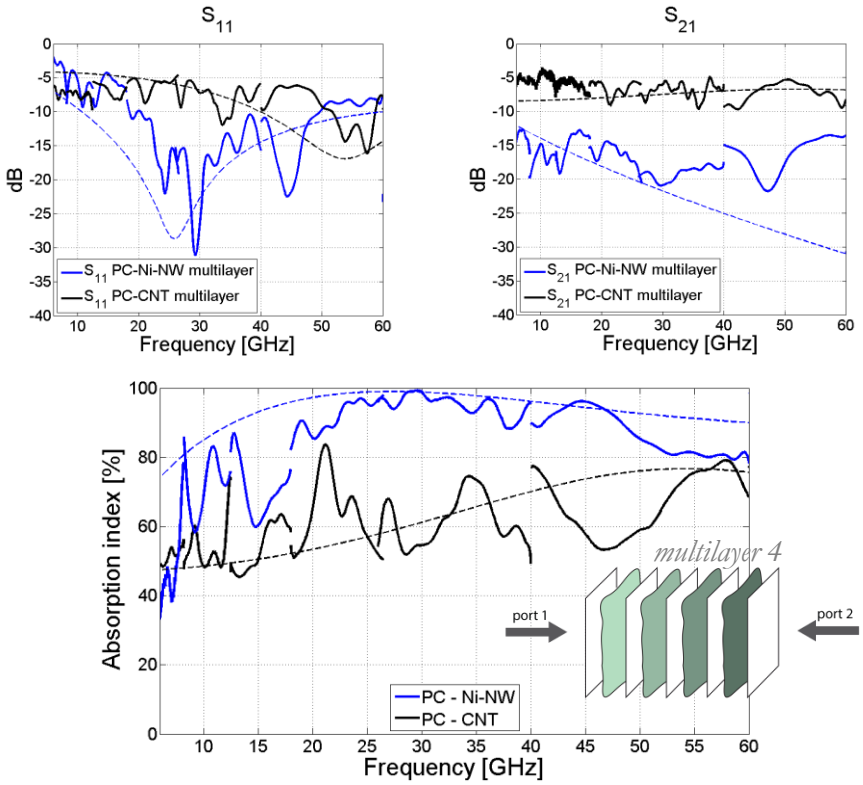


Fig. 50. comparison between PC-Ni-NW and PC-CNT 4-layer structures whose complex permittivity is equal but relative permeability only is different. S-parameters show lower reflexion S_{11} and transmission S_{21} of Nickel based absorber than CNT based multilayer. The absorption index follows the same trend and proves that the PC-Ni-NW multilayer is more efficient. The dotted lines are the theoretical predictions of layers stack.

The fine-tuned and combined control of conductivity and permeability in a smart conductivity/permeability gradient stack hence leads to very high-efficiency absorbers. In the next subsection, the absorption analysis is performed by the Rozanov formalism to compare the performance to the theoretical limit.

Performance assessment through Rozanov method

The two 4-layer absorbers described hereabove are characterised following the Rozanov formalism. Referring to *eq. III-7*, for the same absorption target, the thickness d_n can be decreased inversely proportionally to μ_n. The Nickel nanowires based multilayer exhibits a higher absorption and maintains it even at higher wavelength. Fig. 51 shows the experimental results (full lines) compared with the simulated prediction (dotted lines). This is especially favourable in the Rozanov formalism because the integral on the left side of *eq. III-7* is over a relevant wavelength range. On the other hand, the distance from the ultimate limit is more or less similar for the two samples because the Rozanov inequality takes into account the relative permeability on the right side. For the magnetic multilayer, the integral on the reflection coefficient equals 0.0339 which verifies the inequality condition since $2\pi^2 \sum_i \mu_i d_i = 0.0564$. The corresponding CNT based multilayer is slightly less efficient as a non-magnetic absorber with $0.0041 \leq 0.0138$. In the latter case, the CNT based absorber could move closer to its limit with a gradient of conductivity better adapted for non-magnetic layers. Indeed, the control of its gradient of conductivity is modelled on the one of Ni-NW films multilayer which is not optimal. Better results were, for instance, obtained with CNT only based multilayer (see section *V-1.3*). Anyway, the addition of magnetic properties in a gradient stack provides a better absorption index with a lower thickness as highlighted by Fig. 50 and Fig. 51.

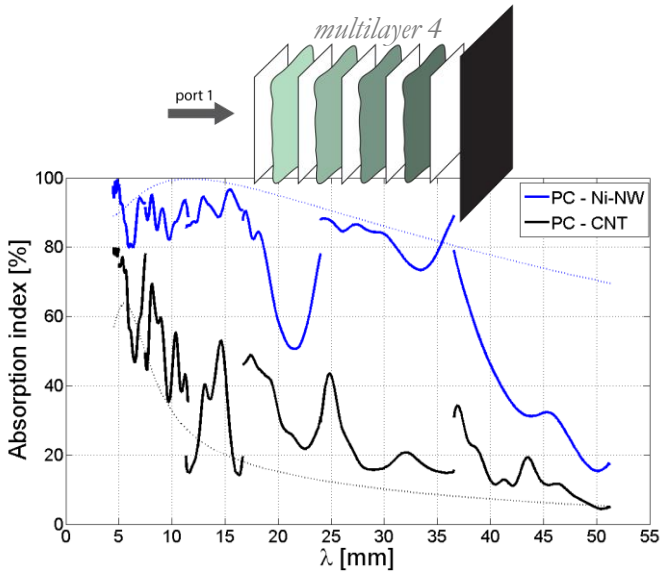


Fig. 51. characterisation following the Rozanov formalism of two multilayers based on CNT and Ni-NW. Both structures are composed of 4 PC-Ni-NW or PC-CNT sandwiches whose physical properties are equal except for permeability. The inset illustrates the multilayer back-covered by a metal foil (in black). The dotted lines are the predictions for each stack.

2.3. Conclusion

Au-NW composites have been investigated as a comparison with CNT composites and for developing a general process suited for metallic nanowires. Our interest has next moved to ferromagnetic Ni-NW nanowires. The use of magnetic films allows raising the level of absorption at the same thickness. Interestingly, Rozanov rules out such a high absorption for so thin a structure in the absence any magnetic property. This advantage comes at a price; it is at the moment hardly conceivable to produce such absorbers at large scale. CNT production is now well controlled; hence it is possible to make large areas of PC-CNT multilayers. By contrast, the mass production of metal nanowires is still a slow and complex process. Realistically, Ni-NW film absorbers are limited to small surfaces. They seem particularly suited for specific compact devices such as microchips, sensors or medical probes. The simulations highlight the total adaptability of the systems to other wavelengths. It is thus conceivable to move the working frequency spectrum if needed.

3. Anisotropic composites for polarisation

The carbon nanotubes or nanowires based multilayers have proved their high efficiency for the broadband microwave absorption. This section first brings the polarisation sensitivity of the absorption index. We now work with films whose conductivity varies with direction in the plane. An anisotropic structure is formed by parallel lines drawn with carbon nanotubes on polycarbonate (see IV-2.3). These films will be competing with a PC-CNT composite with oriented charges (see subsection IV-2.1). The electric field is affected by conductivity so that the absorption index of an incident wave depends on the alignment of its polarisation with the conductive direction.

A variant of this anisotropic multilayer can induce a rotation of the electric field to the desired angle. The loss thus becomes a drawback since the multilayer aims to switch the polarisation without absorption. The current anisotropic films have proved their ability to fulfil this task. Some prospects based on simulations are given as an avenue towards optimisations of the present structure.

3.1. Electrical and morphological characterisation

We elaborate an anisotropic material at nanoscale thanks to the orientation of the charges themselves in the polymer. The CNT are aligned in one direction in the plane. The process is described in paragraph IV-2.1. Here, only one concentration of 2% CNT is used because of practical limitation of production. The in-plane DC measurement is made parallel and perpendicular to CNT. The average

values are given in Table 5. Actually, the anisotropy in the material is weak in term of DC conductivity.

Table 5. DC characterisation by 4-wires probe of oriented (2%) CNT composite

	Mean conductivity [S/m]	**standard deviation**
parallel	$1.99\ 10^{-8}$	$1.73\ 10^{-9}$
perpendicular	$1.96\ 10^{-8}$	$2.49\ 10^{-9}$

The weak conductivity makes sense if we look at the organisation of CNT at nanoscale. Fig. 52 shows the alignment of carbon nanotubes in polycarbonate. They are not connected to each other in any direction. Then it is logical that the conductivity is very low in all directions. We need to characterise in AC to see an electrical anisotropy because the coupling capacitance between carbon nanotubes ends is short-circuited.

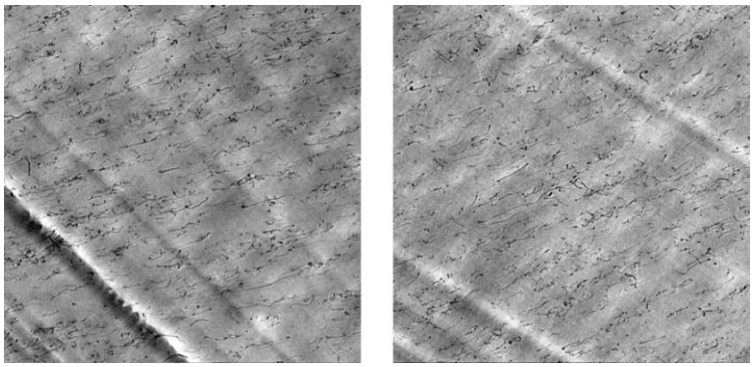


Fig. 52. TEM images 5000x of oriented CNT by stretching. The composite is 2% of CNT in polycarbonate.

The response is made by microwave (in-plane) along the two axes in the plane. Let's assume that the nanotubes are oriented in x axis in the xy plane. The waveguide measurements give the conductivity (in x direction) parallel to the fillers and (in y direction) perpendicular to the fillers. The microstrip measurement gives the out-of-plane conductivity (along z) which is perpendicular to the plane (and fillers). The measurements in y and z direction are close to each other. The conductivity parallel to the CNT is higher which shows the influence of the orientation.

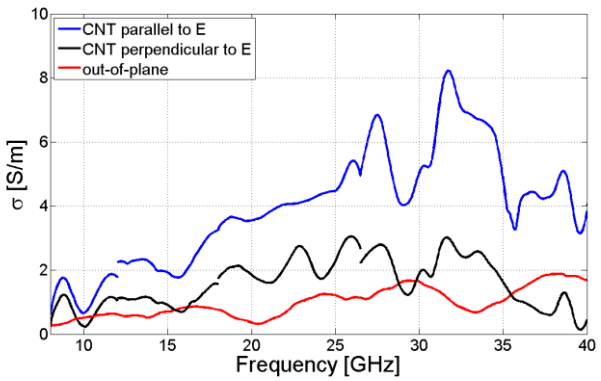


Fig. 53. AC characterisation of aligned CNT composite. Conductivity is given for the electric field oriented in parallel and perpendicularly to the CNT in-plan and out-of-plane.

3.2. Polarisation-selective surface

Oriented CNT composite

The conductivity of the composites varies with the measurement direction. The control of conductivity is the key for high absorption. An adequate conductivity could lead to an efficient absorber but, on the opposite, a too weak conductivity makes the multilayer almost transparent. This concept can be exploited to design a selective absorber depending on the polarisation. Assuming that the incident wave is polarised, the absorption index will be higher for an electric field parallel to the nanotubes. We start our investigation with oriented CNT composite. This polarisation-selective absorber is a PC-2% oriented CNT multilayer (see Fig. 54). The stack is composed of four 100µm thick PC films alternating with 3 PC-oriented CNT composite films. As

the concentration of CNT is imposed by processing constraints, the thickness of the conductive composite films is increased to get a gradient effect. The thickness of the conductive layers is increasing from 125 to 250 and 375 μm in the propagation direction. The gradient structure has the advantage to enhance the absorption index as explained in the previous sections. S-parameters are shown in Fig. 54 for parallel and perpendicular to CNT polarisation of the incident electric field.

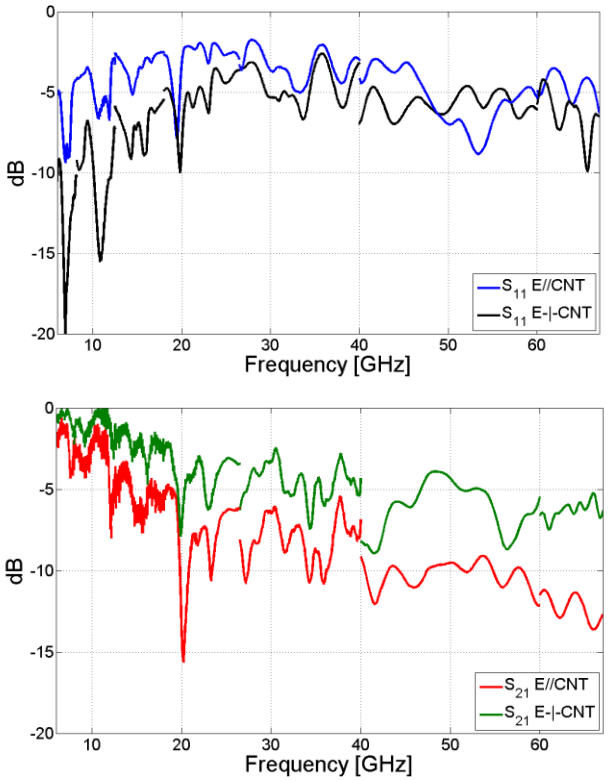


Fig. 54. comparison of S-parameters for multilayers where CNT are parallel or perpendicular to electric field.

S-parameters do not exhibit significant difference for reflection. On the other hand the transmission shows a gap which evidences anisotropy. The orientation of CNT could be enhanced in order to increase the anisotropy. Unfortunately, the process was limited by the brittleness under strain of the composite above a certain drawing speed. A lower molecular weight polycarbonate or a lower T_g polymer could allow stretching the composite to larger strain and it would thus improve

the alignment of CNT. This avenue is worth exploring more deeply because it is likely to lead to a potentially very efficient system.

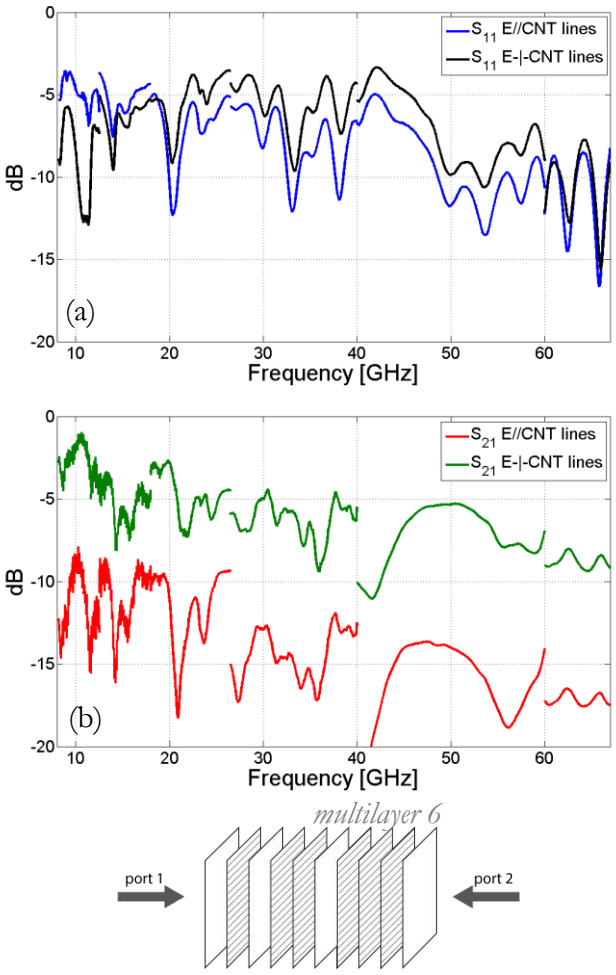
The AquaCyl™ lines based composites could bypass the limitations encountered with CNT oriented composites. Their isolated gap between lines of CNT could enhance the anisotropy. Moreover, the electrical network along the lines of CNT is certainly more conductive than the oriented CNT network of the previous anisotropic films. Those educated guesses are verified in the section hereafter.

Patterned AquaCyl™ based composite

Lines of AquaCyl™ are drawn on activated polycarbonate sheets. The pattern is obtained by a projection of CNT ink through a mask. The process is described in paragraph IV-2.3. All the lines are 0.5mm thick and the spacing between the lines is summed up in Table 3. For convenience, we take the sample names given in Table 3: narrow, medium, large, wide. DC conductivity obviously shows a clear gap between CNT deposition and pure PC. The lines have a conductivity of about 200S/m while pure polymer areas are below the sensitivity of the equipment (theoretically 10^{-12}S/m). The AC characterisation by wave guide measures S-parameters which are the average response over the surface. The structural information is not detectable because it is smaller than the wavelength. However, we do not lose the finger print of the anisotropy since the effective conductivity depends on measurement direction. When the electric field is parallel to the network of lines, the conductivity is higher than when it is perpendicular. All samples follow this rule whatever the structure (narrow, medium large or wide) may be. We observe a trend to increase the anisotropic effect when the space between the lines decreases. Due to this observation, we focus our investigation on the *narrow* patterned structure.

We stack the layers with the same topology as the CNT oriented composites discussed above. The dielectric layers are 100µm thick pure polycarbonate sheets. The patterned composites are each 125µm thick. We stack one, two and three layers between dielectric films (see inset of Fig. 55 or *multilayer 6* in Annex C) in order to reproduce the same thickness as oriented CNT composite-based systems. The composites are precisely stacked so that the CNT parallel lines are perfectly aligned through the entire multilayer. This amplifies the polarising effect layer

after layer. The thickness and arrangement of each layer are thus equivalent for the two kinds of polarisation-selective absorbers.



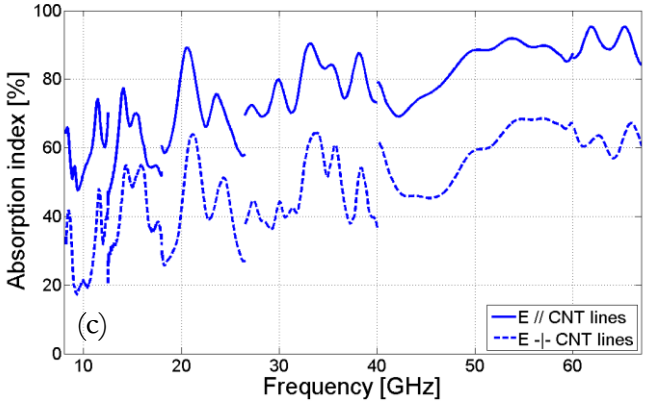


Fig. 55. polarisation-selective absorber based on parallel AquaCyl™ lines patterned on PC sheets. The multilayer consists of 3 structured composites separated by 4 dielectric layers. The full curves give the absorption index when the electric field E is parallel to the CNT lines; the dotted lines give the characterisation for E perpendicular to lines.

The first two graphs of Fig. 55 give S-parameters of the multilayer built with the *narrow* network of lines. Reflexion S_{11} for parallel or perpendicular polarisation is close but a gap of ~10dB is opened for transmission S_{21} at all frequencies. The FOM also favour the parallel absorber with $Q_{\parallel} = 18.2$ compared to the perpendicular case with $Q_{\perp} = 11$. We note there is a larger anisotropy for the patterned lines system than for the oriented CNT composite multilayer. Fig. 55c shows that the absorption index for an electric field E parallel to the lines is on average 30% higher than the perpendicular case. The parallel CNT lines are therefore more sensitive to the polarisation of the waves. The major limitation of oriented CNT composite films is probably an undesired short-circuiting by micro-capacitances between the parallel CNT in addition to the short-circuiting along the alignment direction. We can conclude that the best polariser absorber would be based on conductive lines structured at microscale. The polariser could be a prefect alignment of ultra-long CNT in the matrix at very low concentration (to avoid parallel interaction). A recent CVD process allows producing 0.5mm long CNT (165). An alignment of such long CNT would provide a strong anisotropy and efficient polariser films.

3.3. Microwave twist polarisation

The anisotropic films are interesting candidates for applications acting on polarised waves. In the previous section, we saw how to preferentially absorb polarised microwaves. The same elements are now used for another application: switching the angle of polarisation. This consists in polarising any wave crossing the multilayer. The first layer has nanofillers oriented along the z-axis, for example. Layer by layer, the composite films are a few degrees rotated until being aligned in y. Let's assume that an unpolarised wave comes in at port 1 (see Fig. 56), the electric field will progressively align along y. If the incoming wave is already polarised along y, the interaction with the multilayer will be weak so that no rotation will be operated. In short, the polariser imposes an orientation of the electric field without significant absorption.

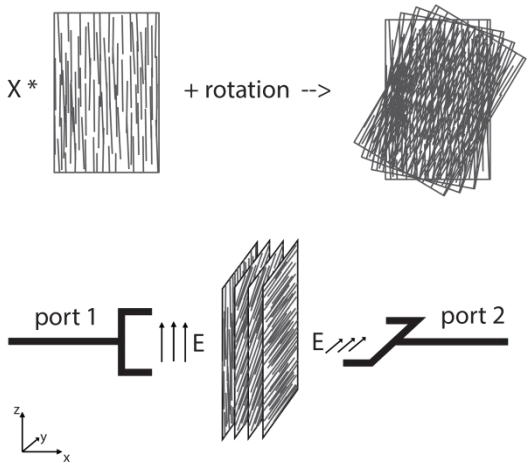


Fig. 56. scheme of the polariser multilayer and the orientation of the ports for EM characterisation.

The set-up is modified for this particular characterisation. The port 1 emits/measures waves polarised along the z-axis perpendicularly to the polarisation of reception/emission of the port 2. This is the reference which we compare the effect of samples with. It means that almost nothing is transmitted without the help of a polariser. The reflexion is total for the same reason. This blank measurement is first compared with a polariser built from an oriented CNT composites multilayer. Multilayers made from parallel CNT line patterns do not show convincing polarisation (not shown). This is probably due to the fact that

anisotropy of CNT lines is only fully effective when several patterned films are superimposed. Polarisation is more efficient when using oriented CNT composite films at the same total thickness. This point is significant because the more the thickness increases, the more the absorption increases too. Absorption is a drawback for polarisers. Fig. 57 gives the S-parameters of a polariser based on 3 CNT oriented films. Each layer is 125µm thick and 45° rotated to make a total angle of 90° from the incoming electric field. The second multilayer is built with 5 CNT oriented films. The incremental rotation is then 22.5° from layer to layer. Fig. 57 shows that the polariser is more efficient if we use more layers. S-parameters of the 5 layers system demonstrate that the transmission through the sample is enhanced.

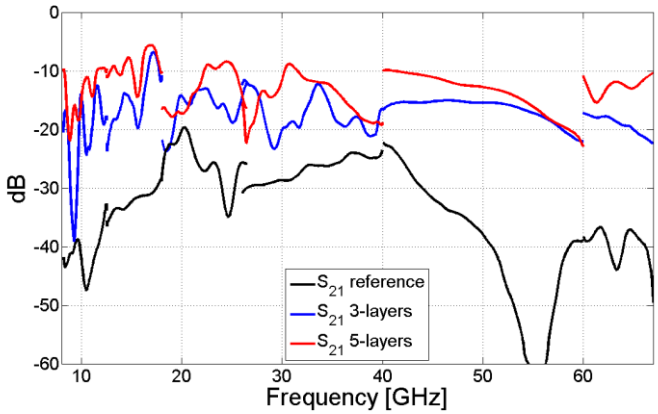


Fig. 57. S-parameters of multilayer polariser based on CNT oriented composite. The reference is the measurement of perpendicular waveguide only. The 3-layer and 5-layer polariser are a stack of CNT oriented composite with incremental angle of respectively 45° and 22.5° each.

The system is obviously perfectible. The major improvement would lie in the enhancement of the transmission. Comsol simulations have been performed to provide guidance toward a better structure. We have explored the impact of conductivity in one direction from 1 to 20S/m. Conductivity in other directions is fixed at 10^{-5}S/m and the thickness of all films is 25µm. Fig. 58a proves that increasing conductivity enhances the transmission for 3-layers polarisers. In Fig. 58b, we start from the 3-layers polariser with $\sigma = 20S/m$. This is compared with structures where the number of stacked layer increases (at same conductivity). We quickly conclude that it is advantageous to stack layers maximising conductivity

(in only one direction) and to multiply the number of those successive layers.

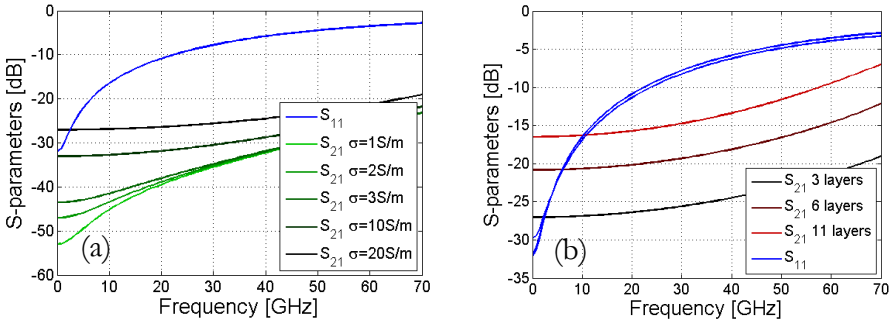


Fig. 58. Comsol simulations of several polarising structures. In (a), only conductivity changes and structural arrangement is fixed. In (b), the number of equivalent layer varies.

The present system could hence be optimised by using thinner films with higher CNT concentration and extremely high anisotropy. Again an enhancement of the stretching process should provide better alignment and, moreover thinner films which are advantageous for decreasing the loss.

3.4. Conclusion

The organisation of multilayer films in gradient of conductivity is a smart arrangement for absorption. The building blocks, namely the CNT composites, can be made anisotropic to add a novel property: polarisation sensitivity. Based on this idea, we have developed a multilayer having an absorption index depending on the polarisation of the incident microwave.

The interaction of anisotropic films with polarised waves can further be used to polarize an incident wave through the multilayer. From layer to layer, we force the electric field of the wave to rotate up to a defined angle. The system controls the wave propagation from a new point of view; the absorption becomes now a drawback because the objective is to modify the propagation mode of the wave without loss. We see here that polymer-CNT structures are adapted for numerous applications concerning the control of wave propagation.

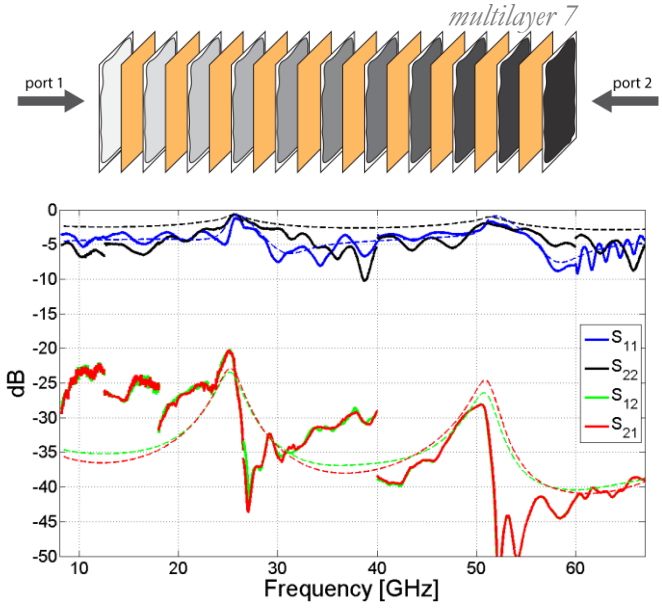
4. Electromagnetic bandgap structures

Carbon nanotubes or nanowires combined with polymer have shown their efficiency for broadband absorption. We go now further with a filtering system based on CNT and polymer or ceramic substrate. Two opposite behaviours are possible for the electromagnetic bandgap (EBG) filters using conductive layers. The first kind of filter can absorb almost the entire spectrum with the exception of narrow bandgaps at some frequencies: large bands of high absorption are separated by narrow bands showing weak absorption. The complementary structure, which is described further, is a filter selectively absorbing one frequency (and its harmonics). We adapt the structure so as to create some narrow windows/gaps in the spectrum where absorption increases. The high-absorption frequency bands correspond to a lower level of signal reflection.

4.1. Frequency-selective filter with narrow bandgap

In the previous section, PC was chosen for its low permittivity ($\varepsilon_r = 2.8$) in order to minimise the overall thickness of the absorber. However this low permittivity advantage of PC for a broadband absorber becomes a weakness for an EBG filter. A multilayer based on PC would require a very high thickness to achieve minima of absorption in the desired frequency range. Hence, PC is replaced by a high permittivity insulating substrate: Arlon AD1000 based on PTFE, ceramic powder and woven glass, with permittivity 10.7 and 1.5mm thickness. All morphological characteristics of the *multilayer 7* are given in Annex C. In EBG filters, the conductive layers serve as "mirrors" which trap waves

by multiple internal reflections. Ink based sandwiches are ideal for building the EBG. Fig. 59 presents the EM characterisation of an AquaCyl™ on PC - Arlon multilayer stacked in gradient of conductivity. The components are identical to those presented in the previous section except for the nature of dielectric layers. Fig. 59 gives measured S-parameters and calculated absorption of the ink based multilayer. As predicted by the simulations, the reflection S_{11} is maximum at ~26 GHz and its harmonics. The mean absorption level reaches 70% overall. The whole device has a thickness of 17.97mm mainly due to the relatively thick dielectric spacers. However, the multilayer flexibility remains reasonable for practical applications in the field of absorbers, while its mechanical and chemical resistance make it an interesting candidate for frequency-selective coating on the reflector of an antenna for pre-filtering of detected signals.



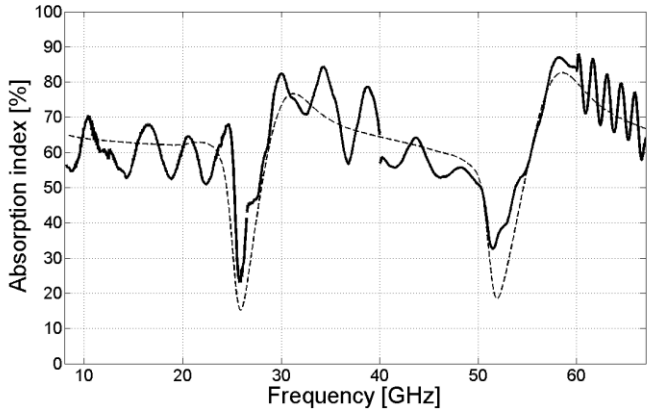


Fig. 59. measured S-parameters and absorption from port 1 to 2 (see inset) of an AquaCyl™ based composite gradient multilayer, the thickness of the dielectric ($\boldsymbol{\varepsilon} = \mathbf{10.7}$) is 1.5mm. Measurements (full lines) are fitted with simulations (dotted lines).

4.2. Frequency-selective filter with absorbing peak

For the following experiments, we aim at full absorption around 2.4GHz, corresponding to Wi-Fi communication systems (standard IEEE 802.11b to 802.11v), as an illustrative example of the concept. Theoretical analysis shows that a modification of dielectric spacer parameters (dielectric constant, thickness) shifts the position of the absorption minima (18). Substrates for PCBs can have a permittivity of up to 10 and even more (166). They are reliable candidates with well tabulated dielectric properties. Arlon AD1000 is an ideal candidate but very expensive, and its large scale use is questionable. Ceramics such as granite or concrete are natural materials also showing high dielectric ε-values. Although they lack the conformability of polymeric substrates, they are certainly relevant for applications focusing on building protection (167). So, we propose to compare selective absorbers built from polymeric Arlon high-ε substrates or from granite plates alternating with CNT-coated PC films described above. The nominal permittivity value of Arlon is equal to 10.7. Measurements of the granite slab give a permittivity of about 9 in the GHz range. As explained in section III-1.3, the condition for a local maximum of absorption at a given frequency is to have a quarter-wavelength distance between the conductive layers. Preliminary simulations have showed that the absorption peak is optimum (highest magnitude/width ratio) for conductive layers between

5.10^3 and 10^4S/m. With three AquaCyl™ airbrushed layers on plasma-activated PC films, it is possible to reach the required conductivity. As CNT coated films are sandwiched between thin PC sheets, the overall equivalent conductive layer thickness is 110µm. The thinnest arrangement able to absorb a selected frequency is a dielectric/conductor bilayer. For illustrating this filter, we use one 9.6mm thick Arlon substrate stacked against a single CNT-PC film. This simplest structure proves the efficiency of the basic cell and offers the advantage of a low thickness. The bilayer is 9.7mm thick, and the absorption peak appears at 2.4GHz or a wavelength of 125mm in vacuum. Referring to inset of Fig. 60 (and *multilayer 8* in Annex C), we see that when the incoming wave enters at port 1, it first meets the dielectric layer causing controlled reflection depending on the wavelength. The conductive layer acts mainly as a "mirror" creating the filtering effect at $t_{sub}=\lambda/4$. On the contrary, a wave incoming at port 2 is reflected regardless the frequency. Fig. 60 shows the agreement between measurements (solid curve) and the theoretical prediction (dotted curve).

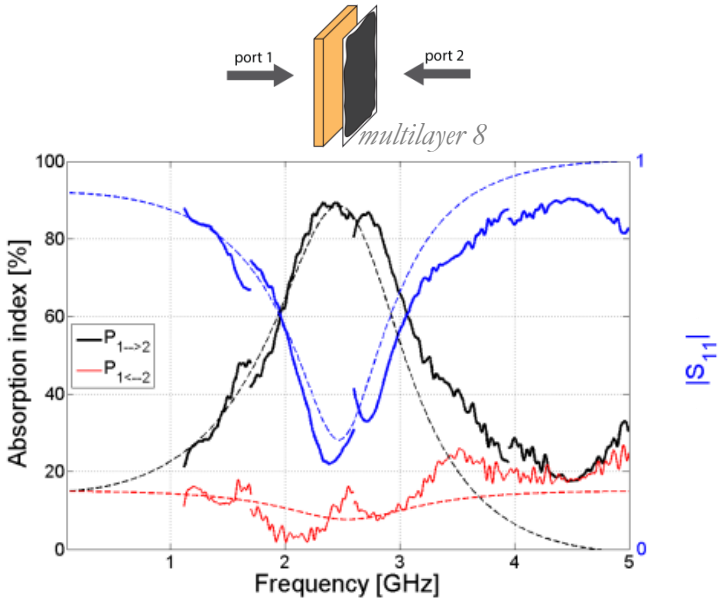


Fig. 60. EM characterisation of Arlon AD1000 substrate (orange thick layer in the inset) back-coated by a PC-CNT sandwich (black layer). The black and red curves are absorption in the direction given by legend. The magnitude of the S_{11} parameter is in blue. The analytical model predictions are displayed as dotted lines. (168)

As complementary structure to a single basic cell, we next characterise a multilayer of 3 granite slabs 10.45mm thick each separated by 2 CNT/PC layers (Fig. 61). For this step, we modify the nature and the number of the dielectric layers (see *multilayer 9* in Annex C). Still guided by preliminary simulations, we select 3 dielectric spacers in order to maximise the absorption peak in both direction while keeping an acceptable thickness. The filter now operates symmetrically in both directions and the maximum of absorption is also slightly higher than for the 1-granite layer filter (*multilayer 10*) shown for comparison. Changing the nature of spacers to granite also highlights the ability of this building material. The absorption curve of the 3-granite slabs multilayer shows an almost complete absorption at 2.4GHz but much lower absorption at other frequencies (simulation predicts an absorption of 25% at the mobile phones network frequency at 800MHz).

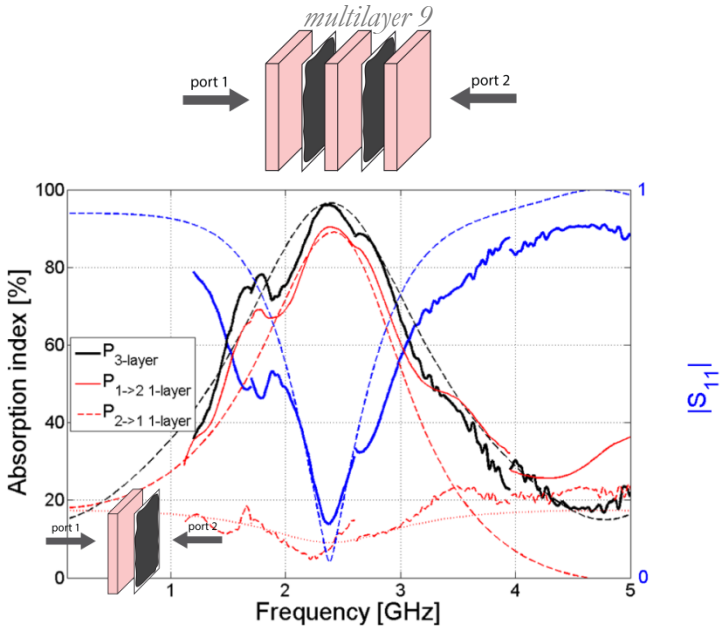


Fig. 61. EM characterisation of 2 thin CNT films sandwiched (black layers in the inset) between 3 granite slabs (pink slabs). The black curve is the absorption index and the blue curve is the magnitude of the S_{11} parameter. The red curves display for comparison the corresponding absorption level for a 1-granit slab filter. The analytical model predictions for the structure are displayed as dotted lines. (168)

The total thickness and weight of this second (with 3 granite slabs) filter are of course higher. We reach 31.55mm (and 1.54Kg) which is still

low compared to the wavelength (125mm at 2.4GHz). A photo of the two EBG filters is exhibited in Fig. 62 to visualise the structures.

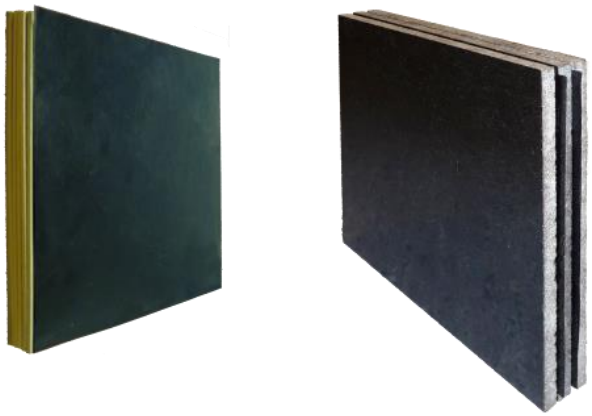


Fig. 62. Photo of the Arlon based EBG on the right and the granite based structure on the left. (168)

For other applications, a theoretical analysis of the multilayers demonstrates the possibility to tune the absorption frequency and bandwidth thanks to the versatility of the system. It is, for example, possible to decrease the thickness of the dielectric substrates if their permeability increases. It is in agreement with the *eq. III-9* and proven by simulations of such a multilayer. However, it requires developing a material with high ε'_r and μ'_r wich is incompatible with a dielectric material. Indeed, all natural magnetic substances or even magnetic composites are conductive.

The force of the EBG is the simplicity and the large scale manufacturability. The use of construction materials such as granite or concrete is interesting for their high performance in this application and their attractive cost.

4.3. Conclusion

We have demonstrated the easy to make thin (compared to wavelength) multilayer composite structures, which are able to selectively

absorb a desired frequency. They open up new possibilities in the area of microwave control using lossy EBG structures. The multilayers are based on widely available materials and nanofillers and have a modular structure, which endows them with great versatility and applicability. The analytical model developed to simulate the absorbers and filters is in good agreement with experimental characterisation and could be further extended to aid the design of new systems operating in other frequency ranges.

5. Cylindrical invisible cloaking

The final part of this thesis is focused on a cylindrical invisibility cloaking. We still work with polymer and CNT composites for the control of wave propagation. We present two gradient multilayer systems built from conductive-dielectric bilayers, one based on ABS and the other on Rohacell®, designed to deflect waves around an object with a loss as limited as possible. The judicious arrangement of the successive bilayers is the key to control the permittivity and thereby deflect waves in the wanted way. The cloaking is measured by near field mappings around the structure. The discussion of results and some directions to optimise the system are afterwards introduced.

5.1. Bilayers for controlled permittivity

The realisation of invisible cloaking involves the use of metamaterials with specific EM properties. The required ε_r must vary between 0 and 1 which is not obtainable with common polymers and composites. We have hence developed polymer-composite bilayers (an example is given in Fig. 63) for which ε_r goes down to below 1 and even to negative values (see section III-2.4). The strategy to make an object invisible is based on a series of concentric layers with controlled permittivity (see Fig. 26). From layer to layer, ε_r permittivity follows the rule of EM deviation formulated in section III-2.2. The magnetic permeability is 1

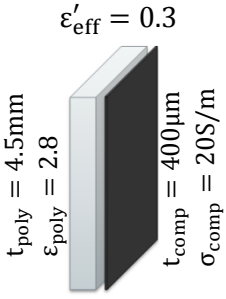


Fig. 63. diagram of a bilayer

and the imposed radial permittivity ε_θ is a constant dependent on the inner and outer radii of the structure (see *eq. III-54*). The inner radius is imposed at 3cm which means that the diameter of the cloaked object is higher than the wavelength, knowing that we work at 6GHz ($\lambda = 5\text{cm}$). The outer radius could be selected to give a perfect fit between actual ε_θ and theory but it involves often a very large thickness for the cloak. For this reason, it is preferable to deviate from the ideal to keep reasonable thickness of the system. All the structural choices and their impact are discussed in details in section V-5.4.

ABS dielectric spacers

The most influencing parameters on effective permittivity of the bilayers are the thickness of the dielectric layer and the conductivity of the composite. The first kind of bilayers developed in this chapter is built from acrylonitrile butadiene styrene (ABS) dielectric layer and AquaCyl™ based composite. Why was polycarbonate replaced by ABS? The dielectric tubes must be machined or moulded with a very high accuracy. An imprecision of 100µm notably changes the effective permittivity. This leads us to select a machining method of very high accuracy. Hence, we turn to a 3D printing technique. This meets the mandatory accuracy and avoids long and expensive machining process. However it reduces the choice of polymer to ABS or PLA (polylactic acid). Actually, a simple adaption of the analytical model to the properties of ABS allows predicting the thickness of ABS needed to manage the effective permittivity of each bilayer. The density of a 3D printed part is depending on printing mesh. We use the finest mesh to minimise changes of permittivity due to humidity of the air potentially diffusing into the pores of the printed part. The characterisation of ABS gives $\varepsilon_{ABS} = 3.1$ at 6GHz (which is higher than DC values given in the data sheet).

Hence, permittivity of the dielectric spacers is known. For ease, we decide to impose the thickness and conductivity of the composite layers in order to keep only one free parameter: the thickness of ABS dielectric layers. The thickness of the composite is preferably low ($t_{comp} = 175\mu\text{m}$) to avoid unwanted absorption through this film. This favours the choice of AquaCyl™ on PC film because of low thickness, ease of handling flexibility. Conductivity of the conductive films must be as low as possible to avoid reflecting a part of the EM waves. Fig. 64 shows an

analytical simulation of effective permittivity at 6GHz of a bilayer as a function of thickness of the dielectric layer and conductivity of the conductive layer. The graph is useful to determine the minimal conductivity acceptable so that ε_{eff} goes between 0 and 1. Here the limit is $\sigma_{comp} = 39S/m$ to reach the lower boundary $\varepsilon_{eff} = 0$. We consider the effective conductivity of the AquaCyl™ PC sandwich. This simplifies simulation and understanding. In short, we directly extract conductivity from measurements of the composite and we use it as input for the simulations of bilayers.

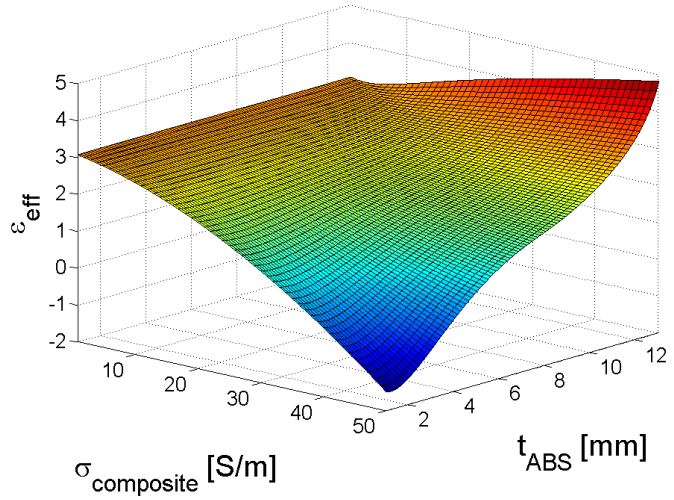


Fig. 64. simulation of effective permittivity at 6GHz of a bilayer as function of thickness of ABS layer and conductivity of conductive layer. The composite is 175µm thick and $\varepsilon_{ABS} = 3.1$. The effective permittivity must at least cross 0 and 1 for a fixed conductivity of the composite.

Prediction of Fig. 64 condenses a lot of information. It confirms the possibility of creating an effective permittivity lower than 1 by stacking two films of very different conductivity. When σ_{comp} tends to 0, ε'_{eff} is close to the law of mixtures (very close to ε_{ABS} due to the difference in thickness). On the other hand, the higher the conductivity of the composite, the lower is the effective permittivity. This highlights by the way that any inaccuracy on σ_{comp} could significantly change ε'_{eff}. That is why all composites are first characterised in order to qualify them. Their thickness could also alter quality but the process to make CNT sandwiches is very accurate in terms of thickness. When conductivity of

a composite is fixed, the thickness of ABS controls the effective permittivity of the bilayer. A last point of concern is the stability of the dielectric constant of the ABS spacer with respect to ambient conditions. Fig. 65 shows the influence of a change of ε_{ABS} or the thickness of the composite on ε'_{eff} of the bilayer. We note that a change of t_{comp} has a very weak impact on ε_{eff} since its standard deviation is 7µm (for an average of 175µm). The change of permittivity of ABS is more problematic. The range displayed on Fig. 65 is too wide but small changes of ABS permittivity do have a potentially significant impact. To avoid this issue, the samples are stored and all EM measurements are performed in the Welcome laboratory of UCL where temperature and humidity are regulated. No significant deviation has been observed during a few months of study.

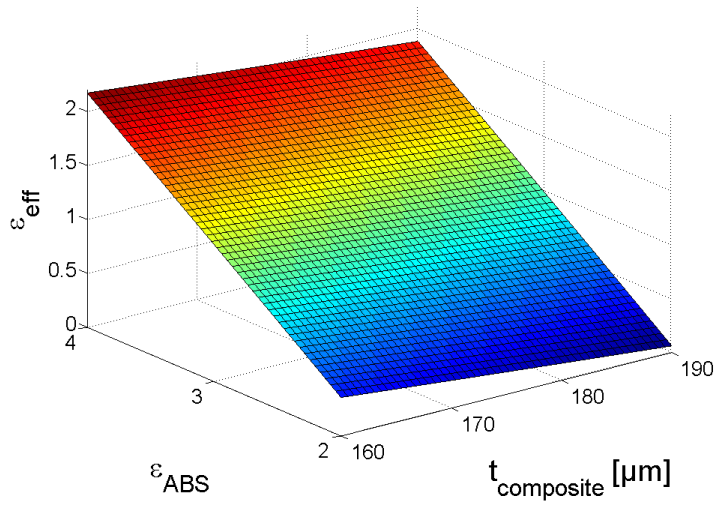


Fig. 65. influence of change of permittivity of ABS and change of thickness of the composite on effective permittivity of the bilayer. The ABS layer is 5mm thick and the conductivity of the composite is fixed at 35S/m.

Some bilayers have been measured by wave guide in order to confirm the expectation. For the examples of Fig. 66, three slabs of ABS (3.9, 4.1 and 4.6mm thick) are characterised with back covered conductive layer. The composite is plasma modified polycarbonate dip coated in pure AquaCyl™ (AquaCyl™ is adhering only to activated surface of PC) and hot pressed with a second PC sheet to protect the CNT deposit. Its effective conductivity is 35S/m at 6GHz (with a

standard deviation lower than 1S/m) and the thickness is 175µm. The ABS-CNT sandwich bilayers have an effective permittivity from 0.8 to 1.7 (full lines of Fig. 66). As expected, those results are slightly above the interesting range. The study (in Fig. 64) of the interaction between composite conductivity and effective permittivity of the bilayer shows that σ_{comp} has to increase to decrease ε'_{eff}. For ease, we stack 2 composite layers on the same ABS slabs in order to increase the reflectivity and hence decrease the effective permittivity. Those results are displayed in Fig. 66 by the dotted curve (called …|2xCNT in the legend). Let's note also that effective conductivity is relatively low due to the much larger thickness of ABS than of the composite. By the way, the difference between the effective conductivity of single and double layer composites is not very significant, as opposed to the strong influence on permittivity.

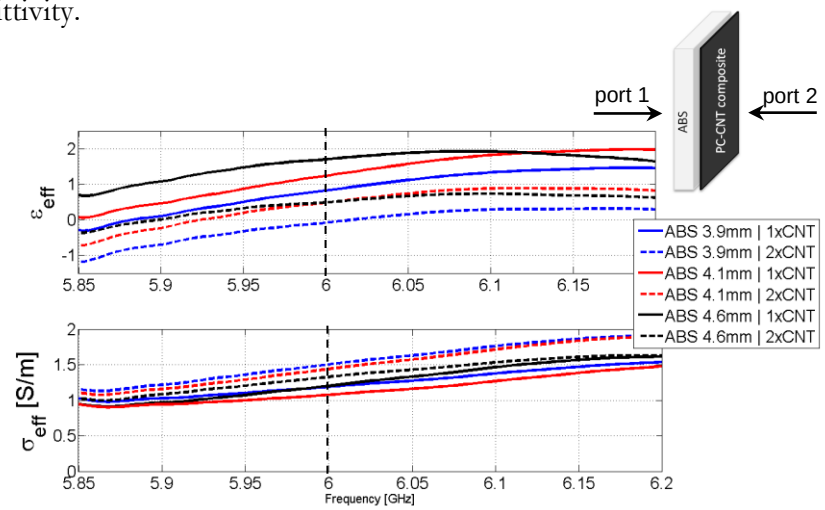


Fig. 66. Effective permittivity and conductivity of ABS-CNT composite bilayers. The thicknesses of ABS are 3.9, 4.1 and 4.6mm. The conductive layer is 1 or 2 AquaCyl™ based film(s) which is/are stacked on the back.

Rohacell® dielectric spacers

In parallel with ABS printing, we have developed spacers in Rohacell® foam. This foam exhibits properties similar to air at microwave frequencies. Rohacell® is very stable in terms of frequency and external conditions. Temperature does not affect its permittivity and its structure is made of closed cells which makes it insensitive to changes of ambient humidity. The drawback is the difficulty to machine precise

parts. This is why we obtained the help of the company Grando specialised in high accuracy foam cutting by high pressure water. The accuracy is similar to the one of 3D printing.

A study of the relationship between conductivity of the composite, thickness of Rohacell® and effective permittivity of the bilayer is first performed. Fig. 67 shows that we need even less conductivity of the composite (as compared with printed ABS) mainly because Rohacell® has a low intrinsic dielectric constant. A zero effective permittivity is already reached with $\sigma_{comp} = 21S/m$. This advantage is accompanied by a drawback: ε'_{eff} is very sensitive to σ_{comp}.

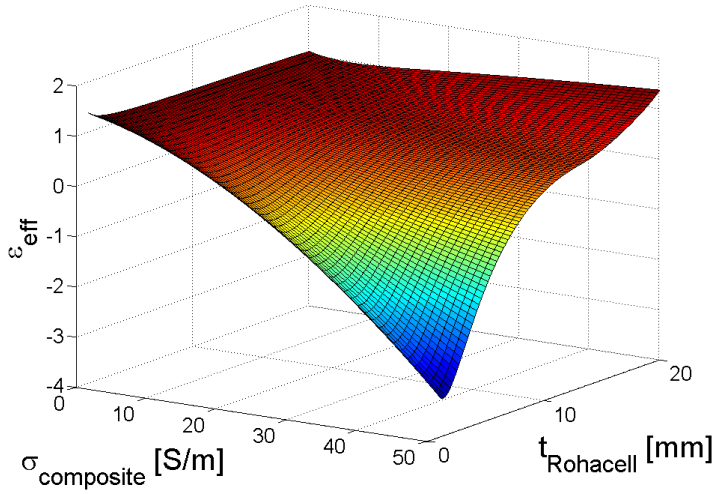


Fig. 67. simulation of effective permittivity at 6GHz of a bilayer in function of thickness of Rohacell® layer and conductivity of conductive layer. The composite is 175µm thick and $\varepsilon_{Rohacell} = 1.106$. Effective permittivity must at least cross 0 and 1 for a chosen conductivity of composite.

Rohacell®-composite bilayers are measured at 5, 10, 15 and 20mm of Rohacell® thickness. Referring to Fig. 67, we see that lower conductivities are needed than in the case of printed ABS slabs. With Rohacell®, we use CNT sandwiched films (based on PC dip coated in 60% diluted AquaCyl™) with $\sigma_{comp} = 24S/m$ and thickness 175µm.

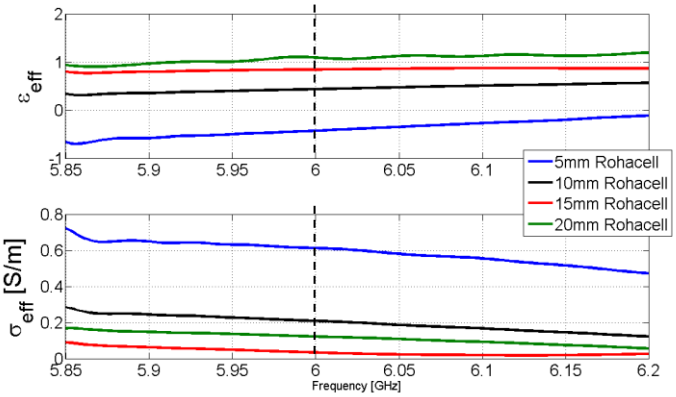


Fig. 68. Effective permittivity and conductivity of Rohacell®-CNT composite bilayers. The thicknesses of Rohacell® are 5, 10, 15 and 20mm. The AquaCyl™ based film has $\sigma_{comp} = 24 S/m$.

5.2. Stacks of bilayers for the invisibility cloak

The targeted invisible cloak is built with the help of the formalism for a cylindrical shape (see section III-2.2). We aim to make any object invisible by controlling radial permittivity of a multi-layered structure. Preliminary simulations are performed in order to determine the best parameters and identify their influence on the cloaking. The basic simulation is a top view of point-source (located on the left side) emitting a wave at 6GHz into a free space (see Fig. 69a). Fig. 69b shows the wave propagation from the source to a cylinder made of copper. This is the reference. We see a cone-shaped shadow behind the cylinder, the magnitude of the EM wave slightly decreases and the phase is shifted. The objective is thus to reduce this area. Fig. 69c shows the same cylinder surrounded by an ideal cloak of invisibility. The cloaking perfectly applies the *eq. III-54* knowing that the antenna emits a y-polarised wave at 6GHz. The comparison between Fig. 69a and Fig. 69c is the evidence of proper operation. The theoretical cloak involves no loss since it works only with the real part of ε_r and μ_r (the imaginary part is set to 0). Still referring to *eq. III-54*, $\mu = 1$ all over the device, $\varepsilon_r = 1$ on the outer radius of the cloak but $\varepsilon_\theta = \left(\frac{b}{b-a}\right)^2$ where a and b are the inner and outer radius respectively. When the characteristic impedance Z_c of the cloak is well adapted, it is impossible to get no reflection since Z_c does not match with the normalised impedance of the air namely

$Z_{air} = 1$. The consequence is a slight reflection along $\hat{e}_\theta$. This becomes negligible when a decreases or b increases. We chose the compromise: $a = 30mm$ and $b = 60mm$.

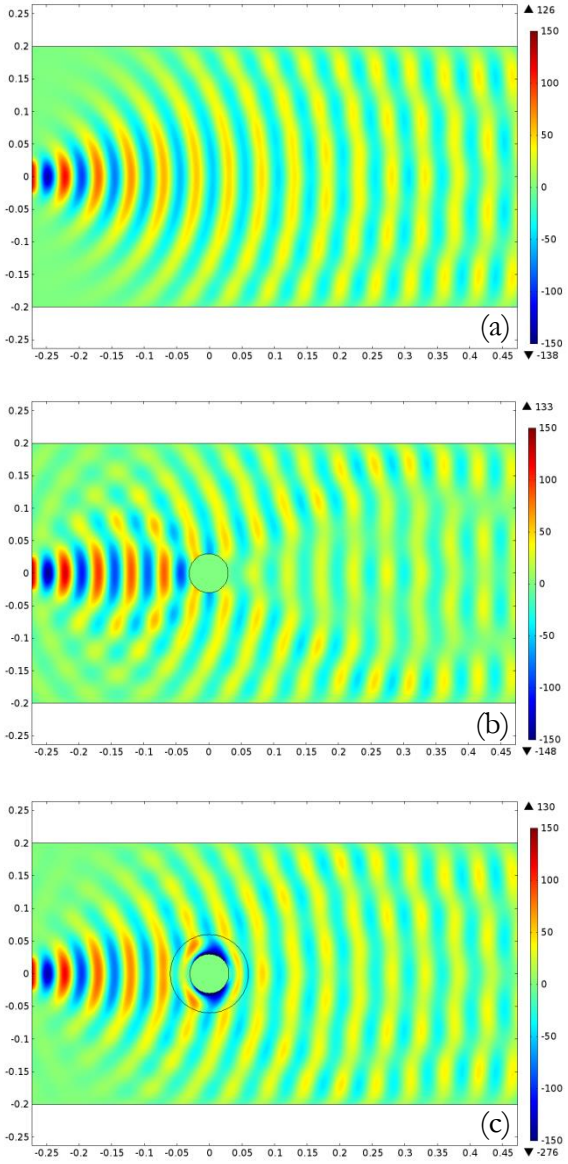
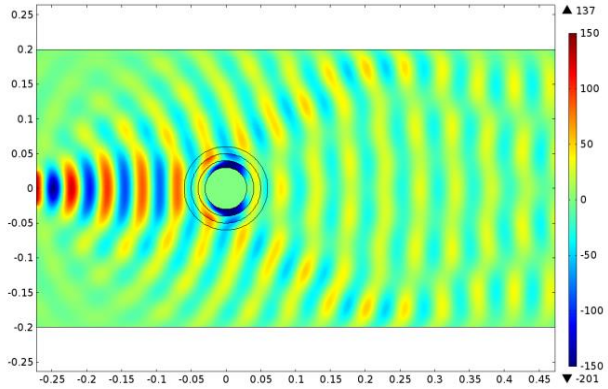
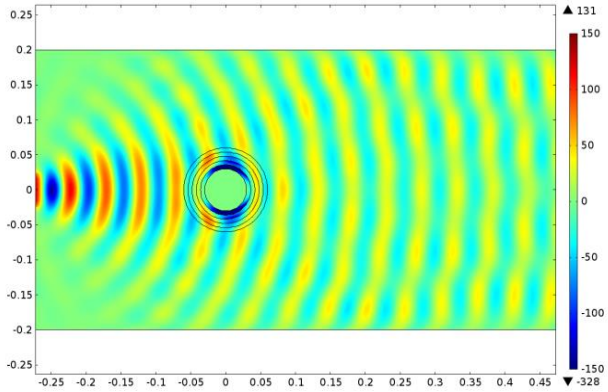


Fig. 69. Comsol simulations of the wave propagation over a free space in (a), around a metallic cylinder (30mm radius) in (b) and the same cylinder covered by a perfect invisible cloaking 30mm thick in (c)

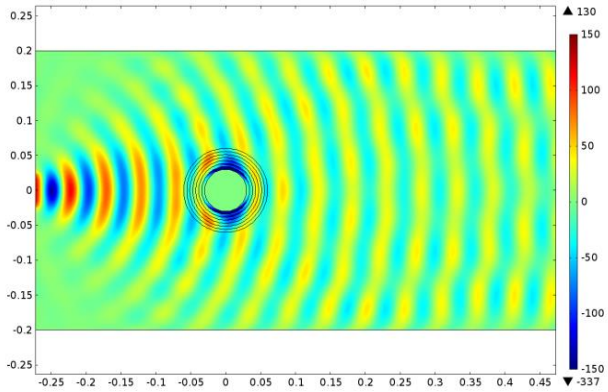
The device presented in Fig. 69 is a theoretical material whose physical properties progressively change with spatial coordinate. For practical realisation, the block is divided into concentric cylindrical layers having constant physical properties. The question then arises how many layers are, at the minimum, mandatory to keep an effect close to the continuous medium system. Fig. 70 shows the reference structure divided into 3, 5 and 7 layers. Each of these layers obviously follows conditions: $\mu_z = 1$ and $\varepsilon_\theta = 4$ (here); as for ε_r, it is a constant value per layer fixed by its position in the stack. For instance, the 5-layered cloak is composed of layers having ε_r equal to 0.033, 0.213, 0.444, 0.678 and 0.898 from inner to outer layer. The simulations of Fig. 70 show that the 3-layered cloak degrades the quality of the response. The 5- and 7-layered cloaks are quasi similar and they are very close to the continuous medium cloak (in Fig. 69b). This proves that a division beyond 5 layers is unbeneficial. This result is useful for next investigations.



divided in
3 layers



divided in
5 layers

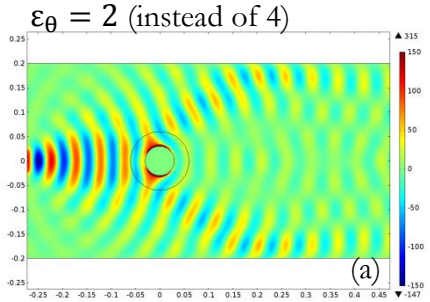


divided in
7 layers

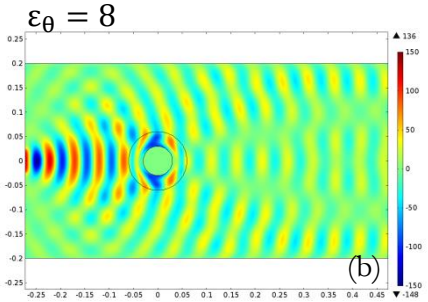
Fig. 70. Comparison between different layered cloaks of invisibility. The structure is divided in 3, 5 and 7 layers which have constant physical properties.

The strategy of cloaking by bilayers requires sequencing the device in layers. The brief analysis here above has shown that it is not necessary to work with a continuous medium and that even a rough division is sufficient to reconstruct the incoming wave front to the back of the device. The number of bilayers might be determined in order to satisfy the condition $\varepsilon_\theta = \left(\frac{b}{b-a}\right)^2$. In other words, we could add more and more bilayers to increase the radius b up to the point we get an agreement with ε_θ. Nevertheless, the non-zero conductivity used to control the effective permittivity induces a reflection and loss. It is therefore necessary to limit the number of bilayers to reduce the total reflectivity of the system. This is why it is essential to restrain as much as possible the number of bilayers. The following simulations sum up the impact of the deviation from strict theory. Fig. 71a and Fig. 71b show the cloaking quality when ε_θ is respectively 50% and 200% of the ideal value. We observe that the deviation impacts the overlapping of the wave behind the object. Fig. 71c and Fig. 71d show the influence of a lossy cloaking device with σ equals to 1 and 10S/m respectively.

$\varepsilon_\theta = 2$ (instead of 4)



$\varepsilon_\theta = 8$



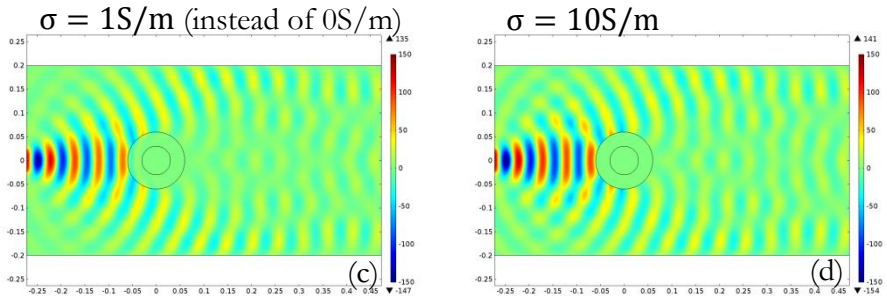


Fig. 71. simulations of invisible cloaking showing the influence of deviation from the ideal case. In (a) and (b), ε_θ is 50 and 200% the right value respectively. In (c) and (d), conductivity is 1 and 10S/m respectively.

So the realisation of cloaking is a matter of compromise to come as close as possible to the ideal case. In practice, two invisible cloaks made from bilayers have been realised. The first uses ABS as dielectric layers made by 3D printing. It has the advantage of being relatively compact but it requires more conductive composite which inevitably implies a greater loss. The thickness of the cloak is only 21.1mm, therefore $\varepsilon_\theta = 5.87$. The real azimuthal permittivity is more or less the one of ABS i.e. 3.1. The simulation built with experimental properties of each independent element is displayed in Fig. 72.

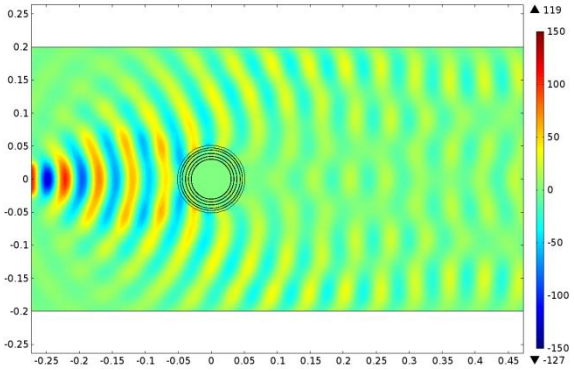


Fig. 72. simulation of the invisible cloaking based from ABS-composite bilayers

Loss and mismatch of ε_θ deteriorate the quality of the reconstruction of the wavefront. For the reasons stated above, it does not seem possible to significantly increase the efficiency of the ABS-

composite couple. A second alternative has been developed as an attempt to solve the problem of losses. ABS is replaced by Rohacell® foam. The very low permittivity of this material allows reaching zero-permittivity with the help of a weakly conductive composite. The disadvantage is that it generates a much wider invisible cloaking. The stack of 5 Rohacell®-composite bilayers simulated in Fig. 73 has a thickness of 49.7mm. The ratio of the inner/outer radii is greater, the azimuthal permittivity is thus lowered to $\varepsilon_\theta = 2.57$. But it remains higher than the intrinsic permittivity of Rohacell® 1.106. This issue point could be eliminated but it would involve a huge device. So we decide to keep those two examples as demonstrators. Several enhancements are suggested in section V-5.4.

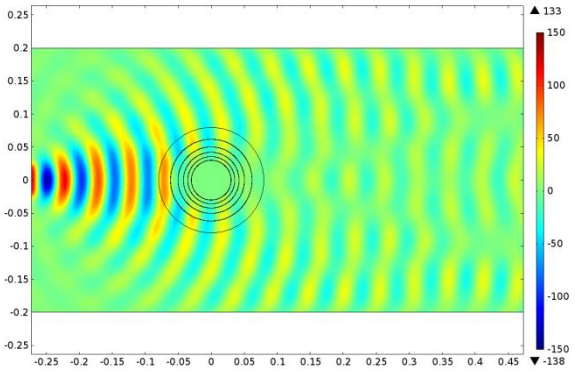


Fig. 73. simulation of invisible cloaking based on Rohacell®-composite bilayers

5.3. Mapping of near field around cloaked zone

The cloaking devices have been characterised by a near field probe in space. The antenna emits a y-polarised wave at 6GHz toward the xy table. Port 1 of the PNAX-70 is connected to the antenna and the probe is connected to port 2. We measure thus S_{21} that corresponds to the near field measurements. The cylindrical cloak stands (in z-axis) on the middle of the table and the probe moves around halfway up the cylinder. The practical details and illustrations of the measurements are given in section IV-3.3. The probe sweeps a maximum surface of 250x250mm. In order to extend the surface, two mappings are taken side by side in the front and behind the device. The captures are assembled and displayed by Matlab. The real part of S_{21} is multiplied by the cosine of the phase angle. This gives a view of the magnitude and the phase of the wave at all points.

Near field mapping around a reference steel cylinder

The first mapping of the near field has been performed on a single metallic cylinder. This is the reference that we aim to make invisible (Fig. 74). It consists of a steel cylinder with 6cm height and diameter (which is larger than the wavelength). The cylinder is placed on a Rohacell® plate (itself on top of high absorbing foam) to avoid any interferences with the table. It appears like a levitating cylinder for microwaves. The probe sweeps the surface but the zone around the arm fixture is inaccessible. The unmeasurable area is displayed in white on the graphs. A scheme of the cylinder is added over the graph for a better visualisation.

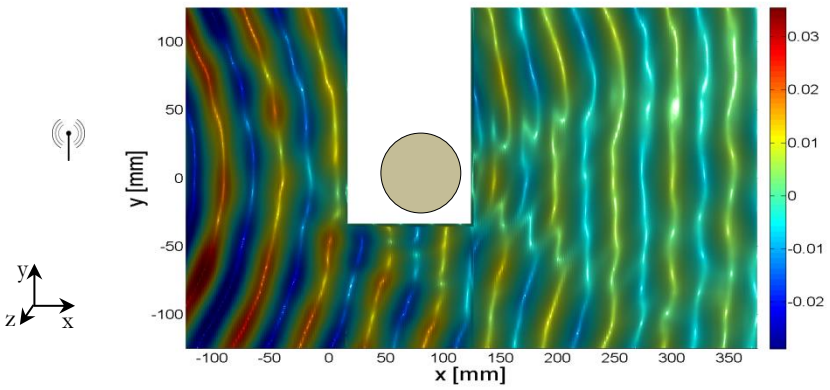


Fig. 74. characterisation of a metallic cylinder over the xy table

Near field mapping around an invisible cloaking based on ABS-CNT composites bilayers

The cylinder of Fig. 74 is now covered by a cloak based on 5 ABS-composite bilayers. Each bilayer is composed of an ABS hollow cylinder produced by a 3D printer which is coated by a sandwich of AquaCyl™ on PC. It is the structure described and simulated previously. Fig. 75 gives the result of the near field mapping. The cylinder and the cloak of invisibility are schematised by the grey and white circles respectively.

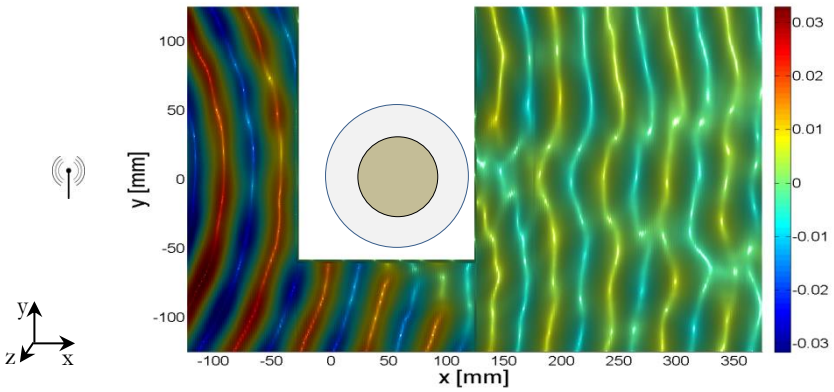


Fig. 75. characterisation of a metallic cylinder cloaked by a stack of 5 ABS-CNT composite bilayers

The invisibility cloak of Fig. 75 shows a significant influence on the incoming wavefront. Compared to Fig. 74, we see that the interference due to reflection at the front of the object is attenuated. The cloaking therefore promotes wave transmission beyond the object. However, it is not excluded that a minor part of this reflection was absorbed by the cloak itself. Behind the steel cylinder, we can observe a narrowing of the angle of the shadow. Deviations from the ideal case are thus seen in the way predicted by Comsol simulations (see Fig. 72). The real value of the azimuthal permittivity does not exactly match theory and hence a cone of shadow is still present at the back. This shadow is also amplified by the non-negligible level of loss of the invisibility cloak. Despite these weaknesses, the device does help the wavefront bypass the obstacle. The strategy of bilayers stacking hence proves its ability to modulate the effective permittivity of the medium and so control the path of a wave at a preset frequency. Various optimisation pathways are discussed in the next paragraph.

Near field mapping around an invisible cloaking based on Rohacell®-CNT composites bilayers

The near field has been swept around the invisible cloaking built on CNT composites and Rohacell® (see Fig. 76). The global conductivity of this system is lower than the previous one based on ABS. This is the advantage of this system which decreases the loss. The reconstruction of

wave front by the way is less oscillating. The wavefront behind the system lets appear a slight shadow which has a narrower angle than the case without cloaking (see Fig. 74). Unfortunately, the large outer radius of this invisible cloak reduces the measurement area on the left part. We did not collect enough data to draw reliable conclusion about the reflectivity.

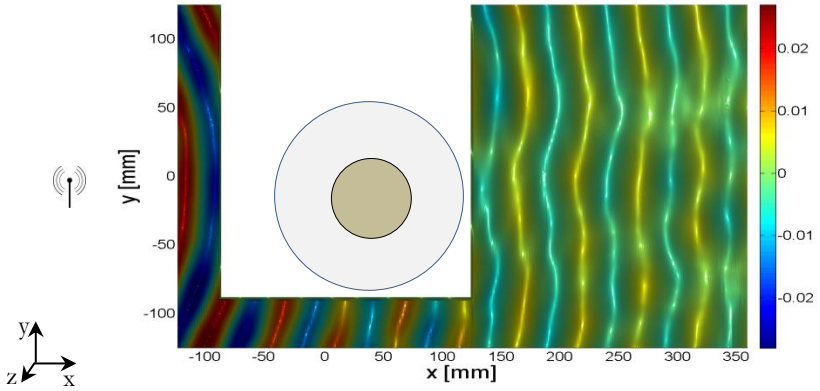


Fig. 76. characterisation of a metallic cylinder cloaked by a stack of 5 Rohacell®-CNT composite bilayers

A photo of the ABS and Rohacell® stacks used for invisible cloaking is shown in Fig. 77. The steel cylinder is placed at the centre of the structures for the near field mapping.



Fig. 77. photo of Rohacell® and ABS based invisible cloaking (and the steel cylinder)

5.4. Discussion of experimental results and potential enhancements

The analysis of our multilayer cylindrical cloaks shows an undeniable ability to deviate the microwaves. However we have to admit that the reconstruction of the wavefront behind the cloaked object is perfectible. The points limiting the performance are discussed below and some directions to mitigate them are given. The reflectivity of the cloak is probably a major problem, which could be eliminated by modifications of the CNT based composites. The mismatch of ε_θ is improvable by simple changes of the structure. Some complementary concepts are also described as prospects for future research starting from the present work.

Reducing EM loss

A perfect cloaking should be transparent. However, non-zero conductivity is required to deflect the microwaves to the desired trajectory. A study of the interaction between the conductivity of the composite and the effective permittivity of bilayers has already been carried out in order to work with lower conductivity. The nature of the dielectric is important at this stage; the lower its dielectric constant, the lower the conductivity of the composite required ensuring a minimum effective permittivity of 0.

Although it is not possible to reduce the overall conductivity by our method, it is interesting to quantify its influence. Fig. 78 compares an invisible cloaking based on Rohacell® bilayers (in a) with a hypothetical system where radial and azimuthal permittivities are equivalent but the global conductivity is zero. It proves that a drastic decrease of σ improves the transmission near the system but the reconstruction of the wavefront continues to be disrupted by the mismatch of ε_θ.

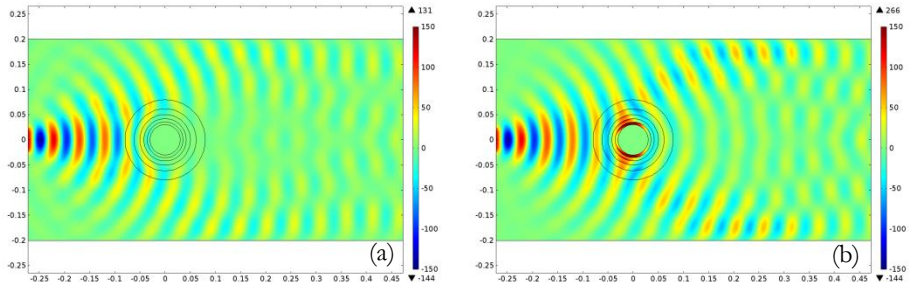


Fig. 78. Comsol simulations of wave propagation trough "normal" Rohacell® based invisible cloaking in (a) and the same system where σ is artificially set at 0S/m in (b).

Improvement of the azimuthal permittivity matching

Apart from the loss, the imperfection of the experimental cloaking is caused by the difference between the experimental azimuthal permittivity and its theoretical value. To correct this inaccuracy, we should use a material whose azimuthal permittivity ε_θ is larger than the radial permittivity ε_r. Indeed, ε_r is set so that each bilayer gives ε_{eff} satisfying the *eq. III-54*. Changing only ε_θ of the dielectric layers would effectively require an anisotropic material, for example, a polymer reinforced with oriented ceramic nanofibers having a high dielectric constant in the direction $\hat{e}_\theta$. The impact on ε_r would be minimal compared to the increase of ε_θ. The development of such material does not seem unfeasible, despite its higher complexity. The cloaking based on Rohacell® would require an extensive modification of the production process. On the other hand, the ABS based cloak of invisibility could be directly printed with a suited anisotropy. With the increasing popularity and fast development of 3D printing, it will soon be possible to print micro-architecturated anisotropic materials. The composite film could immediately be printed too. Fig. 86b shows a Comsol simulation of the structure so described (which is compared with the cloaking based on isotropic ABS in Fig. 86a). The dielectric layers have ε_r of bulk ABS but ε_θ is modified to fit with the *eq. III-54*.

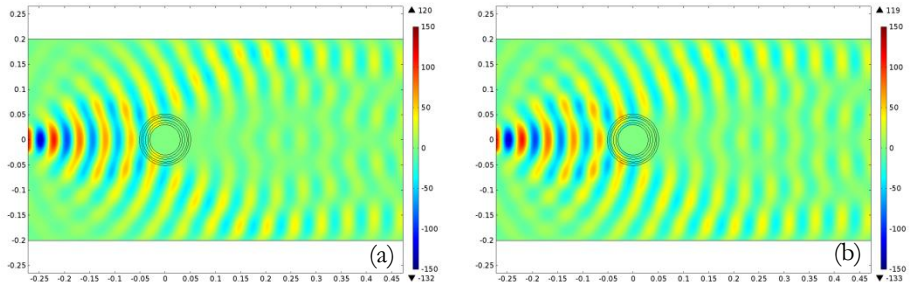


Fig. 79. Comsol simulations of wave propagation trough "normal" ABS based invisible cloaking in (a) and the same system where ε_θ fits with theory in (b).

Through this simulation, we notice that the correction of ε_θ produces an enhancement to restore the correct shape of the back wavefront. Research about the issue of azimuthal permittivity merits further consideration. It is conceivable that an optimisation in terms of loss reduction coupled with a better match with theoretical ε_θ would lead to effective systems. Some solutions to bypass the current limitations are introduced in next section.

5.5. Prospects and alternatives for invisible cloaking

Invisible cloaking by stacks of polymer-composite bilayers has shown its ability and its limitations. This point introduces potential avenues to develop complementary systems bypassing the current issues. The concept of cloaking by bilayers is extrapolated to magnetic composites stacked with the same dielectric polymer. The addition of magnetism allows managing permeability for deviating microwaves. It adds also the possibility to extend our cloaking to arbitrary shape in theory. The concept of split ring resonator designed by CNT ink is brought as a second alternative to control permeability with a thin and single layer. Afterwards, a variant of our cloaking is described. It is a swiss roll system built from a continuous bilayer rolled up on itself. The simplicity of its implementation combined with correct performance makes it a serious candidate for invisible cloaking.

Test of split ring resonators designed by CNT

The most common way to control permeability is the use of metallic split ring resonator (SSR). As explained in section III-2.3, the design of SRR with a conductive substance allows decreasing the effective permeability as a function of geometrical parameters of the patterns. Controlling permeability leads to advantages such as lower loss. We have performed some trials of airbrushing CNT trough of mask in order to draw SRR. The process is detailed in section IV-2.3. It provides structured films whose permeability is passing through desired values around radar frequencies. An example of the possibilities is shown in Fig. 80 which presents a simulation of a structure containing 2 superimposed SRR made of CNT. Referring to Fig. 22, the design is built with: r = 5.6mm, d = 3.1mm, g = 5.7mm, p = 3mm, a = 49.4mm, l = 300µm. A picture of a CNT SRR sandwiched between PC sheets is inset in Fig. 80.

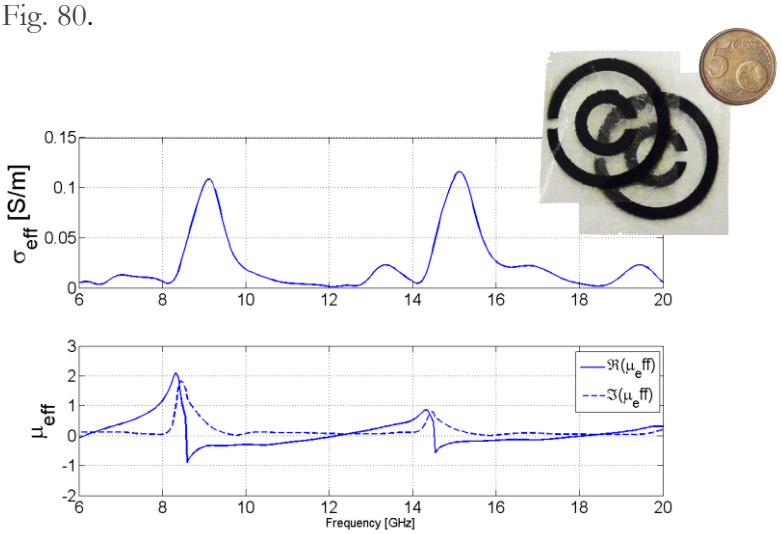


Fig. 80. effective conductivity and permeability of 2 superimposed SRR of CNT on PC. The inset is a picture of the measured 2 layers of SRR (superimposed for measurement).

The resonance involving the fluctuation of μ_{eff} has to appear at 6GHz in theory. The shift is presumably due to a lack of precision because of the airbrushing and the hot-pressing steps which do not bring a sufficient structural accuracy. A small deviation from the theoretical pattern implies large change on measured effective permeability. It is the reason why we have not further developed this method for cloaking.

Moreover, the imaginary permeability $\Im\{\mu_{eff}\}$ should be a narrow peak as shown by Fig. 22. The spreading of the peak is possibly also caused by a lack of precision of the pattern. However, we notice that the resonance phenomenon obviously shows up. Permeability crosses the values between 0 and 1, hence proving that this route could be used for an invisible cloaking system. The loss would be weak because the effective conductivity is weak as proven by Fig. 80. Assuming that a high precision SRR would sharpen the peak of μ''_{eff} as predicted by theory, the loss would be only due to non-zero conductivity. The structure would approach the Pendry's work (see Fig. 24) but would be fully composed of organic materials processed in simple ways.

Swiss roll cloak of invisibility

The swiss roll invisible cloaking is a variant of the presented systems which target an extremely simple implementation process. The bilayer concept is kept for the control of radial permittivity. Instead of stacking concentric tubular bilayers, a continuous film of dielectric-composite is wound around the object to cloak. The thickness of the dielectric layer has to grow continuously in the same way as the thickness of the dielectric bilayers increases from the inner to outer radius for concentric tubes. Fig. 81 shows schematically the envisioned manufacturing process. Note also that it would be possible to create this structure with a dielectric film of constant thickness if the conductivity of the composite varies along the length (as suggested by the Fig. 64 and Fig. 67). However, it seems simpler to manage a thickness gradient that a continuous conductivity gradient.

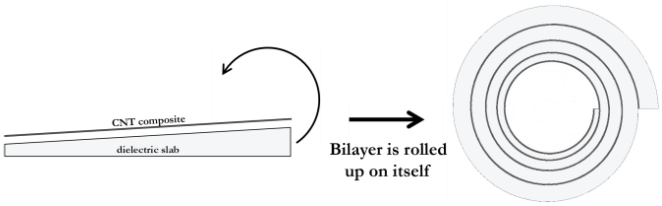


Fig. 81. diagram of the implementation of swiss roll invisible cloaking

Simulations have been conducted to show the ability of this variant of cloaking. The simulated composite remains identical to previous theoretical and experimental cases. The dielectric is simulated from the

physical parameters of Rohacell®. Its thickness increases linearly to be as close as possible to the aimed thickness in order to obtain the proper effective permittivity. Since this structure is not symmetrical, it has been simulated under different angles. The elementary structure is shown in Fig. 82a and next it is rotated -90° (Fig. 82b) and +90° (Fig. 82c).

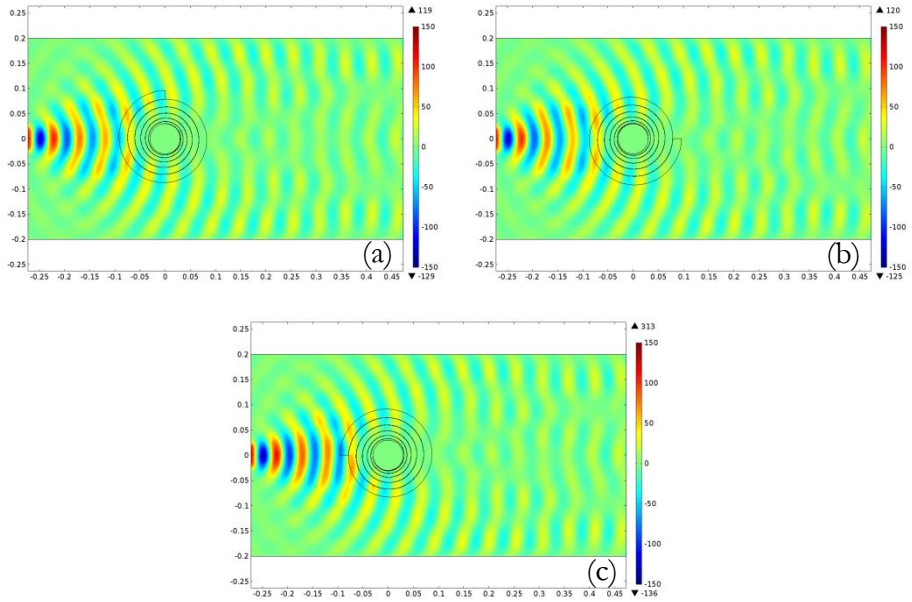


Fig. 82. simulations of swiss roll invisible cloaking with different rotation in order to observe any influence on wavefront and the quality of transmission

No significant difference is noted according to the angle of the structure. The angle of incident wave therefore has no negative impact on the quality of cloaking. The very simple implementation makes the "swiss roll" an attractive possibility.

5.6. Conclusion

Isotropic composites built from CNT and polymeric substrates can be organised as smart multilayers able to produce effective control of EMW propagation. The fine management of the physical properties of each individual layer is the key to deviate microwaves in wanted directions. This approach paves the way to invisible cloaking but in the present implementation, some loss is unavoidable due to the required

conductive layers. Some directions for improvement (SRR CNT paths, anisotropic dielectric layers, swiss roll structure) have been proposed.

The devices can be developed for radar applications if the cloaking quality is high enough to evade radar detection threshold. Even if the reconstruction of the wavefront behind the cloaked object is so far not perfect, the system could be made invisible for the detector.

In summary, carbon nanotubes combined with dielectric polymer are brilliant candidates for the control of wave propagation with the advantage of simplicity and robustness.

Chapter VI

General conclusion & prospects

The broad objective of this thesis is to contribute to the progress of the state the art in the important field of microwave EM control by absorption as well as deflection. The investigations have focused on wide band absorbers, frequency-selective absorbers and invisible cloaking. The strategy developed to fulfil the general aim is based on hierarchical multilayer structures using a combination of conductive nano-composites and pure polymer or ceramic substrates.

Carbon nanotubes (and partially nickel nanowires) composite films are the essential building blocks used in this work to create the layered structures. Some methods have been developed to homogeneously disperse nanofillers (CNT or NW) three-dimensionally or as a surface thin deposition to achieve the desired mechanical and EM properties. By adequate control of the process, this approach allows producing composite films whose conductivity, permittivity and permeability are controllable over a broad range, including their anisotropy. However, those basic layers only realise their full potential when they are stacked according to a smart organisation. The absorption or deviation of microwaves appears under particular conditions. For instance, we could make an EBG instead of a broadband absorber with the same layers if the arrangement is modified. It is therefore necessary to implement a mathematical model to stimulate multiple interactions between the set of layers used in a multilayer. This model, built on the concept of chain matrices, is able to predict the frequency dependent behaviour of all types of multilayers when geometry and electromagnetic properties of each individual layer are used as input. Despite its simplicity this model is nevertheless powerful. As evidence, it has been used to predict the structure of broadband absorbers, EBG filters and invisible cloaking which are successively discussed hereafter.

1. Broadband absorption

Absorption over the frequency range of 8-67GHz has been widely studied in this research. Multilayer structures alternating conductive and dielectric films are a great combination to maximise absorption. A stack of conductive layers in gradient of conductivity decreases the reflection. The developed structures are presented as flexible, thin and conformable films. The conductive layers are either made of a PC-CNT blended composite obtained by extrusion or an ultra-thin deposit of CNT on the polycarbonate surface. This last is a novel method for the production of

sandwiches of entangled CNT between PC sheets. It stands out from the current state of the art by its simplicity (169) and its performance in terms of conductivity (170). The achieved absorption index is entirely convincing especially since the overall thickness remains far below the wavelength as shown by Fig. 83.

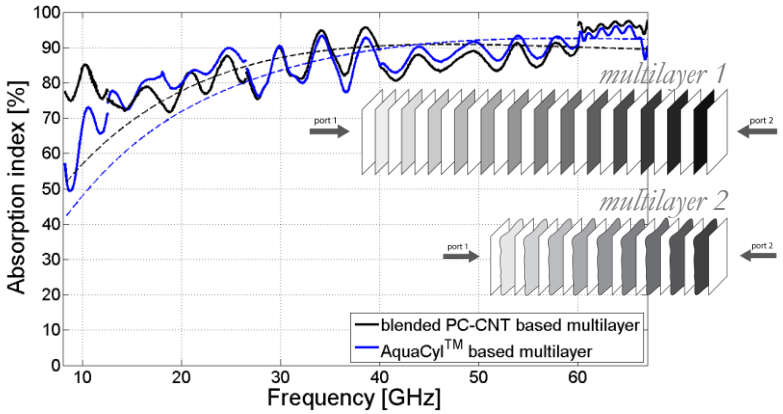


Fig. 83. absorption index of blended PC-CNT composite and AquaCyl™ sandwiches based multilayer. The dotted lines are the absorption predicted by the model. The blended composites and AquaCyl™ sandwiches based multilayers have a thickness of 4.90mm and 2.56mm respectively.

It is quite possible to cover electronic devices, medical devices or others to isolate them from external and internal fields. The main advantage of those multilayers is the potential industrial implementation at large scale. The absorber could cover large surface as rooms or entire buildings. Few large-scale solutions combining this efficiency with such a thickness are available, especially at a relatively low cost (171).

We have pushed back the absorption/thickness ratio via a novel type of broadband absorbing multilayer. The CNT composites are replaced by entangled ferromagnetic nanowires sandwiched between polymer films. The fine control of conductivity and permeability as well as a smart conductivity/permeability gradient stacking of the layers lead to very high-efficiency absorbers. Analysis by the Rozanov formalism confirms the performance compared to the theoretical limit. The difficulties to massively produce NW is probably the main limit of this system. It constrains to work at small scale unlike the CNT based multilayers. This optimal absorber seems thus totally suited for EMI

shielding of microchip and small devices needing a high absorption level despite a reduced admissible thickness.

By keeping the same multilayers concept, we have also demonstrated that the absorption can be controlled according to the polarisation of an incoming microwave. The orientation of CNT inside a polymer matrix or a CNT track pattern allows selecting the favourable absorption direction. The effect has been clearly demonstrated but some optimisation could improve the anisotropy of the conductive films. Research should be conducted to increase the stretching of the PC-CNT composites before rupture in order to improve the alignment of the CNT. The patterned lines of CNT could be designed with a smaller interdistance in order to increase the gap between the conductivity according the orthogonal directions in the plane. The fact remains that polarising multilayers presented in this thesis open the way to a novel type of polarisation-selective filters.

In summary:

The combination of conductive nanofillers (CNT or NW) and polycarbonate has clearly proved its efficiency for broadband absorption. The type of nanofiller makes the resulting shields suited either for covering large surfaces at attractive cost or for small devices requiring very high absorption/thickness ratio. The micro-structuration or alignment of charges further opens the possibility to polarisation control of the waves. The multilayers are very thin compared to wavelength and benefit to the classical advantages of polymers: resistance, flexibility and conformability.

2. Electromagnetic bandgap filtering

Some situations or devices are not helped by broadband absorption because it is too restrictive or it simply prevents normal functioning. EBG filters are often a better solution for devices connected to telecommunication networks. The challenge becomes more precisely to absorb the microwaves with the exception of the useful frequency band. We have demonstrated easy to make multilayer nanocomposite structures which open up new possibilities in the area of microwave management. The EBG are able to selectively reflect/absorb desired wavelengths. The filter shown in Fig. 84a is an absorber with some narrow band of high reflectivity. It suggests some potential for basic

filtering of signals. A parabolic antenna could, for instance, be covered by such a multilayer to only focus operating frequencies to the detector. Furthermore, the selection of the thickness or permittivity of the dielectric layers allows a complete freedom for the choice of the filtered frequency. Higher or lower frequencies can be targeted too. A very commonly used frequency nowadays is 2.4GHz corresponding to the Wi-Fi protocol. Shielding those frequencies should prevent leaks of data conveyed by this network. It is relevant for protection of privacy and general data protection. The second example of EBG in Fig. 84b acts on Wi-Fi frequency for illustrating the versatility of the method. In the latter case, we absorb only at 2.4GHZ without affecting significantly other frequency bands. Furthermore, it is built from a stone (granite) slab which is a natural choice in the conception of shields for large surfaces typical of buildings.

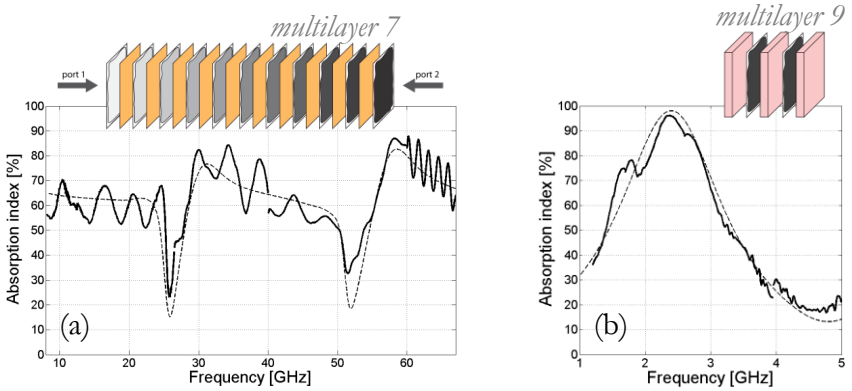


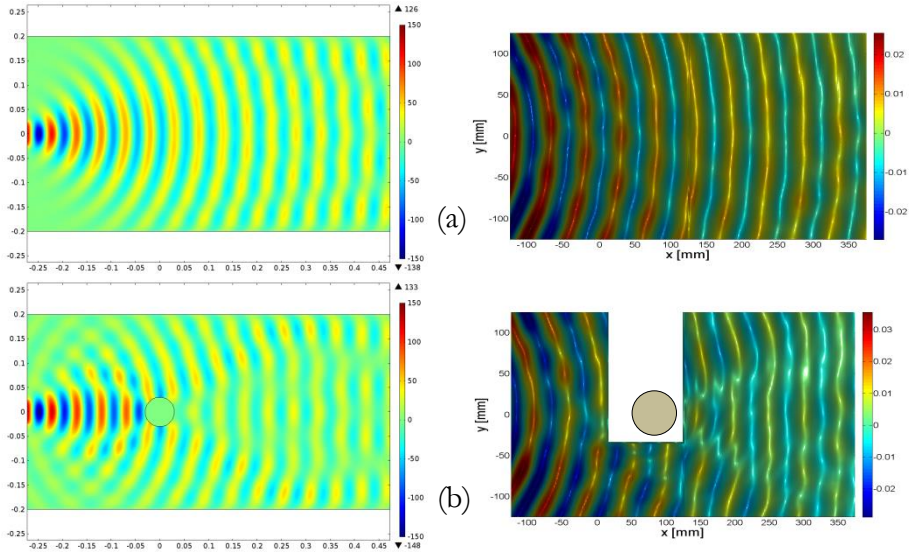
Fig. 84. EBG filter based on AquaCyl™ composites stacked in gradient of conductivity with alternately Arlon AD1000 substrate in (a). An EBG filter based on two equivalent AquaCyl™ sandwiches between natural granite slabs in (b). The dotted lines are the theoretical predictions.

In summary:

The proposed EBG filters show that CNT composites are also very attractive in the field of frequency-selective absorption. They naturally combine with many types of substrates including construction materials. The developed EM model correctly fits these materials and can be used to select the best dielectric substrate for each multilayer.

3. Invisible cloaking

Absorption or filtering (controlled in frequency or polarisation) is helpful in many applications. However, in situations such as emission/detection of a radar signal, it is much more appropriate to prevent distortion of the signal regardless of the interfering elements in the detection zone. This amounts to making the source of interference invisible to microwaves. We have developed an invisible cloaking working at 6GHz, which is a common frequency of radars. Our system is built from the same type of building blocks as in the previous sections i.e. conductive composites based on CNT ink sandwiched between PC sheets and dielectric polymer foams (ABS or Rohacell®). The materials are precisely arranged in concentric layers around a cylindrical obstacle to hide, thanks to a proper radial modulation of the effective permittivity. The concentric shield deviates the waves at a desired frequency in such a way that the wavefront passes the obstacle almost unperturbed. Fig. 85a is a mapping of the free xy table and Fig. 85b shows the perturbation provided by a highly reflecting object (here a 6cm diameter steel cylinder) which is compared with the two experimental cloaks of invisible given in Fig. 85c and Fig. 85d. They show a convincing transmission of the wavefront through the cylinder. Some perturbations are introduced because of the imperfection of the cloaking. Nevertheless, this obviously reduces the detectable area at the rear of the system. Those invisible cloaks are perhaps sufficient to exceed the detection threshold of radars.



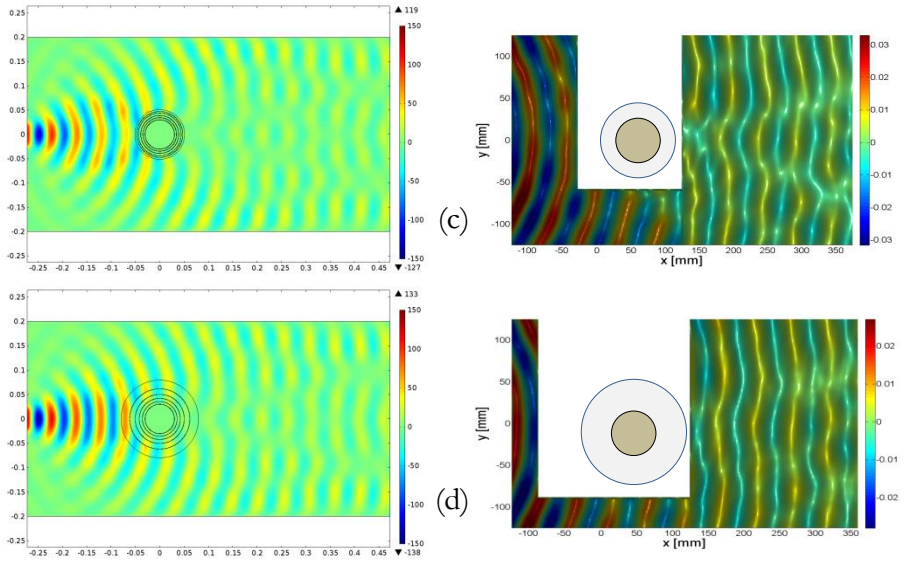


Fig. 85. characterisation of free space in (a) and a metallic cylinder in (b) which is cloaked by a stack of 5 ABS-CNT composite bilayers in (c) and a stack of 5 Rohacell®-CNT composite bilayers in (d)

In summary:

Our research has shown the feasibility of a correct control of wave propagation by a simple method of manufacturing with standard organic materials and conductive nanofillers. It is only a first step as the quality of the system is fit for improvement but some directions for progress are already identified.

The solutions in the context of this thesis fulfil their function to diminish or avoid microwave interference. The proposed solutions easily adapt on demand either to the propagation mode (by absorption or transmission by deviation), or to the aimed frequencies of operation, or to the wanted angle of polarisation. All those possibilities are the consequence of judicious hierarchical organisation of materials based on polymers and conducting nanostructures.

References

1. **M.F. Violette, J. Violette.** *Electromagnetic compatibility handbook.* s.l. : Van Nostrand Reinhold Company, 1987.
2. **W. Coats, M. Kamerling.** *Electromagnetic shield for electronic equipment. 4,381,421* 1983.
3. **G. Sridharan, K. Sridharan.** *Integrated circuit die having an interference shield. 6,486,534* 2002.
4. *Mobile phone interference with medical equipment and its clinical relevance: a systematic review.* **N. Lawrentschuk, D. Bolton.** 3, 2004, Medical journal of Australia, Vol. 181, pp. 145-149.
5. **Lee, William.** *Mobile Communications Engineering.* s.l. : McGraw-Hill Professional, 1982.
6. *GPS signal-to-noise measurement in weak signal and high-interference environments.* **P. Groves.** 2, 2005, Navigation, Vol. 52, pp. 83-94.
7. **M. Taieb.** *Évaluation de l'effet des structures éoliennes sur la réception des signaux de télédiffusion.* s.l. : Université Laval, 2009.
8. **M. Skolnik.** *Radar (chap. 24-29).* s.l. : McGraw-Hill, 1970.
9. **European Commission.** *Council Directive 89/336/EEC of 3 May 1989 on the approximation of the laws of the Member States relating to electromagnetic compatibility.* 1989.
10. —. *Directive 2004/108/EC relating to electromagnetic compatibility and repealing Directive 89/336/EEC.* 2004-2014.
11. **B. Mulder, Q. Chu, D. Choukroun, E.-J. van Kampen, C. de Visser, G. Looye.** *Advances in aerospace guidance, navigation and control.* [éd.] S. Theil F. Holzapfel. s.l. : Springer, 2011.
12. *Radar Performance Degradation due to the Presence of Wind Turbines.* **A. Theil, L. van Ewijk.** 2007, IEEE Radar Conference, pp. 75-80.

13. *Wind farm clutter mitigation in air surveillance radar.* **J. Perry, A. Biss.** 7, 2007, IEEE Aerospace and Electronic Systems Magazine, Vol. 22, pp. 35-40.
14. *Assessment of the Effects of Wind Turbines on Air Traffic Control Radars.* **J. Lemmon, J. Carroll, F. Sanders, D. Turner.** 454, 2008, National Telecommunications & Information Administration, Vol. 8.
15. *Impacts of wind farms on WSR-88D operations and policy considerations.* **J. Vogt, J. Reed, T. Crum, J. Snow, R. Palmer, B. Isom, D. Burgess.** B, 2007, 23rd Int. Conf. on Interactive Information Processing Systems for Meteorology, Oceanography and Hydrology, Vol. 5.
16. *Characterization Approach of Wind Turbine Clutter in the Spanish Weather Radar Network.* **B. Gallardo, F. Pérez, F. Aguado.** 2008, 5th European Conference on Radar in Meteorology and Hydrology.
17. **Leland H. Hemming.** *Architectural Electromagnetic Shielding Handbook: A Design and Specification Guide.* s.l. : Wiley-Blackwell, 2000.
18. *Thin and flexible multilayer polymer composite structures for effective control of microwave electromagnetic absorption.* **Y. Danlée, C. Bailly, I. Huynen.** 2014, Composites Science and Technology, Vol. 100, pp. 182-188.
19. *Formulas for the Skin Effect.* **H. Wheeler.** 9, 1942, IEEE Proceedings of the IRE, Vol. 30, pp. 412-424.
20. **P. S. Neelakanta.** *Electromagnetic Materials: Monolithic and Composite Versions and Their Applications.* 1995.
21. **Xingcun Colin Tong.** *Advanced materials and design for electromagnetic interference shielding.* s.l. : CRC Press, 2008.
22. *Reflection Properties of the Salisbury Screen.* **R. Fante, M. Mccormack.** 1988, IEEE Transactions on Antennas and Propagation, Vol. 36, pp. 1443-1454. http://dx.doi.org/10.1109/8.8632.
23. *A design process for Jaumann absorbers.* **L. du Toit, J. Cloete.** 1989, Antennas and Propagation Society International Symposium, Vol. 3, pp. 1558-1561.
24. *Multifunctional hybrids for electromagnetic absorption.* **I. Huynen, N. Quiévy, C. Bailly, P. Bollen, C. Detrembleur, S. Eggermont, I. Molenberg, J.-M. Thomassin, L. Urbanczyk, T. Pardoen.** 8, 2011, Acta Materiala, Vol. 59, pp. 3255-3266.
25. **P. Bollen.** *Hierarchical hybrid materials combining wideband electromagnetic absorption and mechanical performance.* 2015.
26. *Design, fabrication, and characterization of lightweight and broadband microwave absorbing structure reinforced by two dimensional composite lattice.* **M. Chen, Y. Pei, D. Fang.** 1, 2012, Applied Physics A: Materials Science & Processing, Vol. 108, pp. 75-80. 10.1007/s00339-012-7002-7.

27. *Microwave absorbing composite lattice grids.* **H. Fan, W. Yang, Z. Chao.** 15-16, 2007, Composites Science and Technology, Vol. 67, pp. 3472-3479.
28. *Broadband EMI absorbing materials.* **C. A. Grimes.** 1993, IEEE International Symposium on Electromagnetic Compatibility , pp. 245-249. 10.1109/isemc.1993.473737.
29. *Ferrite grid electromagnetic wave absorbers.* **Y. Naito, H. Anzai, T. Mizumoto, M. Takahashi.** 1993, IEEE International Symposium on Electromagnetic Compatibility, pp. 254-259. 10.1109/isemc.1993.473735.
30. *Microwave reflection at an active surface imbedded with fast-ion conductors.* **P. Neelakanta, J. Abello, C. Gu.** 5, 1992, IEEE Transactions on Microwave Theory and Techniques, Vol. 40, pp. 1028-1030. 10.1109/22.137416.
31. *Carbon nanotube composites for broadband microwave absorbing materials.* **A. Saib, L. Bednarz, R. Daussin, C. Bailly, X. Lou, J-M. Thomassin, C. Pagnoulle, C. Detrembleur, R. Jerome, I. Huynen.** 2005, Microwave Conference, Vol. 1.
32. *Comparison study on the effect of carbon nano materials for single-layer microwaveabsorbers in X-band.* **J-B. Kim, S-K. Lee, C-G. Kim.** 14, 2008, Composites Science and Technology, Vol. 68, pp. 2909–2916.
33. *Multiwalled carbon nanotube/poly(ε-caprolactone) nanocomposites with exceptional electromagnetic interference shielding properties.* **J-M.Thomassin, X. Lou, C. Pagnoulle, A. Saib, L. Bednarz, I. Huynen, R. Jerome, C. Detrembleur.** 30, 2007, J. Phys. Chem. C, 2007, 111 (30), pp, Vol. 111, pp. 11186–11192.
34. *Rheological behavior of multiwalled carbon nanotube/polycarbonate composites.* **P. Pötschke, T. D. Fornes, D. R. Paul.** 11, 2002, Polymer, Vol. 43, pp. 3247–3255.
35. *Electrical conductivity and electromagnetic interference shielding of multiwalled carbon nanotube composites containing Fe catalyst.* **H. M. Kim.** 4, 2004, Applied Physics Letters, Vol. 84, pp. 589-591.
36. *Electromagnetic interference shielding effectiveness of carbon materials.* **D. Chung.** 2, 2001, Carbon, Vol. 39, pp. 279-285.
37. *Novel Carbon Nanotube−Polystyrene Foam Composites for Electromagnetic Interference Shielding.* **Y. Yang, M. C. Gupta.** 11, 2005, NanoLetters, Vol. 5, pp. 2131–2134.
38. *Electromagnetic absorption properties of carbon nanotube nanocomposite foam filling honeycomb waveguide structures.* **N. Quiévy, P Bollen, J.-M. Thomassin, C. Detrembleur, T. Pardoen, C. Bailly, I. Huynen.** 1, IEEE Transactions on Electromagnetic Compatibility (Spec. Nanotechnology), Vol. 54, pp. 43-51.

39. *Carbon Nanotube–Polycarbonate Composites.* **R. O. Loutfy, J.C. Withers, M. Abdelkader, et al.** 2002, Perspectives of Fullerene Nanotechnology, pp. 317–325.
40. *Mechanical and flame resistant properties of polycarbonate-carbon nanotubes-ochre composites.* **S. C. Moon, J. Y. Kim, B. T. Oh.** 11, 2013, Polymer Engineering and Science.
41. *Carbon nanotube-filled polycarbonate composites produced by melt mixing and their use in blends with polyethylene.* **P. Potschke, A. R. Bhattacharyya, A. Janke.** 5–6, 2004, Carbon, Vol. 42, pp. 965–969.
42. *Decorating carbon nanotubes with metal or semiconductor nanoparticles.* **V. Georgakilas, D. Gournis, V. Tzitzios, L. Pasquato, D. Guldi, M. Prato.** 26, 2007, Journal of Materials Chemistry, Vol. 17, pp. 2679-2694.
43. *Optimization of electromagnetic matching of Fe-filled carbon nanotubes/ferrite composites for microwave absorption.* **X. Gui, W. Ye, J. Wei, K. Wang, R. Lu, H. Zhu, F. Kang, J. Gu, D. Wu.** 7, Journal of Physics D: Applied Physics, Vol. 42.
44. *Broadband RF Noise Suppression by Magnetic Nanowire-Filled Composite Films.* **B. Nam, Y.-H. Choa, S.-T. Oh, S. Lee, K. Kim.** 6, 2009, IEEE Transactions on Magnetics, Vol. 45, pp. 2777-2780.
45. *Ultra-thin Nickel nanowires films for high efficiency large band shielding by absorption.* **Y. Danlée, C. Bailly, I. Huynen, L. Piraux.** 2014, Smart Materials & Structures.
46. *Ultimate thickness to bandwidth ratio of radar absorbers.* **K. N. Rozanoz.** 8, 2000, IEEE Antennas & Propagation, Vol. 48, pp. 1230-1234.
47. *A novel design method for electromagnetic bandgap based waveguide filters with periodic dielectric loading.* **S. Şimşek, E. Topuz, E. Niver.** 3, 2012, AEU - International Journal of Electronics and Communications, Vol. 66, pp. 228–234.
48. *Ultrathin multiband gigahertz metamaterial absorbers.* **H. Li, L. Yuan, B. Zhou, X. Shen, Q. Cheng, T. Cui.** 1, 2011, J. Appl. Phys., Vol. 110.
49. *Electromagnetic band-gap structures: classification, characterization and applications.* **Y. Rahmat-Samii, H. Mosallaei.** 480, 2001, 11th International Conference on Antennas and Propagation, Vol. 2, pp. 560-564.
50. *Transmission lines on periodic bandgap metamaterials from microwaves to optics applications.* **A. Saib, I. Huynen.** 2, 2005, J. Opt. A: Pure Appl. Opt., Vol. 7.
51. **N. Engheta, R. Ziolkowski.** *Metamaterials: Physics and Engineering Explorations.* s.l. : John Wiley & Sons, 2006.
52. **Filippo Capolino.** *Theory and phenomena of metamaterials.* s.l. : Taylor & Francis Group, 2009.

53. **Xun-Ya Jiang.** *Metamaterial (chap 13).* s.l. : InTech, 2012.
54. *Manufacturing Tolerance Analysis, Fabrication, and Characterization of 3-D Submillimeter-Wave Electromagnetic-Bandgap Crystals.* **B. Martinez, I. Ederra, R. Gonzalo, B. Alderman.** 4, 2007, IEEE Transactions on Microwave Theory and Techniques, Vol. 55.
55. *Fragility of photonic band gaps in inverse-opal photonic crystals.* **Z.-Y. Li, Z.-Q. Zhang.** 1516, 2000, Physical Review B, Vol. 62.
56. *On EBG Structures for Cellular Phone Applications.* **F. Bilotti, L. Vegni, F. Viviani.** 6, 2003, AEU - International Journal of Electronics and Communications, Vol. 57, pp. 403–408.
57. *A novel compact electromagnetic-bandgap (EBG) structure and its applications for microwave circuits.* **L. Yang, M. Fan, F. Chen, J. She, Z. Feng.** 1, 2005, IEEE Transactions on Microwave Theory and Techniques, Vol. 53, pp. 183-190.
58. *Metamaterials in Electromagnetic Wave Absorbers.* **A. Dubey, T. Shami.** 4, 2012, Defence Science Journal, Vol. 62. 10.14429/dsj.62.1514.
59. **T. K. Wu.** *Frequency Selective Surface and Grid Array.* s.l. : John Wiley & Sons, 1995.
60. **F. Nians, J. Matson.** *Antenna feed system simultaneously operable at two frequencies utilizing polarization independent frequency selective intermediate reflector. US3231892 A* 1966.
61. *Transmission through a two-layer array of loaded slots.* **B. Munk, R. Luebbers, R. Fulton.** 6, 2003, IEEE Transactions on Antennas and Propagation, Vol. 22, pp. 804-809.
62. *Far-infrared properties of metallic mesh and its complementary structure.* **R. Ulrich.** 1, 1967, Infrared Physics, Vol. 7, pp. 37-55. 10.1016/0020-0891(67)90028-0.
63. *Far-IR optical properties of freestanding and dielectrically backed metal meshes.* **M. Durschlag, T. De Temple.** 7, 1981, Applied Optics, Vol. 20, pp. 1245-1253. 10.1364/AO.20.001245.
64. *A grid amplifier.* **K. Moonil, J. Rosenberg, P. Smith, R. Weikle, J. Hacker, M. De Lisio, D. Rutledge.** 11, 1991, IEEE Microwave and Guided Wave Letters, Vol. 1, pp. 322-324.
65. *Frequency selective surfaces on biased ferrite substrates.* **T. Chang, R. Langley, E. Parker.** 15, 1994, Electronics Letters, Vol. 30, pp. 1193-1194.
66. *Tunable frequency selective surface using liquid substrates.* **A. de C. Lima, E. Parker, R. Langley.** 4, 1994, Electronics Letters, Vol. 30, pp. 281-282.
67. *Scattering by a two dimensional periodic array of conducting rings on a chiral slab.* **T. Ege.** 1995, Antennas and Propagation Society International Symposium, Vol. 3, pp. 1667-1670 .

68. *Thin absorbing screens using metamaterial surfaces.* **N. Engheta.** 2002, IEEE Antennas and Propagation Society International Symposium, Vol. 2, pp. 392-395.
69. **R. Pierrot.** *Reflector for Circularly Polarized Waves. 3500420* 1970.
70. *A new advance in circular polarization selective surface: A three layered CPSS without vertical conductive segments.* **I.-Y. Tarn, S.-J. Chung.** 2, 2007, IEEE Transaction Antennas Propagation, Vol. 55, pp. 460-467.
71. *Layered chiral metallic microstructures with inductive coupling.* **Y. Svirko, N. Zheludev, M. Osipov.** 4, 2001, Applied Physics Letters, Vol. 78, pp. 498-500.
72. *Anisotropic impedance surfaces for linear to circular polarization conversion.* **E. Doumanis, G. Goussetis, J. Gomez-Tornero, R. Cahill, V. Fusco.** 1, 2012, IEEE Transaction Antennas Propagation, Vol. 60, pp. 212-219.
73. *Chirality and bianisotropy effects in plasmonic metasurfaces and their application to realize ultrathin optical circular polarizers.* **A. Alu, Y. Zhao, X.-X. Liu.** 2011, General Assembly and Scientific Symposium, pp. 1-4.
74. **Gábor Horváth.** *Polarized Light and Polarization Vision in Animal Sciences.* s.l. : Springer, 2014.
75. **David Armitage, Ian Underwood, Shin-Tson Wu.** *Introduction to Microdisplays.* s.l. : John Wiley & Sons, 2006.
76. **Graham Smith, Terry King, Dan Wilkins.** *Optics and Photonics: An Introduction.* s.l. : John Wiley & Sons, 2007.
77. **Michael Vollmer, Klaus-Peter Möllmann.** *Infrared Thermal Imaging: Fundamentals, Research and Applications.* s.l. : John Wiley & Sons, 2010.
78. **G. Raju.** *Radar Engineering.* s.l. : I. K. International, 2008.
79. *Carbon Nanotube Terahertz Polarizer.* **L. Ren, C. Pint, L. Booshehri, W. Rice, X. Wang, D. Hilton, K. Takeya, I. Kawayama, M. Tonouchi, R. Hauge, J. Kono.** 7, 2009, Nano Letters, Vol. 9, pp. 2610-2613.
80. *Broadband Terahertz Polarizers with Ideal Performance Based on Aligned Carbon Nanotube Stacks.* **L. Ren, C. Pint, T. Arikawa, K. Takeya, I. Kawayama, M. Tonouchi, R. Hauge, J. Kono.** 2, 2012, Nano Letters, Vol. 12, pp. 787-790.
81. *Analysis and design of a two-octave polarization rotator for microwave frequency.* **R. Torres, M. Catedra.** 2, 1993, IEEE Transactions on Antennas and Propagation, Vol. 41, pp. 208-213.
82. *Liquid crystals for twisted nematic display devices.* **G. Gray, S. Kelly.** 9, 1999, Journal of Materials Chemistry, Vol. 9, pp. 2037-2050.
83. *Synthesizing a Twist Polarizer.* **T. Niemi, A. Karilainen, S. Tretyakov.** 2012, IEEE Antennas and Propagation Society International Symposium, pp. 1-2.

84. **Marek Matuszczyk.** *Structures and Properties of Ferroelectric Liquid Crystal Displays.* s.l. : Chalmers Tekniska Högsk, 1996.
85. *Broadband Acoustic Cloak for Ultrasound Waves.* **S. Zhang, C. Xia, N. Fang.** 2011, Physical Review Letters, Vol. 106.
86. *The Anti-Cloak.* **H. Chen, X. Luo, H. Ma, C. Chan.** 19, 2008, Optics Express, Vol. 16, pp. 14603-14608.
87. *Complementary Media Invisibility Cloak that Cloaks Objects at a Distance Outside the Cloaking Shell.* **Y. Lai, H. Chen, Z.-Q. Zhang, C. Chan.** 9, 2009, Physical Review Letters, Vol. 102, p. 093901.
88. *Controlling Electromagnetic Fields.* **J. Pendry, D. Schurig, D. Smith.** 2006, Science, Vol. 312.
89. *Metamaterial Electromagnetic Cloak at Microwave Frequencies.* **D. Schurig, J. Mock, B. Justice, S. Cummer, J. Pendry, A. Starr, D. Smith.** 2006, Science, Vol. 314, pp. 977-980.
90. *Experimental study on transparency induced by metamaterials.* **J. Hu, Q. Deng, X. Cai, X. Zhou, G. Hu.** 2008, IEEE International Workshop on Metamaterials.
91. *Hiding under the Carpet: A New Strategy for Cloaking.* **J. Li.** 20, 2008, Physical Review Letters, Vol. 101.
92. *Optical cloaking with metamaterials.* **W. Cai, U. Chettiar, A. Kildishev, V. Shalaev.** 2007, Nature Photonics, Vol. 1, pp. 224-227.
93. *Composite medium with simultaneously negative permeability and permittivity.* **D. Smith, W. Padilla, D. Vier, S. Nemat-Nasser, S. Schultz.** 18, 2000, Physical Review Letters, Vol. 84, pp. 4184-4187.
94. *Influence of Carbon Nanofiber Network Variability on the AC Conductivity of Polyetherimide Composite Films.* **B. Li, W.-H. Zhong.** 4, 2010, Macromolecular Materials and Engineering, Vol. 295, pp. 310-314.
95. *Microwave absorbing performances of multiwalled carbon nanotube composites with negative permeability.* **L. Deng, M. Han.** 023119, 2007, Applied Physics Letters, Vol. 91.
96. **J. A. Kong.** *Electromagnetic Wave Theory.* s.l. : Cambridge, 2000.
97. **C. Bohren, D. Huffman.** *Absorption and scattering of light by small particles.* s.l. : Wiley, 1983.
98. **D. Pozar.** *Microwave Engineering (2nd ed.).* s.l. : Wiley, 1997.
99. *Computation design and performance prediction towards a multi-layer microwave absorber.* **M. Cao, J. Zhu, J. Yuan, T. Zhang, Z. Peng, Z. Gao, G. Xiao, S. Qin.** 6, 2002, Materials and Design, Vol. 23, pp. 557-564.
100. *Microwave absorbers based on foamed nanocomposites with graded concentration of carbon nanotubes.* **I. Huynen, L. Bednarz, J-M.Thomassin, C. Pagnoulle, R. Jerome, C. Detrembleur.** 2008, Microwave Conference, pp. 5-8.

101. *Polymer/Carbon based composites as Electromagnetic Interference (EMI) shielding materials.* **J.-M. Thomassin, C. Jérôme, T. Pardoen, C. Bailly, I. Huynen, C. Detrembleur.** 7, 2013, Materials Science and Engineering Reports, Vol. 74, pp. 211-232.
102. **H. M. Nussenzveig.** *Causality and Dispersion Relations.* s.l. : Academic Press New York, 1972.
103. **L. M. Brekhovskikh.** *Waves in Layered Media (2nd Edition).* s.l. : Academic, 1980.
104. *Ultra Thin Metamaterial Absorbers Using Electric Field Driven LC (ELC) Resonator Structure.* **S. Bhattacharyya, K. V. Srivastava.** 2012, PIERS Proceedings, pp. 314-317.
105. *The Theory and Design of Provably Optimal Bandwidth Radar Absorbent Materials (RAM) using Dispersive Structures and/or Frequency Selective (FSS).* **A. Mackay.** 2007, International Conference on Electromagnetics in Advanced Applications, pp. 157-160 .
106. *Reflection and transmission guided-mode resonance filters.* **S. Tibuleac, R. Magnusson.** 7, 1997, Journal of the Optical Society of America A, Vol. 14, pp. 1617-1626.
107. **R. Magnusson, S.-S. Wang.** *Efficient bandpass reflection and transmission filters with low sidebands based on guided-mode resonance effects. US 08/465,386* 1995.
108. *A low-frequency model for wedge or pyramid absorber arrays - I: theory.* **E. Kuester, C. Holloway.** 4, 1994, IEEE Transactions on Electromagnetic Compatibility, Vol. 36, pp. 300-306.
109. *A low-frequency model for wedge or pyramid absorber arrays - II: computed and measured results.* **E. Kuester, C. Holloway.** 4, 1994, IEEE Transactions on Electromagnetic Compatibility, Vol. 36.
110. *Surface plasmon transmission across narrow grooves in thin silver films.* **J. Seidel, S. Grafström, L. Eng, L. Bischoff.** 9, 2003, Appied Physics Letters, Vol. 82, p. 1368.
111. *Characteristics of an electromagnetic wave absorbing composite structure with a conducting polymer electromagnetic bandgap (EBG) in the X-band.* **W.-J. Lee, J.-W. Lee, C.-G. Kim.** 12, 2008, Composites Science and Technology, Vol. 68, pp. 2485-2489.
112. *Modelling of intrinsic conducting polymer for Wi-Fi electromagnetic interference shielding.* **W. Al-Shabib, S. Lachowicz.** 2013, Science and Information Conference, pp. 836-838.
113. *Broad-Band Microwave Transmission Characteristics from a Single Measurement of the Transient Response.* **A. M. Nicolson.** 4, 1968, IEEE Transactions on Instrumentation and Measurement, Vol. 17, pp. 395-402.

114. *Automatic measurement of complex dielectric constant and permeability at microwave frequencies.* **W. B. Weir.** 1, 1974, Proceedings of IEEE, Vol. 62, pp. 33-36.
115. *Transmission/Reflection Method Based on Coaxial Line for RF Materials Characterization Measurement.* **S.-H. Jing, Q.-X. Jiang.** 5, 2005, Journal of Astronautics, Vol. 26.
116. *Modified algorithm on electromagnetic parameters test.* **G. Yang, S. Jiang, G. Wang.** 8, 2007, Theory and Method, Vol. 26.
117. *Noniterative stable transmission/reflection method for low-loss material complex permittivity determination.* **A.-H. Boughriet.** 1, 1997, IEEE Transactions on Microwave Theory and Techniques, Vol. 45, pp. 343-349.
118. *Investigation of effective permittivity and permeability for a novel v-shaped metamaterial using simulated s-parameters.* **E. Ekmekçi, G. Turhan-Sayan.** 2007, Proceedings of 5th International Conference on Electrical and Electronics Engineering, pp. 251–254.
119. *A Unique Extraction of Metamaterial Parameters based on Kramers-Kronig Relationship.* **Z. Szabó, G.-H. Park, R. Hedge, E.-P. Li.** 10, 2010, IEEE Transactions on Microwave Theory and Techniques, Vol. 58, pp. 2646-2653.
120. *Robust method to retrieve the constitutive effective parameters of metamaterials.* **X. Chen, T. Grzegorczyk, B.-I. Wu, J. Pacheco, J. Kong.** 2004, Pysical Review E, Vol. 70.
121. *Electromagnetic parameter retrieval from inhomogeneous metamaterials.* **D. Smith, D. Vier, T. Koschny, C. Soukoulis.** 2005, Physical Review E, Vol. 71.
122. *The effect of particle size on electric conducting percolation threshold in polymer/conducting particle composites.* **X. Jing, W. Zhao, L. Lan.** 5, 2000, Journal of Materials Science Letters, Vol. 19, pp. 377-379.
123. *Polymer micro and nanocomposites: Structure, interactions, properties.* **J. Móczó, B. Pukánszky.** 5, 2008, Journal of Industrial and Engineering Chemistry, Vol. 14, pp. 535-563.
124. *Polymer nanotechnology: Nanocomposites.* **D. Paula, L. Robeson.** 15, 2008, Polymer, Vol. 49, pp. 3187–3204.
125. *Correlations between Percolation Threshold, Dispersion State, and Aspect Ratio of Carbon Nanotubes.* **J. Li, P. Ma, W. Chow, C. To, B. Tang, J.-K. Kim.** 16, 2007, Advanced Functional Materials, Vol. 17, pp. 3207-3215.
126. **R. Saito, G. Dresselhaus, M. S. Dresselhaus.** *Physical Properties of Carbon Nanotubes.* s.l. : London: Imperial college press, 1998.
127. **J. Israelachvili.** *Intermolecular and Surface Forces (3rd ed.).* s.l. : Academic Press, 2011.

128. *Carbon nanotube–polymer interactions in nanocomposites: A review.* **M. Rahmat, P. Hubert.** 1, 2011, Composites Science and Technology, Vol. 72, pp. 72-84.
129. **R. Good, M. Chaudhury.** *Theory of adhesive forces across interfaces - 1. The Lifshitz-van der Waals Component of interaction and adhesion (Vol. 3).* 1991.
130. *Van der Waals forces between cylinders: I Nonretarded force between thin isotropic rods and finite size corrections.* **D. Mitchell, B. Ninham, P. Richmond.** 4, 1973, Biophysical Journal, Vol. 13, pp. 359-369.
131. *Van der Waals forces between cylinders: II Retarded interaction between thin isotropic rods.* **D. Mitchell, B. Ninham, P. Richmond.** 4, 1973, Biophysical Journal, Vol. 13, pp. 370-384.
132. *Near-Static Dielectric Polarization of Individual Carbon Nanotubes.* **W. Lu, D. Wang, L. Chen.** 9, 2007, Nano Letters, Vol. 7, pp. 2729-2733.
133. *Static Dielectric Properties of Carbon Nanotubes from First Principles.* **B. Kozinsky, N. Marzari.** 166801, 2006, Physical Review Letters, Vol. 96.
134. *Percolation and conductivity: A computer study.* **G. Pike, C. Seager.** 1421, 1974, Physical Review B, Vol. 10.
135. **Kim Christensen.** *Percolation Theory.* s.l. : MIT, 2002.
136. *Percolation Theory Generates a Physically Based Description of Tortuosity in Saturated and Unsaturated Porous Media.* **B. Ghanbarian, A. Hunt, M. Sahimi, R. Ewing, T. Skinner.** 6, 2013, Soil Science Society of America Journal, Vol. 77, pp. 1920-1929.
137. *Electrical conducting behaviors in polymeric composites with carbonaceous fillers.* **D. Zhu, Y. Bin, M. Matsuo.** 2007, Journal of Polymer Sciences Part B: Polymer Physics, Vol. 45, pp. 1037-1044.
138. *Comparison of the effective conductivity between composites reinforced by graphene nanosheets and carbon nanotubes.* **S. Xie, Y. Liu, J. Li.** 2008, Applied Physics Letters, Vol. 92, p. 243121.
139. *Comparison of electrical properties between multi-walled carbon nanotube and graphene nanosheet/high density polyethylene composites with a segregated network structure.* **D. Jinhong, Z. Long, Z. You, Z. Zhang, L. Feng, L. Pengfei, L. Chang.** 2011, Carbon, Vol. 49, pp. 1094 -1100.
140. *Simulations and generalized model of the effect of filler size dispersity on electrical percolation in rod networks.* **R. Mutiso, M. Sherrott,J. Li,K. Winey.** 2012, Physical Review B, Vol. 86, p. 214306.
141. *Effect of nanotube alignment on percolation conductivity in carbon nanotube/polymer composites.* **F. Du, J. Fischer, K. Winey.** 12, 2005, Physical Review B, Vol. 72.

142. *Critical concentration in percolating systems containing a high-aspect-ratio filler.* **A. Celzard, E. Mc Rae.** 10, 1996, Physical Review B, Vol. 53, pp. 6209-6214.
143. *Percolation Theory and Electrical Conductivity.* **B. Last, D. Thouless.** 1719, 1971, Physical Review Letter, Vol. 27.
144. *Characteristics of the electrical percolation in carbon nanotubes/polymer nanocomposites.* **X. Zeng, X. Xu, P. Shenai, E. Kovalev, C. Baudot, N. Mathews.** 2011, Journal of Physical Chemistry C, Vol. 115, pp. 21685–21690.
145. *Optical conformal mapping.* **U. Leonhardt.** 2006, Science, Vol. 312, pp. 1777-1780.
146. *Transformation methods in computational electromagnetism.* **A. Nicolet, J.F. Remacle, B. Meys, A. Genon, W. Legros.** 10, 1994, Journal of Applied Physics, Vol. 75, pp. 6036-6038. 10.1063/1.355500.
147. *Refraction and geometry in Maxwell's equations.* **A. Ward, J. Pendry.** 4, 1996, Journal of Modern Optics, Vol. 43, pp. 773-793.
148. **M. Yan, W. Yan, M. Qiu.** Chap. 4 - Invisibility Cloaking by Coordinate Transformation. [auteur du livre] Emil Wolf. *Progress in Optics (vol. 52).* s.l. : Elsevier, 2009, pp. 261-304.
149. *Transformation optics and the geometry of light.* **U. Leonhardt, T. Philbin.** 69, 2009, Progress in Optics, Vol. 53.
150. **C. Dodson, T. Poston.** *Tensor Geometry: The Geometric Viewpoint and Its Uses.* s.l. : Springer, 1991.
151. **P. Zhang.** *Theory of transformation optics and invisibility cloak design.* Sweden : KTH Electrical Engineering, 2011. Doctoral Thesis in Electromagnetic Theory.
152. **Richard Fitzpatrick.** *Maxwell's Equations and the Principles of Electromagnetism.* s.l. : Jones & Bartlett, 2008.
153. *Electromagnetic cloaking by layered structure of homogeneous isotropic materials.* **Y. Huang, Y. Feng, T. Jiang.** 18, 2007, Optics Express, Vol. 15, pp. 11133-11141.
154. *Measurement of the Intrinsic Properties of Materials by Time-Domain Techniques.* **A. Nicolson, G. Ross.** 4, 1970, IEEE Transactions on Instrumentation and Measurement, Vol. 19, pp. 377-382.
155. *Métamatériaux.* **A. de Lustrac.** Universté Paris 10.
156. *SRRs' artificial magnetic metamaterials modeling using transmission line therory.* **Q. Wu, M.-F. Wu, F.-Y. Meng, J. Wu, L.-W. Li.** 5, 2005, Progress In Electromagnetics Research Symposium 2005, Vol. 1, pp. 630-633.
157. *Shape- and Size-Dependent Refractive Index Sensitivity of Gold Nanoparticles.* **H. Chen, X. Kou , Z. Yang , W. Ni, J. Wang.** 10, 2008, Langmuir, Vol. 24, pp. 5233-5237.

158. *Size dependence of refractive index of gold nanoparticles.* **L. Scaffardi, J. Tocho.** 5, 2006, Nanotechnology, Vol. 17.
159. *A Wideband Line–Line Dielectrometric Method for Liquids, Soils, and Planar Substrates.* **I. Huynen, C. Steukers, F. Duhamel.** 5, 2001, IEEE Transactions On Instrumentation And Measurement, Vol. 50, pp. 1343-1348.
160. *Simple, convenient, and nondestructive electromagnetic characterization technique for composite and multiscale hybrid samples at microwave frequencies.* **I. Molenberg, M. Bernal, P. Bollen, D. Spote, R. Verdejo, T. Pardoen, C. Bailly, I. Huynen.** 2, 2014, Microwave and Optical Technology Letters, Vol. 56, pp. 504-509.
161. *TFU Calibration Kit for Characterizing Waveguide-Embedded Microstrip Circuits At Millimeter-Wave Frequencies.* **V. Niculae, U. Pisani.** 2002, IEEE Insmentation and Measurement Technology Conference, pp. 1349-1354.
162. *4–8 GHz Near-Field Probe for Scanning of Apertures and M ultimode Waveguides.* **I. Russo, W. Menzel.** 12, 2011, IEEE Microwave and Wireless Components Letters, Vol. 21.
163. *Frequency-Selective Coatings Based on EBG Structure Combining Carbon Nanotubes with Polymeric or Ceramic Substrate.* **Y. Danlée, C. Bailly, I. Huynen.** 2014, Conference EuCap.
164. **M. Koledintseva, E. Yelsukov K. Rozanov.** *Chap.15: Frequency-Dependent Effective Material Parameters of Composites as a Function of Inclusion Shape, Composites and Their Properties.* s.l. : Ning Hu, 2012.
165. *Synthesis of ultra long vertically aligned carbon nanotubes using the rapid heating and cooling system in the thermal chemical vapor deposition process.* **C. Chiu, T. Tsai, N. Tai, C. lee.** 10, 2006, Surface and Coatings Technology, Vol. 200, pp. 3215-3219.
166. *Understanding dielectric constant for microwave PCB materials.* **J. Coonrod, A.Horn.** 23, 2011, High Frequency Electronics, Vol. 18.
167. *Improvement of electromagnetic wave (EMW) shielding through inclusion of electrolytic manganese dioxide in cement and tile-based composites with application for indoor wireless communication systems.* **J. Pretorius, B. Maharaj.** 8, 2013, International Journal of Physical Sciences, Vol. 8, pp. 295-301.
168. *Frequency-Selective Multilayer Electromagnetic Bandgap Structure Combining Carbon Nanotubes with Polymeric or Ceramic Substrates.* **Y. Danlée, I. Huynen, C. Bailly.** 13, 2014, Applied Physics Letters, Vol. 105.
169. *Printable Thin Film Supercapacitors Using Single-Walled Carbon Nanotubes.* **M. Kaempgen, C. Chan, J. Ma, Y. Cui, G. Gruner.** 5, 2009, Nano Letters, Vol. 9, pp. 1872-1876. 0.1021/nl8038579.
170. *Synthesis and characterization of carbon nanotube-conducting polymer thin films.* **N. Ferrer-Anglada, M. Kaempgen, V. Skákalová, U. Dettlaf-**

Weglikowska, S. Roth. 2, 2004, Diamond and Related Materials, Vol. 13, pp. 256-260. 10.1016/j.diamond.2003.10.026.
171. *EMI shielding plastics: A review.* **J.H. Huang.** 2, 1995, Advances in Polymer Technology, Vol. 14, pp. 137-150. 10.1002/adv.1995.060140205.
172. *Surface modification of ultrafiltration membranes by low temperature plasma - II. Graft polymerization onto polyacrylonitrile and polysulfone.* **M. Ulbricht, G. Belfort.** 2, 1996, Journal of Membrane Science, Vol. 111, pp. 193-215.

Annex A

Plasma treatment for adhesion of CNT ink on PC

The spreading of AquaCyl™ on polycarbonate requires a surface treatment to increase the contact angle. Preliminary test was realised with the coupling agent 3-aminopropyltriethoxysilane which acts as interface between PC and AquaCyl™. The adhesion is clearly improved but the dispersion of CNT remains insufficient. AquaCyl™ leaves areas of CNT density visible to the naked eye. The process is therefore not followed up. Other experiments have shown that a plasma activation provides a homogenous and better wetting. Research on the wettability of polycarbonate has logically led to this path.

1. Experimental results

Polycarbonate sheets have been exposed to some types of plasma to compare the ability to increase the wettability. A droplet of ultra-pure water is put down on the surface to measure the contact angle. The angle is defined as

$$\theta = 2\arctan\left(\frac{2h}{b}\right) \qquad \textit{eq. A-1}$$

where h is the high on the middle of the droplet and b is the width of the droplet (see inset of Fig. 86). Wettability of pure polycarbonate with PC activated by argon, oxygen or water plasma is compared in Fig. 86. Oxygen plasma starts from pure O_2 but the gas is quickly excited to convert partially oxygen to ozone. The water plasma is actually plasma made from ambient air. The chamber is filled with filtered air. It is thus mainly composed of O_2, N_2 and ambient humidity. The H_2O molecule is particularly reactive to activate a surface. The industry and scientific literature exploit this plasma for its high ratio cost/efficiency (172). By the way, Fig. 86 proves that water plasma decreases at best the contact angle.

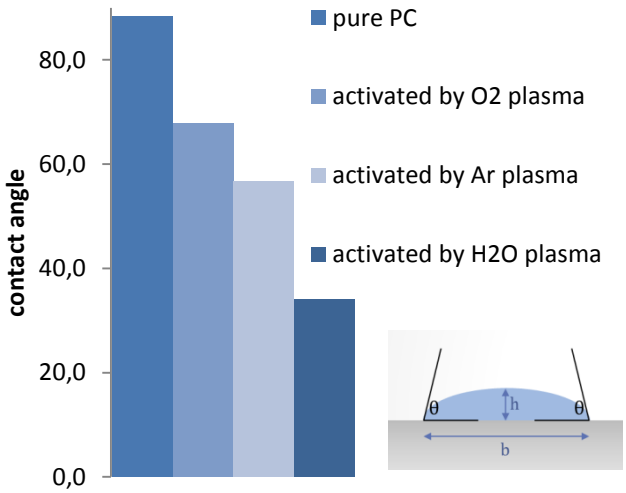


Fig. 86. Measurements of contact angle of polycarbonate surface exposed to different plasmas.

Fig. 86 highlighted that the nature of plasma has a significant influence. Duration and power are equally or even more useful to improve adhesion. They decrease drastically the contact angle; analysis for Ar plasma (shown in Fig. 87) proves that a long exposure time and a higher power are the key parameters to remove the hydrophobic characteristic of the surface. Throughout the process, the injected gas is continually renewed. The partial pressure of the selected gas in the chamber is always imposed at $p \cong 170$ mTorr.

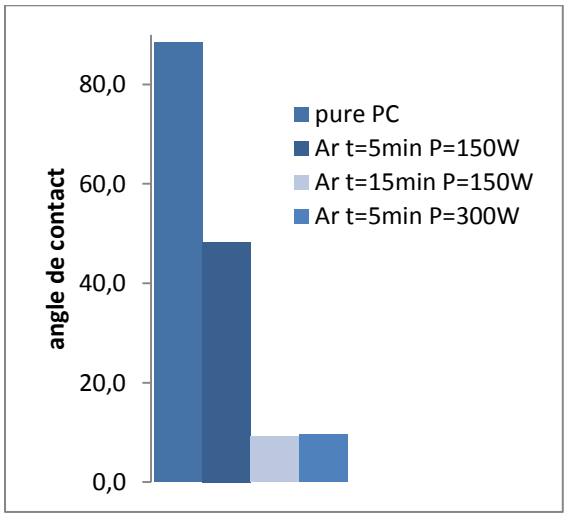


Fig. 87. Measurement of the influence of duration and power of argon plasma

The adhesion of the carbon nanotubes is now satisfactory to cover uniformly a large polymer surface. Experiments showed that plasma indeed modifies surface property. We will investigate the underlying science to understand the modifications. A physical analysis of the surface will be conducted by AFM in order to quantify the change of roughness. A chemical analysis will reveal the modification of polymer chains on the surface.

2. AFM topography

The surface of exposed PC was observed by AFM in order to define how the roughness is affected by the treatment. In fact, collision of ionised molecule at high energy with polymer is susceptible to modify the flatness in surface. A virgin surface has been captured in tapping mode; Fig. 88 shows the height of bounces is around 10nm if the impurities are removed. The second AFM capture at higher zoom confirms that the surface is relatively flat.

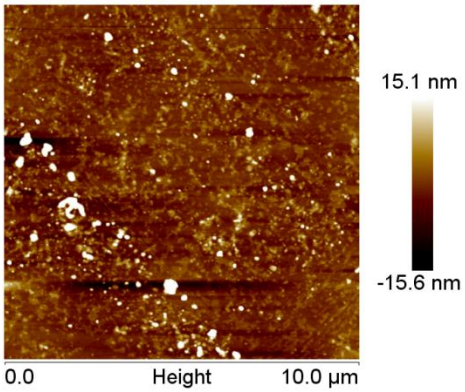


Fig. 88. AFM pictures in tapping mode of pure polycarbonate surface

The AFM analysis of a sample exposed to oxygen or argon plasma is completely different from that of a virgin surface. The roughness is clearly enhanced by an Ar activation as evidenced in Fig. 89. The spread view in Fig. 89a shows mounts and valleys almost 10 times higher than in the previous figure. This topographic analysis proves that a plasma exposure modifies roughness of polycarbonate. However, it is not possible to discriminate between finger prints of different plasmas using AFM images: nature of ionised gas does not induce any visible change on the surface. Further analysis has to be conducted to discriminate between chemical modifications of the surface.

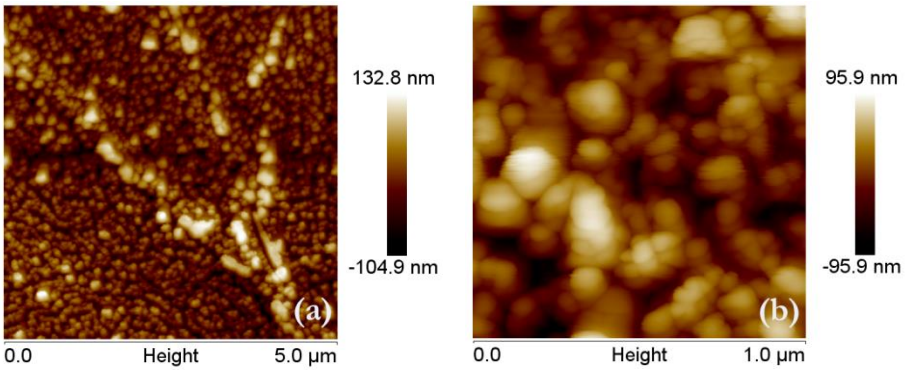


Fig. 89. AFM mapping in tapping mode of polycarbonate surface exposed to 150W argon plasma for 15 minutes

3. X-ray photoelectron spectroscopy (XPS)

XPS analysis was conducted to know the deterioration of polymer chains induced by plasma. Global XPS spectrum of pure and activated polycarbonate are represented in Fig. 90. These are measurements of pure PC, PC exposed to argon, oxygen and successively argon next oxygen plasma. Polycarbonate is composed of C-C, C-O, C-H and other covalent bonds. In global sweep, a F1s and Si2p peak appears because of rare impurities integrated during process.

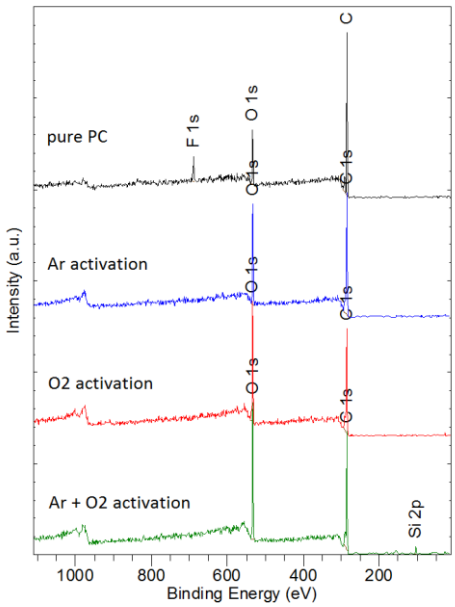


Fig. 90. XPS spectrum of pure PC, PC exposed to oxygen plasma, PC exposed to argon plasma and PC exposed to argon then oxygen plasma.

For polycarbonate, important bonds are O 1s and C 1s. The sweep is spread out for those energy ranges in order to distinguish the type of carbon or oxygen bond. Fig. 91a provides the energy for breaking oxygen bonds in polycarbonate molecule. The peaks corresponding to O-C bond and O=C bond are respectively located at 534.06 eV and 532.41 eV. The change of intensity of those peaks gives evidence that the amount of each bond is affected by plasma activation. Taken as a whole, intensity of activated sample is higher than reference polymer. Argon plasma even reverses ratio O-C/O=C. The qualitative analysis of C 1s bonds shows a clear change of weak peak above 288 eV. The main peak at 284.8 eV corresponds to C-(C or H) bonds (aromatic + aliphatic bonds). It decreases in intensity from reference to activated samples.

Plasma degrades partially the aromatic cycle and lightly modifies C-O (286.28 eV), C=O (287.29 eV), COO (289.22 eV), $C_{aromatic}$-O (286.35 eV) and CO-(C=O)-O (290.69 eV) bonds.

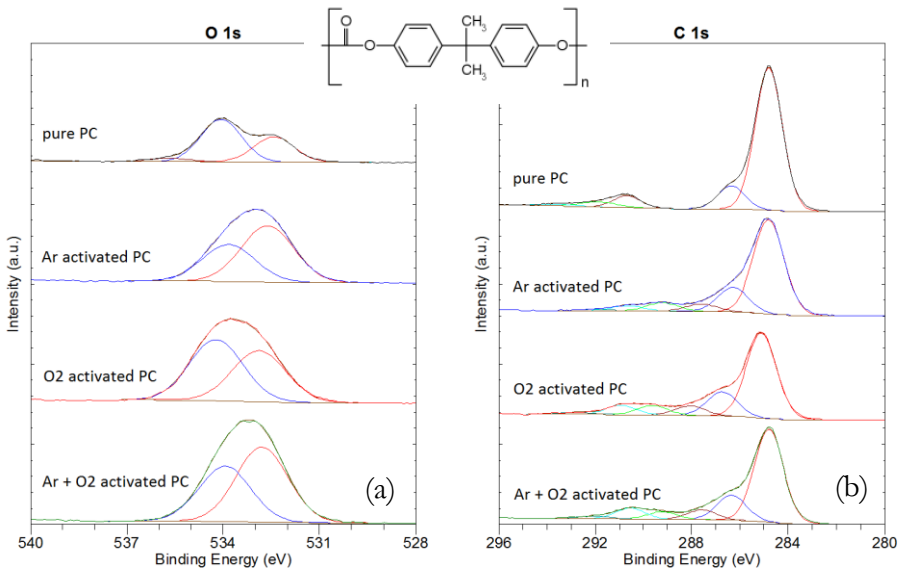


Fig. 91. spectra of C 1s bond in (a) and O 1s in (b). The inset shows polycarbonate molecule.

The AFM observation of the surface and the XPS analysis showed that it was not conceivable to determine the action of a precise plasma compared to another. It is therefore not appropriate to use these results to select one plasma. Nevertheless, we now know that exposure to plasma modifies the surface roughness and surface chemistry. After exposure, the polymer chains are broken and are pending which partly explains the better wettability. As observed experimentally, this chemical activation is attenuated over time. Indeed, the free bonds of the polymer will react quickly with the ambient air. It is therefore essential to maintain the sample under vacuum and apply the CNT ink as soon as possible. In practice, AquaCyl™ was applied directly after exiting the plasma chamber.

Annex B

Gel permeation chromatography (GPC) of PC-NW composites

The implementation of the nanowires-polycarbonate composite can degrade the polymer. A Gel Permeation Chromatography (GPC) is made to identify the level of degradation. Alliance Waters 2695 GPC separates dissolved molecules according to their size by pumping in special columns containing microporous material. As the sample is separated from the column, the Waters 2487 dual λ Absorbance detector measures the distribution of the absolute molecular weight, molecular size and the intrinsic viscosity. From that, we extract information on the macromolecular structure, aggregation and branching.

Pure polycarbonate is exposed to ultra-sonication or to 300°C for 45 minutes. A sample is taken every 15 minutes to highlight a possible evolution of degradation. Fig. 92 shows the GPC results for each step during process compared with the reference virgin polycarbonate. The molecular weight is plotted versus the molecular weight distribution function $\frac{\partial \mathrm{wt}}{\partial(\log \mathrm{M})}$. A movement to the right means that the molecular weight decreases and therefore the polymer chains are degraded. PC exposed to high temperature is very close to the reference curve, the sonicated PC followed very closely too. The level of damage caused by the temperature and even ultrasound is present but negligible.

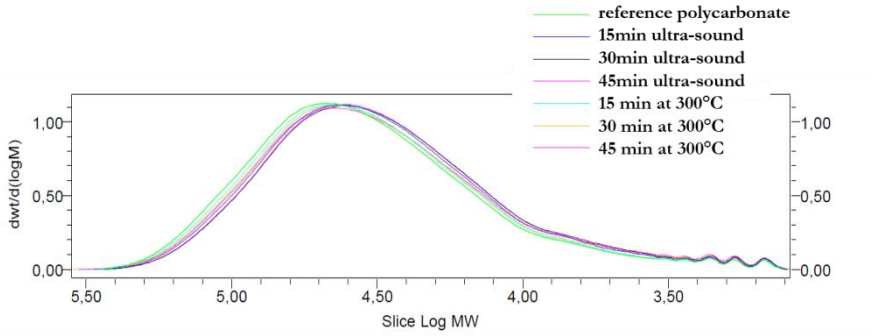


Fig. 92. GPC curves of virgin PC, PC exposed to sonication or high temperature (300°C). A sample is analysed all spans of 15min.

Residues of NaOH (and acetic acid) are also blamed of potential deterioration of the polymer. A second GPC is led on the composite PC-NW itself. Several samples are taken at different positions of the composite (in case of local agglomerates). The shift with the reference curve is more pronounced (see Fig. 93). The combination of sonication, high temperature and chemical residues decline a bit the polycarbonate

quality. Mechanical properties are thereby slightly diminished. However, there is not a real handicap for electromagnetic applications.

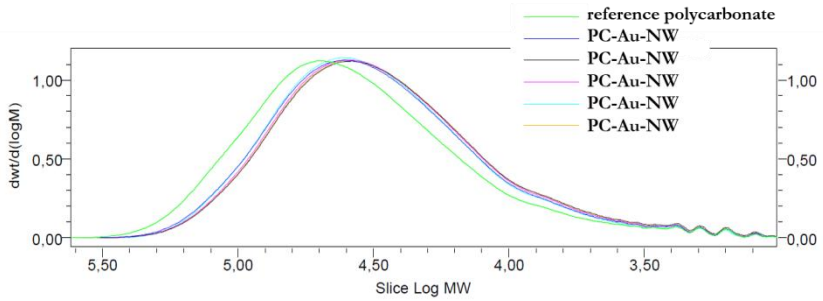


Fig. 93. GPC on PC – Au-NW composite. The reference curve is pure polymer.

Annex C

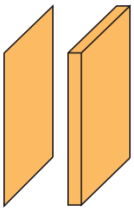
Summary of the multilayers

The main materials and structures used as building blocks for the multilayers are illustrated above and with their intrinsic EM properties are given. Each multilayer corresponds to a specific illustration; they are all shown in the next paragraph. Some structural information, an estimate of the global nanofiller density per surface unit, the total thickness and the figure of merit are provided for the set of multilayers.

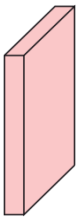
1. Building blocks



Pure polycarbonate
$\varepsilon_r = 2.8$ (in GHz)
$\sigma = 10^{-12}$S/m
$\mu_r = 1$
t variable



Arlon AD1000
$\varepsilon_r = 10.7$ (in GHz)
$\sigma = 10^{-12}$S/m
$\mu_r = 1$
t = 1.5mm or 9.6mm



Granite
$\varepsilon_r = 9$ (in GHz)
$\sigma = 10^{-10}$S/m
$\mu_r = 1$
t = 10.45mm



PC-CNT composite blended by extrusion
$\varepsilon_r \cong 3$ (in GHz)
σ variable
$\mu_r = 1$
t = 175µm



Thin CNT deposition
$\varepsilon_r \cong 3$ (in GHz)
σ variable
$\mu_r = 1$
$t \cong 7\mu m$



AquaCyl™ CNT sandwich
(produced by dip coating or airbrushing)
$\varepsilon_r \cong 3$ (in GHz)
σ variable
$\mu_r = 1$
t variable



Thin Ni-NW deposition
$\varepsilon_r \cong 3$ (in GHz)
σ variable
$\mu_r$variable
$t \sim \mu m$



Parallel CNT striplines film
$\varepsilon_r \cong 3$ (in GHz)
σ variable
$\mu_r = 1$
$t = 125\mu m$

2. Characteristic of the multilayers

Multilayer 1

13 conductive layers:
PC-CNT blended by extrusion (175μm)

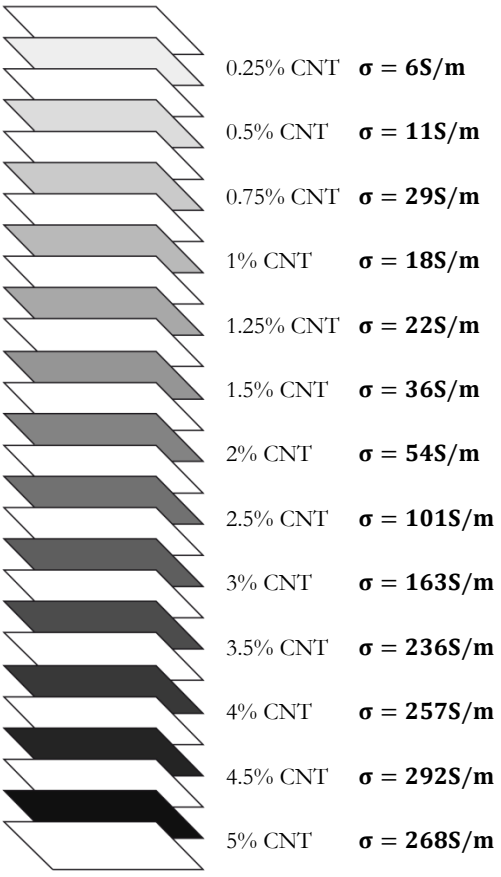
14 dielectric layers:
pure PC (110μm)

CNT density: $\sim 11 mg/cm^2$

Total thickness: 4.90mm

Rozanov result:
$0.0275 \leq 0.0967$

Figure of merit:
$$Q = \frac{0.0254}{t} = 5.2$$



Multilayer 2

9 conductive layers:
diluted AquaCyl™ is dip coated on PC (~7µm)

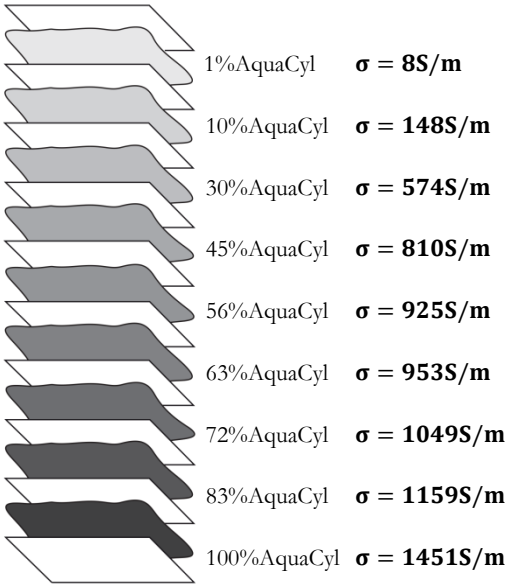
10 dielectric layers:
pure PC (250µm)

CNT density: $\sim 10 mg/cm^2$

Total thickness: 2.56mm

Rozanov result:
$0.0245 \leq 0.0505$

Figure of merit:
$Q = \frac{0.0236}{t} = 9.2$

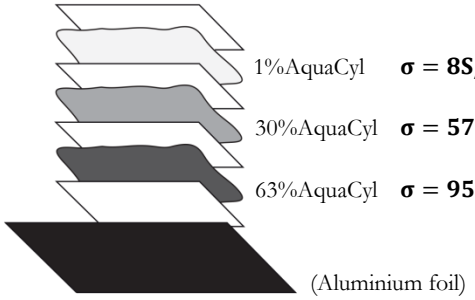


Multilayer 3

3 conductive layers:
diluted AquaCyl™ is dip coated on PC (~7µm)

4 dielectric layers:
pure PC (900µm)

+back-sided reflector



CNT density: $\sim 3.5 mg/cm^2$

Total thickness: 3.65mm

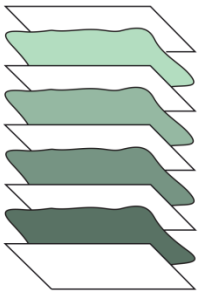
Rozanov result: $0.0675 \leq 0.0720$

Figure of merit (theoretical): $Q = \frac{0.0223}{t} = 6.1$

Multilayer 4

4 conductive layers: surface of entangled Ni-NW
5 dielectric layers: pure PC

The physical properties are effective values of PC|Ni-NW|PC sandwiches 150μm thick (corresponding to direct measurement).



2.8mg Ni-NW	$\boldsymbol{\sigma = 0.5S/m}$	$\boldsymbol{\mu_r' = 1.2}$	$\boldsymbol{\mu_r'' = 1.3}$
4.5mg Ni-NW	$\boldsymbol{\sigma = 1.5S/m}$	$\boldsymbol{\mu_r' = 2.1}$	$\boldsymbol{\mu_r'' = 1.3}$
8.7mg Ni-NW	$\boldsymbol{\sigma = 3S/m}$	$\boldsymbol{\mu_r' = 2.4}$	$\boldsymbol{\mu_r'' = 1.3}$
31 mg Ni-NW	$\boldsymbol{\sigma = 45S/m}$	$\boldsymbol{\mu_r' \cong 13}$	$\boldsymbol{\mu_r'' \cong 12}$

Ni-NW density: 4.95mg/cm^2

Total thickness: 600μm

Rozanov result: $0.0339 \leq 0.0564$

Figure of merit: $Q = \frac{0.0323}{t} = 53.8$

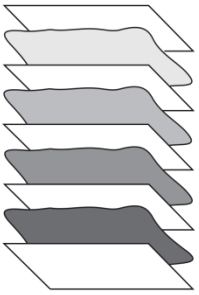
Multilayer 5

4 conductive layers: diluted AquaCyl™ is dip coated on PC
5 dielectric layers: pure PC

The physical properties are effective values of PC|CNT|PC sandwiches 175μm thick.

CNT density: $\sim 5\text{mg/cm}^2$

Total thickness: 700μm



1%AquaCyl	$\boldsymbol{\sigma = 0.3S/m}$
10%AquaCyl	$\boldsymbol{\sigma = 1.5S/m}$
10%AquaCyl	$\boldsymbol{\sigma = 3S/m}$
72%AquaCyl	$\boldsymbol{\sigma = 45S/m}$

Rozanov result: $0.0041 \leq 0.0138$

Figure of merit: $Q = \frac{0.0271}{t} = 38.8$

Multilayer 6

6 conductive layers: CNT striplines airbrushed on PC (pattern *narrow*, see section IV-2.3). Each sandwich is 125µm thick.
4 dielectric layers: pure PC (100µm)

Effective conductivity of patterned films is given parallel ∥ and perpendicular ⊥ to electric field.

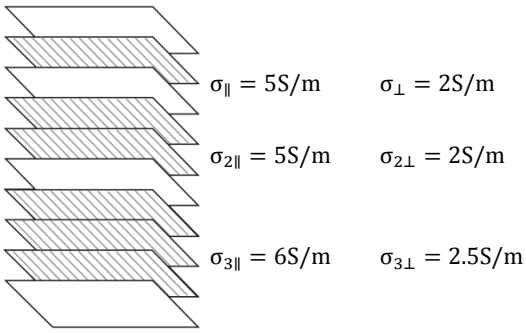
CNT density: $\sim 2.5 mg/cm^2$

Total thickness:1150µm

Figures of merit:

$$Q_{\parallel} = \frac{0.0210}{t} = 18.2$$

$$Q_{\perp} = \frac{0.0127}{t} = 11$$



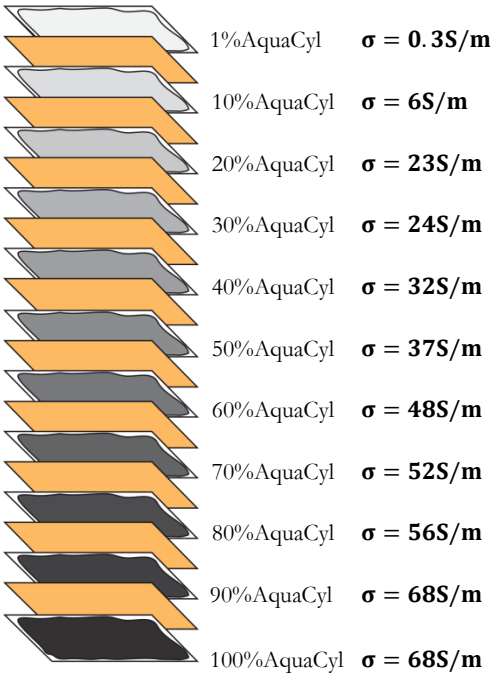
Multilayer 7

11 conductive layers:
PC|CNT|PC sandwiches
250µm thick

10 dielectric layers:
Arlon AD1000 (1.5mm)

CNT density: $\sim 13 mg/cm^2$

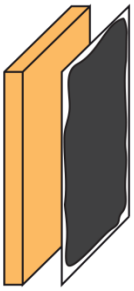
Total thickness: 17.97mm



Multilayer 8

1 dielectric layer:
Arlon AD1000

$\varepsilon_r = 10.7$
$\sigma = 10^{-12}$s/m
$\mu_r = 1$
t = 9.6 mm



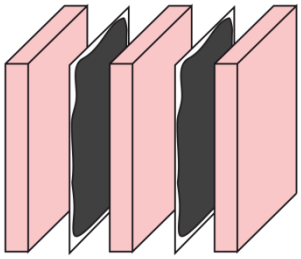
1 conductive layer:
PC|CNT|PC sandwich
(by 3x airbrushing)
$\varepsilon_r \cong 3$
$\sigma = 100$ S/m
$\mu_r = 1$
t = 100µm

CNT density: ~1.5mg/cm²
total thickness: 9.7mm

Multilayer 9

3 dielectric layers:
Granite slabs

$\varepsilon_r = 9$
$\sigma = 10^{-10}$s/m
$\mu_r = 1$
t = 10.45 mm



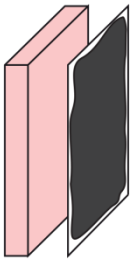
2 conductive layers:
PC|CNT|PC sandwiches
(by 3x airbrushing)
$\varepsilon_r \cong 3$
$\sigma = 100$ S/m
$\mu_r = 1$
t = 100µm

CNT density: ~3mg/cm²
total thickness: 31.55mm

Multilayer 10

1 dielectric layer:
Granite slab

$\varepsilon_r = 9$
$\sigma = 10^{-10}$s/m
$\mu_r = 1$
t = 10.45 mm



1 conductive layer:
PC|CNT|PC sandwich
(by 3x airbrushing)
$\varepsilon_r \cong 3$
$\sigma = 100$ S/m
$\mu_r = 1$
t = 100µm

CNT density: ~1.5mg/cm²
total thickness: 10.55mm